Explaining trends and changing seasonal cycles of surface ozone in North America and Europe over the 2000-2018 period: A global modelling study with NO_X and VOC tagging

Tabish Ansari[1*], Aditya Nalam[1,2], Aurelia Lupaşcu[3], Carsten Hinz[4], Simon Grasse[4], and Tim Butler[1,2]

[1]Research Institute for Sustainability at the GFZ ~~Helmholtz Centre Potsdam~~ (RIFS), Potsdam, 14467, Germany
[2]Institut für Meteorologie, Freie Universität Berlin, Berlin, Germany
[3]European Center for Medium Range Weather Forecasts (ECMWF), Bonn, 53175, Germany
[4]Jülich Supercomputing Centre (JSC), Forschungszentrum Jülich GmbH, 52428 Jülich, Germany

Correspondence to: Tabish Ansari (tabish.ansari@rifs-potsdam.de)

Abstract. Surface ozone, with its long enough lifetime, can travel far from its precursor emissions, affecting human health, vegetation, and ecosystems on an intercontinental scale. Recent decades have seen significant shifts in ozone precursor emissions: reductions in North America and Europe, increases in Asia, and a steady global rise in methane. Observations from North America and Europe show declining ozone trends, a flattened seasonal cycle, a shift in peak ozone from summer to spring, and increasing wintertime levels. To explain these changes, we use TOAST 1.0, a novel ozone tagging technique implemented in the global atmospheric model CAM4-Chem which attributes ozone to its precursor emissions fully by NO_X or VOC+CO+CH4 sources and perform multi-decadal model simulations for 2000-2018. Model-simulated maximum daily 8h ozone (MDA8 O_3) agrees well with rural observations from the TOAR-II database. Our analysis reveals that declining local NO_X contributions to peak-season ozone (PSO) in North America and Europe are offset by rising contributions from natural NO_X (due to increased O3 production ~~productivity~~), and foreign anthropogenic- and international shipping NO_X due to increased emissions. Transported ozone dominates during spring. Methane is the largest VOC contributor to PSO, while natural NMVOCs become more important in summer. Contributions from anthropogenic NMVOCs remain smaller than those from anthropogenic NO_X. Despite rising global methane levels, its contribution to PSO in North America and Europe has declined due to reductions in local NO_X emissions. Our results highlight the evolving drivers of surface ozone and emphasize the need for coordinated global strategies that consider both regional emission trends and long-range pollutant transport.

1 Introduction

Ozone near the Earth's surface is primarily formed by the photodissociation of NO_2 molecules by sunlight - the NO_2 molecule breaks down and furnishes atomic oxygen which combines with molecular oxygen in the air to form ozone. The naturally occurring NO_2 concentration in the troposphere is low and cannot alone explain the high ozone observed in the troposphere (Jacobson, 2005; Seinfeld & Pandis, 2016). However, in the modern era ~~especially towards the end of the 20th century~~ especially during the last half of the 20th century, increased industrialization and motorization of society has led to increasing emissions of nitric oxide (NO) (Logan 1983; Beaton et al., 1991; Calvert et al., 1993). NO can interact with peroxy radicals, chiefly produced from naturally and anthropogenically emitted non-methane volatile organic compounds (NMVOCs), carbon monoxide (CO), and methane (CH_4) in the presence of the hydroxyl radical (OH) to form NO_2 which can then produce ozone through the pathway described above (Atkinson 1990, 1994, 1997; Seinfeld & Pandis, 2016). Unsurprisingly, with increasing anthropogenic activities emitting NO, CO, NMVOCs and CH_4, the ozone concentrations in the troposphere and at the surface have risen substantially as compared to the pre-industrial or early-industrial times (Logan 1985; Crutzen 1988; Young et al., 2013; UNEP and CCAC, 2021).

Ozone is a highly reactive pollutant that harms human health, vegetation, and the environment due to its oxidative properties. In humans, it causes respiratory inflammation, exacerbates chronic illnesses, and impairs lung function by generating reactive oxygen species that damage cellular structures (Lippmann 1989; Chen et al., 2007; Devlin et al., 1991; Brook et al., 2004) due to long term exposure as well as short term exposure at high concentrations (Fleming et al., 2018). Ozone disrupts photosynthesis in plants and damages tissues, reducing crop yields and altering ecosystems (Ashmore 2005; Felzer et al., 2007; Grulke & Heath 2019; Cheesman et al., 2024); a recent assessment by Mills et al. (2018) shows persistent high levels of ozone adversely affecting various types of crops and vegetation in northern hemispheric regions. Moreover, it contributes to climate change by diminishing the carbon sequestration ability of vegetation and acting as a greenhouse gas (Oeschger & Dutsch 1989; Sitch et al, 2007; Szopa et al., 2021). In light of these harmful effects, the World Health Organization (WHO) has set safe standards for short-term and long-term human exposure to ozone: on any day, the maximum 8h average ozone concentration (MDA8 O_3) which must not exceed 100 μgm^{-3} (or ~51 ppb), and annually, the Peak Season Ozone (PSO), i.e., the maximum value of the six-month running average of MDA8 O_3, must not exceed 60 μgm^{-3} (or ~30.61 ppb) (WHO 2021).

In order to meet these safe health standards, various national governments - particularly in North America and Europe and more recently in China - have acted to reduce their industrial and vehicular emissions by adopting cleaner fuel and technologies and have successfully managed to bring down their national NO_X and NMVOC emissions substantially (Goldberg et al., 2021; Shaw & Heyst 2022; Crippa et al., 2023). However, these national efforts of emission reductions have not fully translated into commensurate reductions in local ozone concentrations and health impacts (Seltzer et al., 2020; Parrish et al., 2022). This is due to the long-enough atmospheric lifetime of ozone ~~(about 3-4 weeks)~~ which allows it to

traverse intercontinental distances and affect the air quality of regions far from the location of its chemical production or the location of the emission of its precursors. While the global average tropospheric lifetime of ozone is often cited as approximately 3-4 weeks, a figure largely influenced by more rapid photochemical loss in warmer, humid tropical regions (e.g., Stevenson et al., 2006; Young et al., 2013), the effective lifetime of ozone in air parcels transported within the cooler, drier free troposphere at northern midlatitudes is considerably longer, on the order of several months (e.g., Jacob, 1999; Wang and Jacob, 1998; Fiore et al., 2009). This extended lifetime in the primary transport pathway for intercontinental pollution allows ozone to traverse vast distances and enables the northern mid-latitude free troposphere to act as a relatively well-mixed reservoir (Parrish et al., 2020). Moreover, some ozone precursors (e.g., CO and less reactive NMVOCs) also possess atmospheric lifetimes sufficient for intercontinental transport, subsequently contributing to ozone formation in downwind regions far from their original emission sources. Therefore, air quality benefits in regions with declining emissions can be offset by an increasing share of transported ozone from far away regions where emissions are on the rise. Many previous observational-based studies have reported declining peak-ozone trends in North America towards the final decades of the 20th century and the beginning of the 21st century (Wolffe et al., 2001; Cooper et al., 2014; Cooper et al., 2015; Chang et al., 2017; Fleming et al., 2018; Cooper et al., 2020). However, some of these studies and many others - through novel statistical decomposition~~filtering~~ of observational data - have also pointed out increasing trends in wintertime and background ozone concentrations at many sites in North America, particularly at the US west coast (Jaffe et al., 2003; Cooper et al., 2010; Simon et al., 2014; Parris & Ennis, 2019; Parrish et al., 2022; Christiansen et al., 2022). Such increases in ozone have also been identified throughout the background troposphere at northern midlatitudes including in the free troposphere, with a peak attained in the first decade of the 2000s (e.g., Parrish et al., 2020; Derwent et al., 2024). Some of these observational studies (e.g., Jaffe et al., 2003) have further correlated the increasing background ozone in western US to increasing emissions in Asia while others (e.g., Cooper et al., 2010) have also employed air mass back trajectory analysis to support their claims. Jaffe et al., (2018) performed a comprehensive knowledge assessment of background ozone in the US and emphasized its growing relative importance and advocated for, among other things, a more strategic observational network and new process-based modelling studies to better quantify background ozone in the US to support informed clean air policies. A number of observational studies have also reported changes in the ozone seasonal cycle in North America, with shifting peaks from summer to springtime (Bloomer et al., 2010; Parrish et al., 2013; Cooper et al., 2014), a reversal of the spring-to-summer shift in peak ozone during mid-twentieth century which was reported in earlier studies (e.g., Logan 1985) when anthropogenic emissions were increasing in North America. Similarly, for Europe, many studies have observed declining ozone trends since 2000 (Cooper et al., 2014; Chang et al., 2017; Fleming et al., 2018; EEA report 2020; Sicard 2021). For Europe too, there have been attempts of statistical decomposition~~filtering~~ and analyses of observational data in innovative ways to highlight the increasing share of intercontinental transport and the consequent changes in ozone seasonal cycle in recent decades (Carslaw 2005; Parrish et al., 2013; Derwent & Parrish, 2022).

Reliable, long-term, and publicly accessible monitoring stations across different continents form the backbone of an international consensus on ozone distributions, trends, and health impacts on various populations. These observational networks provide essential data for advanced statistical analyses, which can estimate both transported and locally produced ozone (as seen in many observational studies mentioned earlier). However, such statistical interpretations can be subject to dispute and must be corroborated by well-evaluated atmospheric chemical transport models which simulate atmospheric transport processes explicitly. Together, observational analyses and model-generated results can aid the theoretical development and improvement of simpler conceptual models that capture the essence of the most salient physical and chemical processes that control observed ozone abundances (Derwent et al., 2024).

The hemispheric-scale transport of "foreign" ozone is a phenomenon peculiar to longer-lived pollutants such as ozone. While short-lived pollutants like PM2.5, which are regional in nature, can be largely controlled through domestic policies, effective ozone mitigation requires international engagement and cooperation. Developing such cooperation requires a high-trust international dialogue, underpinned by confident estimates of ozone transport between regions on which there is international consensus. These estimates are vital to implementing effective policies in a world where "foreign" ozone contributions are significant.

Atmospheric chemical transport models simulate the emission, chemical production and loss, transport, and removal of various coupled species within the atmosphere and allow us to assess theory against observational evidence. Atmospheric models can also enable us to quantify various source contributions to concentrations of a particular chemical species in a given location or region. This is achieved by using, broadly, one of the two methods - *perturbation* or *tagging*. In the *perturbation* method, several runs are conducted where certain emission sources are removed or reduced and the resulting concentration fields are subtracted from the baseline run with full emissions to yield the contribution of the removed source. In the *tagging* method, generally a single simulation yields source contributions from different tagged regions or emission sectors. The contributions derived from the perturbation method are not the true contributions operating under baseline conditions. Instead, they represent the response of all other sources to the removal of a particular source, which may be different from their contribution when all sources are present (Jonson et al., 2006; Burr & Zhang, 2011; Wild et al., 2012; Ansari et al., 2021). Therefore, perturbation experiments are best-suited to evaluate air quality policy interventions, when certain emission sources are actually removed (or reduced) or are planned to be removed in the real-world as part of policy. On the other hand, *tagging* techniques, which track the fate of emissions from designated sources as they undergo transport and chemical transformation within the unperturbed baseline atmosphere, allow us to assess the contribution of various sources under a baseline scenario when no policy intervention has been made. We refer the reader to Grewe et al. (2010) for a first-principles discussion on perturbation versus tagging methods and to Butler et al. (2018) for a review of different tagging techniques.

With growing observational evidence of the increasing importance of "foreign" transported ozone, there have been many attempts at confirming and quantifying these contributions using both perturbation-based and tagging-based model simulations for both North American and European receptor regions in recent years. For example, Reidmiller et al. (2009) used results from an ensemble of 16 models which conducted several regional perturbations for the year 2001, to report that East Asian emissions are the largest foreign contributor to springtime ozone in western US while European emissions are the largest foreign contributor in eastern US. Lin et al., (2015) disentangled the role of meteorology from changing global emissions in driving the ozone trends in the US by performing sensitivity simulations with fixed emissions over their simulation period of 1995-2008. Strode et al. (2015) conducted a perturbation experiment where they only allowed domestic US emissions to vary over time but keep the remaining global emissions fixed at an initial year to better quantify the effect of changing foreign emissions on ozone in the US. Similarly, Lin et al. (2017) performed global model simulations with several perturbation experiments where emissions were fixed at the initial year over Asia and where US emissions were zeroed-out. They used the difference between the simulated concentrations in their perturbation and base simulations to quantify the influence of local and foreign emission changes on the ozone concentrations in the US. Mathur et al. (2022) calculated emission source sensitivities of different source regions for the year 2006 using a sensitivity-enabled hemispheric model and applied these sensitivities to multi-decadal simulations to compute the influence of foreign emissions on North American ozone levels. They found a declining influence of European emissions and an increasing influence of East- and Southeast Asian emissions along with shipping emissions on the spring- and summertime ozone in North America. Derwent et al. (2015) used an emissions-tagging method in a global Lagrangian model for the base year 1998 to explain the changing ozone seasonal cycle in Europe. Garatachea et al. (2024) performed three-year long regional model simulations with emissions tagging to calculate the import and export of ozone between European countries. Building on previous work, Grewe et al. (2017) introduced a new tagging method which assigns different ozone precursors into a limited number of chemical 'families' and attributes ozone to multiple sources within each family. Mertens et al. (2020) used this tagging technique at a regional scale to calculate the contribution of regional transport emissions on surface ozone within Europe.

As pointed out earlier, perturbation-based estimates are more suited to evaluate an emissions policy intervention rather than to quantify baseline contributions of various sources (Grewe et al., 2010, 2017; Mertens et al., 2020). Tagging techniques, in calculating baseline source contributions, can also have limitations. For example, they often tag combined NO_X and VOC emissions over a tagged region or attribute ozone to the geographic location of its chemical production rather than the original location of its precursor emissions (as in Derwent et al., 2015) which can complicate policy-relevant interpretation of the model results. Some tagging techniques (as in Garatachea et al., 2024) tag ozone only to its limiting precursor in each grid cell thereby complicating detailed chemical interpretation of the computed contributions. While others (e.g., Grewe et al., 2017; Mertens et al., 2020) attribute ozone molecules to tagged NO_X and VOC depending on their abundances relative to the total amount of NO_X and VOC present in each grid cell at each time step.

In this study, we use the TOAST tagging technique as described in Butler et al. (2018) which separately tags NO_X and NMVOC emissions in two model simulations to provide separate NO_X and VOC contributions from different regions and sectors to simulated ozone in each model grid cell. The results from NO_X- and VOC-tagging can be compared side-by-side and the total contributions of all sources from both simulations add up to the same total baseline ozone. The TOAST tagging technique has been previously applied in both global (Butler et al., 2020; Li et al., 2023; Nalam et al., 2025) and regional models (Lupascu & Butler, 2019; Lupascu et al., 2022; Romero-Alvarez 2022; Hu et al., 2024) to calculate tagged ozone contributions over US, Europe, East Asia as well as the global troposphere.

We describe our model configuration, simulation design, input emissions data, and observations from the TOAR-II database used for model evaluation in section 2. In section 3.1, we present region-specific model valuation for the policy-relevant MDA8 O_3 metric. Key results on attribution of trends and seasonal cycle to NO_X and VOC sources are presented in sections 3.2 for North America and section 3.3 for Europe. We finally summarise our key findings along with potential future directions in section 4.

2 Methodology

2.1 Model description, tagged emissions, and simulation design:

We perform two 20-year long (1999-2018) global model simulations, with 1999 used as a spin-up year, using a modified version of the Community Atmosphere Model version 4 with chemistry (CAM4-Chem) which forms the atmospheric component of the larger Community Earth System Model version 1.2.2 (CESMv1.2.2; Lamarque et al., 2012; Tilmes et al., 2015). The gas-phase chemical mechanism employed in this study is based on the Model for Ozone and Related chemical Tracers, version 4 (MOZART-4) (Emmons et al., 2010) which includes detailed O_x-NO_x-HO_x-CO-CH_4 chemistry, along with the oxidation schemes for a range of non-methane volatile organic compounds (NMVOCs). Specifically, MOZART-4 treats 85 gas-phase species involved in 39 photolytic and 157 gas-phase reactions. NMVOCs are represented using a lumped species approach, where, for example, alkanes larger than ethane are lumped as a single species (e.g., BIGALK for C4+ alkanes), and alkenes larger than ethene are lumped (e.g., BIGENE), with specific treatments for aromatics, isoprene, and terpenes. The oxidation products of these lumped and explicit VOCs are also tracked. Further details on the MOZART-4 chemical mechanism, including the full list of species and reactions, can be found in Emmons et al. (2010). The two simulations are identical in simulating the baseline chemical species including the total ozone mixing ratios, however, they are used to separately tag region- or sector-based NO_X and VOC ozone precursor emissions respectively which ultimately allow us to break down ozone mixing ratios into their tagged NO_X or VOC sources separately.

The model is run at a horizontal resolution of 1.9º×2.5º, a relatively coarse resolution which essentially allows us to compensate for the added computational burden due to the introduction of many new chemical species in form of tags and to effectively carry out two multi-decadal simulations. Vertically, the model was configured with 56 vertical levels with the top layer at approximately 1.86 hPa and roughly the bottom half of the levels representing the troposphere. The model is run as an offline chemical transport model with a chemical time-step of 30 min and is meteorologically driven by prescribed fields from the MERRA2 reanalysis (Molod et al., 2015) with no chemistry-meteorology feedback. The model is meteorologically nudged towards the MERRA2 reanalysis fields (temperature, horizontal winds, and surface fluxes) by 10% every time step.

We use the recently released Hemispheric Transport of Air Pollution version 3 (HTAPv3) global emissions inventory (Crippa et al., 2023) to supply the temporally varying anthropogenic emissions input for NO_X, CO, SO_2, NH3, OC, BC and NMVOCs over 2000-2018 for our model runs. These include multiple sectors including several land-based sectors but also domestic and international shipping as well as aircraft emissions. We break down the global aircraft emissions spatially to denote three different flight phases based on EDGAR6.1: landing & take-off, ascent & descent, and cruising. Based on this spatial disaggregation of flight phases, we vertically redistribute the aircraft emissions at appropriate model levels for each flight phase following the recommended vertical distribution in Vukovich & Eyth (2019). We also speciated the lumped NMVOCs as provided by the HTAPv3 emissions dataset, first, into 25-categories of NMVOCs as defined by Huang et al. (2017). This was done by using the regional (North America, Europe, Asia, and Other regions) speciation ratios specified for each sector by Crippa et al. (2023) (see table here: https://jeodpp.jrc.ec.europa.eu/ftp/jrc-opendata/EDGAR/datasets/htap_v3/NMVOC_speciation_HTAP_v3.xls). After obtaining the 25-category region- and sector-based NMVOC speciation, we further speciated them into the appropriate NMVOC species as required by the MOZART chemical mechanism, which included merging as well as bifurcation of certain species. Biomass burning emissions are taken from GFED-v4 inventory (van der Werf et al., 2010) which provide monthly emissions for boreal forest fires, tropical deforestation and degradation, peat emissions, savanna, grassland and shrubland fires, temperate forest fires, and agricultural waste burning. The biogenic NMVOC emissions are taken from CAMS-GLOB-BIO-v3.0 dataset (Sindelarova et al., 2021), while biogenic (soil) NO_X is prescribed as in Tilmes et al. (2015). While we spatially interpolate the emissions from HTAPv3 high-resolution (0.1º×0.1º) dataset to our coarser model resolution (1.9º×2.5º), it leads to some land-based emissions at coastal areas to spill into the ocean grid cells and vice versa, thereby creating a potential for misattribution of tagged emissions. To correct this, we move these wrongly allocated land-based emissions over ocean grid cells back to the nearest land grid cells (and similarly, wrongly moved oceanic emissions to coasts back into the ocean) to make sure that the emissions are allocated to the correct region for the source attribution. We also ensure that small islands which are smaller than the model grid cell area are preserved and their emissions are not wrongly attributed as oceanic or shipping emissions.

Our simulations do not resolve the full carbon cycle and do not have explicit methane emissions. Instead, methane concentration is imposed as a surface boundary condition. These methane concentrations are taken from the 2010–2018 average mole fraction fields from the CAMS CH_4 flux inversion product v18r1 (https://ads.atmosphere.copernicus.eu/cdsapp#!/dataset/cams-global-greenhouse-gas-inversion?tab=overview) and is specified as a zonally and monthly varying transient lower boundary condition. For upper boundary conditions, annually varying stratospheric concentrations of NO_X, O_3, HNO_3, N_2O, CO and CH_4 are prescribed from WACCM6 ensemble member of CMIP6 and are relaxed towards climatological values (Emmons et al., 2020).

Following the methodology of Butler et al. (2018 and 2020), as per the TOAST tagging system, we modify the MOZART chemical mechanism (Emmons et al., 2012) to include extra tagged species for the NO_X tags and VOC tags, respectively, for the two simulations. This system allows us to attribute almost 100% of tropospheric ozone in terms of its NO_X (+ stratosphere) sources and in terms of its VOC (+ methane + stratosphere) sources in two separate simulations. In the troposphere, almost all ozone production can be attributed to reactions between peroxy radicals and NO, producing NO2, which ultimately photolyzes to produce ozone. Only a small fraction (typically less than 1 ppb of ozone at the surface) can not be clearly attributed to either NOx or VOC precursors, for example the ozone production from O atoms formed through the self-reaction of hydroxyl radicals (Butler et al., 2018) which is labelled as "residual ozone" in our study . In the two simulations, aside from the full baseline emissions, we additionally provide regionally- and sectorally-disaggregated NO_X and VOC emissions, respectively, which undergo the same chemical and physical transformations in the model as the full baseline emissions. The regional tags are based on the HTAP2 Tier1 regions (Galmarini et al., 2017; see Figure 1, S12 and Table 1). Since the focus of this study is to study ozone trends and its sources in North America and Europe, and because ozone is primarily a hemispheric pollutant (with little inter-hemispheric contributions), we explicitly tagged the land-based NO_X emissions in the northern hemisphere regions, namely, North America, Europe, East Asia, South Asia, Russia-Belarus-Ukraine, Mexico & Central America, Central Asia, Middle East, Northern Africa and Southeast Asia, while the southern hemisphere regions of South America, Southern Africa, Australia, New Zealand and Antarctica are tagged together as "rest-of-the-world". The ocean is also divided into multiple~~any~~ zones, mainly in the northern hemisphere, and tagged separately (see Figure S12). In case of the VOC emissions, we use fewer explicitly tagged regions and some of the explicitly tagged NO_X regions are aggregated with the "rest-of-the-world". This is done to ensure computational efficiency given that tagging NMVOC means tagging several speciated NMVOCs within the MOZART chemical mechanism (as opposed to a single NO species in case of NO_X tagging). In addition to the regional tags which carry anthropogenic emissions, we also tag other, mainly non-anthropogenic, global sectors separately: biogenic, biomass burning, lightning, aircraft, methane and stratosphere.

We specify an additional tag for NO_X emission generated from lightning parameterization (Price and Rind, 1992; Price et al., 1997) in our NO_X-tagged simulation, and for methane in our VOC-tagged simulation. We refer the reader to Figure 1 for the

geographic definitions of the various source regions and to Table 1 for more details on the regional and global tags for the NO_X and VOC-tagging runs. Based on these tags changes were made to the model source code following Butler et al. (2018) which allows for physical and chemical treatment of all tagged species within the model.

Figure 2 shows the trends in NO_X and VOC emissions for North America (NAM) and Europe (EUR) tagged source regions and for the northern hemisphere along with the global lightning NO_X emissions and prescribed methane concentrations over the study period. We see a consistent decline in North American anthropogenic NO_X emissions (Fig 2a) from ~250 Kg (N) s^{-1} in 2000 down to ~100 Kg (N) s^{-1}. We also see a decline in European anthropogenic NO_X emissions (Fig 2c), although starting from a lower base in 2000, from ~140 Kg (N) s^{-1} down to 80 Kg (N) s^{-1}. Similarly, the anthropogenic NMVOCs, or AVOCs, in the two regions (Figs 2b and d) have also declined substantially. These large emission changes reflect the strict and effective emission control policies implemented in these regions (Clean Air Act 1963, Clean Air Act Amendments 1990; Council Directive 1996, 2008). The biogenic NO_X emissions peak in summertime for both regions but remain much lower (up to 40 Kg (N) s^{-1} in North America and 20 Kg (N) s^{-1} in Europe) than the anthropogenic NO_X emissions and exhibit no long-term trend. NO_X emissions from fires remain extremely small. The biogenic NMVOCs, or natural VOCs, also peak during summertime for both regions. This is due to the larger leaf area in the summer season (Guenther et al., 2006; Lawrence and Chase, 2007). The natural VOCs for North America are higher than the AVOCs and show an increasing trend since 2013. The natural VOC emissions in Europe are comparable to the AVOC emissions especially in recent years. The biomass burning NMVOC emissions are the smallest but they show an increasing trend in North America. We have also plotted the total northern hemispheric (NH) NO_X and NMVOC emissions which can provide some context in understanding foreign contributions to ozone in North America and Europe. Here, we see the NH anthropogenic NO_X increasing from 2000 until 2013 after which it declines to below 2000 levels. This increasing trend is primarily driven by increasing Chinese emissions, while the decline is driven by a decline in Chinese, North American and European emissions (not shown). We see a similar trend for NH AVOC as well. Summertime NH natural VOC emissions exceed the AVOC emissions. NH biomass burning NMVOC emissions are also significant, up to 5000 Kg C s^{-1}, but they are lower than natural VOC and AVOC emissions and do not show any significant trend. Global lightning NO_X emissions show a declining trend from ~100 Kg (N) s^{-1} in 2000 to ~90 Kg (N) s^{-1} in 2014 after which they increase to 95 Kg (N) s^{-1} in 2018. The global methane concentration remains consistent, around 1780 ppb, for 2000-2006 but rises steadily since 2007 reaching around 1880 ppb in 2018. Understanding these trends in regional emissions of different ozone precursors allows us to better interpret tagged contributions to simulated ozone in later sections.

2.2 Model runs and initial post-processing:

We perform two separate 20-year long simulations for 1999-2018. The first year, 1999, is discarded as a spin-up year and only the outputs for 2000-2018 are used for further analyses. For the VOC-tagged run, the spin-up time was two years, such

that the 1999 run was restarted with the conditions at the end of the first 1999 run. Introducing extra tagged species with full physical and chemical treatment in the model leads to a substantial increase in computational time (approx. 6x-8x) as compared to a basic model run without tagging. Therefore, such a model configuration typically needs a large number of CPU cores spread over multiple parallel nodes. We run our tagged simulations on 6-nodes with 72 Intel Icelake cores each (432 cores in total) with a memory of 2048 GB per node. It takes approximately 24h and 36h wallclock time to complete a single year of simulation with NO_X- and VOC-tagging, respectively, with our model configuration. The VOC-tagged simulations take longer despite having fewer land-based and oceanic tags because, unlike NO_X-tagging, VOC-tagging involves all speciated NMVOCs to be tagged separately thereby increasing the total number of chemical species to be treated in the model.

We configure the model to write out key meteorological and chemical variables, including tagged O_3 variables, as 3D output at monthly average frequency but also write out the tagged O_3 variables at surface at an hourly frequency which allows us to assess key policy-relevant ozone metrics for further analyses. Before we proceed to analyses of the results, we convert the model output into global MDA8 O_3 (maximum daily 8h average) values along with its tagged contributions for each grid cell in the model. The model writes-out the hourly ozone values in Universal Time Coordinates (UTC) for all locations. Therefore, we first, consider different time-zones (24 hourly zones based on longitude range) and select the 24 ozone values by applying the appropriate time-offset to reflect a “local day” for each grid cell. Once a 24h local-day has been selected, we perform 8h running averages spanning these 24 values and pick the maximum of these 8h averages as the MDA8 O_3 value for that grid cell on a given day. We then use the selected time window for the MDA8 O_3 value for the grid cell to also calculate the 8h-average tagged contribution over this window. Using this methodology, we prepare global NetCDF files which contain daily MDA8 O_3 values along with tagged contributions for each grid cell. We use these files for further analyses.

Figure 3 shows the geographic definitions of various HTAP-Tier2 regions (Galmarini et al., 2017), out of which nine regions, five in North America, namely Eastern Canada, Northwest United States (NW US), Southwest United States (SW US), Northeast United States (NE US), and Southeast United States (SW US), and four in Europe,namely Western Europe, Southern Europe, C&E Europe, and SE Europe, shown in various shades of magenta and green, are used as receptor regions to perform further analyses of trends and seasonality in section 3. We use these receptor regions to perform area-weighted spatial averaging of MDA8 O_3 values before analysing the trends and contributions. Area-weighted spatial averaging is needed because different model grid cells cover different areas on the ground based on the rectangular lat-long coordinate system, with high-latitude grid cells covering smaller areas and low-latitude and equatorial grid cells covering larger areas. So, a simple spatial averaging will overrepresent the concentrations of high-latitude gridcells and underrepresent lower-latitude gridcell concentrations in the receptor region average. So, we derive dimensionless coefficients for all grid cells within each receptor region based on their relative size to the average grid cell area in that region. We scale the gridded

MDA8 O3 with these area-coefficients before spatial averaging, ensuring a proportionate representation of the MDA8 O3 value over the entire receptor region.

2.3 TOAR Observations and related data processing:

For model evaluation, we utilize ground-based observations of hourly ozone from many stations over North America and Europe which are part of the TOAR-II database of the Tropospheric Ozone Assessment Report (TOAR). We use the newly developed TOAR gridding tool (TOAR Gridding Tool 2024) to convert the point observations from individual stations into a global gridded dataset which matches our model resolution of 1.9º×2.5º. The TOAR gridding tool allows for data selection including the variable name, statistical aggregation, temporal extent and a filtering capability according to the station metadata.

We extract the Maximum Daily 8h Average (MDA8) metric for ozone from the TOAR-II database analysis service (TOAR-II 2021) for the years 2000 to 2018 (as available until May 2024). The MDA8 values are only saved if at least 18 of the 24 hourly values per day are valid (see, *dma8epa_strict* in TOAR-analysis 2023). This allows us to minimize any discrepancies between the observed and model-derived MDA8 O3 values. Also, since our model resolution is coarse, we only include rural background stations in our analyses to avoid influences of urban chemistry which may not be resolved in our model.

We use the *type_of_area* field of the station metadata to select the rural stations; this information is provided by the original data providers (see Acknowledgements for an exhaustive list of data providers). They cover about 20% of all stations in North America and Europe. We note that roughly a similar fraction of stations in these regions remains unclassified. In the final gridded product, which contains daily MDA8 O_3 values over North America and Europe a grid cell has non-missing value if there is at least one rural station present within it. We obtain large parts of NAM and EUR regions with valid TOAR grid cells, although the number of these valid grid cells changes day-to-day and year-to-year. In North America, the number of valid stations varies from 3-4 for Eastern Canada, 17-3~~4~~4 for NW US, 53~~2~~-139~~140~~ for SW US, 178-207~~134-235~~ for NE US, 116-139~~100-114~~ for SE US. In Europe, the number of rural stations varies from 140-154~~201-236~~ for Western Europe, 50-185~~57-223~~ for Southern Europe, 36-86~~45-100~~ for C&E Europe~~Central & Eastern Europe~~, and 1-19~~20~~ for SE Europe, with a general increase in the number of stations in each region with time~~, except for 2012 when there is an anomalous drop in the number of stations~~. Furthermore, the number of valid TOAR stations within each grid cell also varies for certain locations. To better understand the changes in the TOAR station network in each of the 9 receptor regions considered here, we have plotted a time-series of annual average number of stations within each receptor region. This is shown in Figure S11. We note that sparse spatiotemporal sampling can introduce uncertainty in identifying true long-term trends of ozone and refer the reader to a technical note on this issue by Chang et al. (2024) for more details.

3. Results:

3.1 Model Evaluation:

The CAM4-Chem model has been evaluated for its ability of simulating the distribution and trends of tropospheric ozone by many previous studies (Lamarque et al., 2012; Tilmes et al., 2015) including its modified version with ozone tagging (Butler et al., 2020; Nalam et al., 2024~~5~~). Generally, many atmospheric models including CAM4-Chem have been shown to overestimate surface ozone in the Northern Hemisphere (Reidmiller et al., 2009; Fiore et al. 2009; Lamarque et al., 2012; Young et al., 2013; Tilmes et al., 2015; Young et al., 2018; Huang et al, 2021). In a recent study that utilized the same model simulations as those presented in this study, Nalam et al. (2025~~4~~) evaluated model simulated monthly average surface ozone against gridded observations from the TOAR-I dataset (Schultz et al., 2017) over various HTAP Tier 2 regions (Galmarini et al., 2017) in North America, Europe and East Asia for 2000-2014 and found a satisfactory performance, albeit with a general high bias of 4-12 ppb, similar to a reference CMIP6 model CESM2-WACCM6 (Emmons et al., 2020); see Figure 1 in Nalam et al., 2025~~4~~ for more details. Furthermore, Nalam et al. (2025~~4~~) have also evaluated the model simulated monthly mean ozone against the ozone sonde-based climatology compiled by Tilmes et al. (2012) for different latitude bands in the northern hemisphere at different pressure levels over the same period and found generally high correlations and low biases - see Figure 2 in Nalam et al. (2024~~5~~) for further details.

One reason for a high bias as seen in Nalam et al., (2025~~4~~) and other studies could be the use of all available stations (including many urban stations) for evaluating the model performance. Given the coarse model resolution, we expect the model not to resolve high NO_X concentrations around the urban and industrial centres and therefore suffer from the lack of ozone titration. Therefore, here, we only evaluate the model against data from rural stations, wherever available. Also, in this study, we only work with policy-relevant metrics such as Maximum Daily 8h Average (MDA8) Ozone at the surface or other metrics derived from it, e.g., Peak Season Ozone (PSO). These metrics generally include only the daytime ozone, especially over land. Therefore, evaluating the model for these metrics also allows us to exclude nighttime ozone and avoid any large nighttime biases which often arise due to improper simulation of the nighttime boundary layer which has been a persistent issue in both global and regional models (Houweling et al., 2017; Du et al., 2020; Ansari et al., 2019).

For model evaluation, we derive regionally averaged monthly mean MDA8 O_3 for all HTAP tier 2 receptor regions for North America, Europe and Asia but sample the MDA8 O_3 values only from those gridcells where rural TOAR observations were available. Figure 4 shows the time-series of monthly mean MDA8 O_3 from the model and TOAR observations for the entire simulation period. We ask the reader to refer to the geographic extent of the receptor regions discussed here in Figure 3.

In Eastern Canada (Figure 4a), the model reproduces the O_3 seasonal cycle very well, especially between 2007-2018. It overshoots the maxima and undershoots the minima for the earlier years of 2000-2006. This could be due to inaccurate (higher) NO_X emissions over the region in the HTAPv3 inventory for the earlier years which leads to higher summertime production and lower wintertime levels due to increased titration. The model also reproduces the flattening annual cycle well which is consistent with decreasing NO_X emissions over this region (see Figures 3 and S6~~3~~). For the Northwestern United States (Figure 4b), the model reproduces the annual cycle ~~very~~ well, although it systematically overestimates the MDA8 O_3 during peak season by up to 5 ppb. For the Northeastern United States (Figure 4c), the model captures the structure of the annual cycle of MDA8 O_3 very well for recent years but overestimates the summer peak and underestimates wintertime ozone for earlier years, similar to Eastern Canada, again pointing to high NO_X emissions in the emission inventory over this region in the initial years. The model shows an extremely skilful simulation of MDA8 O_3 in the Southern United States. In SW US~~Southwestern US~~ (Figure 4d), the model reproduces the gradual and steady decline in MDA8 O_3 over time, albeit with a slight overprediction (~2ppb) in later years. Similarly, in the SE US~~Southeastern US~~ (Figure 4e), we note a very good reproduction of trends, with a decreasing summertime peak. For all North American regions, we see a high correlation between observed and modelled monthly mean MDA8 O3 values with correlation coefficient r ranging from 0.86 to 0.98. Correlations at the annual average timescale are lower and driven by interannual variability rather than seasonality of ozone. Mean bias is positive for all regions and ranges ~~but small, ranging~~ from 0.68 ppb to 3.65 ppb. Mean absolute bias ranges from 3.35 ppb to 4.37 ppb.

Since the MDA8 O3 seasonal cycle is a subject of further analysis in this study and forms a key part of our results, it is imperative to perform a more rigorous evaluation of the model's ability to capture its various features quantitatively. Parrish et al. (2016) provide a good precedent for such an evaluation where they break down the observed and modelled ozone seasonal cycle into a y-intercept (detrended annual average) and two sinusoidal harmonics using a Fourier transform and then statistically compare the fit parameters that define these harmonics (i.e. amplitudes and phase angles) for the observed and modelled data. They argue that the first harmonic, with its large amplitude and phase angle, broadly represents the local photochemical production of ozone, while the generally out-of-phase second harmonic, with a smaller amplitude and phase angle, is related to the photolytic loss of O3, driven by $j(O^1D)$ - a hypothesis supported by the finding that the second harmonic is small in the free troposphere but grows more significant in the marine boundary layer (MBL), at least for alpine and remote sites analyzed (Parrish et al., 2020). Thus comparing these Fourier parameters for the observed and modelled data can unveil specific model skill or lack thereof in capturing different aspects of atmospheric chemistry which ultimately determine the shape of O3 seasonal cycle (Bowdalo et al., 2016; Parrish et al., 2016; Bowman et al., 2022). We performed a quantitative evaluation of the seasonal cycles following the same approach. Figure S3 presents scatterplots for these five essential fourier parameters, y0 in ppb (y-intercept representing annual average MDA8 O3 derived from detrended data), A1 in ppb (amplitude of the first or fundamental harmonic), φ1 in radians (phase angle of the fundamental harmonic), A2 in ppb (amplitude of the second harmonic), and φ2 in radians (phase angle of the second harmonic). In terms of y0, the correlation

coefficient r ranges from 0.34 to 0.95, with higher values for southern US but lower values for NW US and Eastern Canada, reflecting lower model skill in capturing the interannual variability of MDA8 O3 in these regions. The model is more skilful in capturing the amplitude of the fundamental harmonic (r values from 0.72-0.93) than in capturing the amplitude of the second harmonic (r values from 0.09-0.90). In terms of phase angles too, the model is more skilful in capturing the phase angles for the fundamental harmonic (r values from 0.63-0.93) than for the second harmonic (r values from 0.41-0.74). The model generally overestimates y0, A1, A2, and φ1 but underestimates φ2. In general we can state that the first harmonic which is related to local photochemistry is well captured by the model for most of North America. The second harmonic, in our case, might be related to all other processes that modify the near-sinusoidal shape of the O3 seasonal cycle (e.g., long range transport of ozone from other regions and from stratosphere and photolytic losses), and these processes are relatively less well captured by the model. All Fourier fit parameters for the observed and modelled MDA8 O3 seasonal cycles have been tabulated in Tables S2-S6 for different North American receptor regions.

The model reproduces the monthly mean MDA8 O_3 for Europe extremely well with very small mean biases (-1.54 ppb to 1.25 ppb), small mean absolute biases (2.18 to 3.54), and very high r values ranging from 0.94 to 0.97 for various regions, except SE Europe~~Southeastern Europe~~. For Western Europe (Figure 4f), it captures both the trends and the structure of the seasonal cycle extremely well, for example, note the near-stagnant maxima and increasing minima over time in both observations and model output. Similarly for Southern Europe (Figure 4g), we again see a very skilful simulation of monthly mean MDA8 for the entire simulation period - this includes capturing the slightly decreasing summer maxima and increasing winter minima and an overall flattening of the seasonal cycle post 2006. We see a very good reproduction of MDA8 O_3 for C&E Europe~~Central & Eastern Europe~~ (Figure 4h) particularly for the summer months. We see a small underprediction for the winter months in years up to 2012. However, it is the summertime MDA8 O_3 values that constitute the peak season ozone metric which are ultimately utilized in our further policy-relevant analyses. Finally, for SE Europe~~Southeastern Europe~~ (Figure 4i), we notice an overprediction of MDA8 O_3 for early years, until 2006, after which the model captures the trends and particularly the summer peaks very well. The mean bias is 7.63 ppb and r value is 0.62.

Similar to North America, we also performed a Fourier transform analysis for European regions which provides a quantitative basis for assessing model skill in reproducing various aspects of the MDA8 O3 seasonal cycle across the 19 year study period. Scatterplots in Figure S4 show high correlations between observed and modelled amplitudes and phase angles for both harmonics. The general high biases, as seen in North American regions, are also not present except for the first harmonic parameters for Western Europe and C&E Europe. This highlights a very high model skill in reproducing the fundamental local ozone photochemistry as well as transport and loss processes in Europe. The y-intercept y0, representing interannual variability of ozone, shows lowest correlations which suggests that year-to-year meteorological changes remain a source of model bias and uncertainty in this region. All Fourier fit parameters for the observed and modelled MDA8 O3 seasonal cycles have been tabulated in Tables S7-S10 for different European receptor regions.

We have also included the Belarus & Ukraine region (Figure 4j; with 1-2 valid stations) in our evaluation and here too we see a good simulation of MDA8 O_3 for the entire period (with a small mean bias of 0.56 ppb and r value of 0.83), barring a couple of years (2014 and 2017) when the model overestimates the values. We have also evaluated the model for MDA8 O_3 against rural observations from the TOAR-II database in other regions including Mexico (11-14 stations), North Africa (1-3 stations), Southern Africa (1 station), Southern Latin America (1-2 stations), and Europea~~Western~~n Russia (2 stations; see Figure 3 for region definitions), where the model has also captured the trends well, however, since we do not discuss these regions in further analyses, they are presented in the supplement (see, Figure S1). Here too, the model output is extracted only from those grid cells where at least one TOAR station exists, ensuring representative co-sampling.

We also evaluate the model in the context of potential overestimation of ozone production from ship plumes. This is because in our modelling setup, ship NOx emissions are instantaneously diluted within the 1.9°×2.5° model grid cell which can lead to an overestimation of ozone production efficiency from ship NOx. In the real world, the more localized, high-NOx conditions within a concentrated young plume, the titration effects and NOx self-reactions can be more dominant and the true ship NOx contribution might be somewhat lower than simulated (Kasibhatla et al., 2000; Chen et al., 2005; Huszar et al., 2010). Such overestimated ship NOx contribution to ozone shows up, for example, in terms of a lower simulated vertical gradient than the observed vertical profile of ozone especially at remote coastal locations. To assess this, we plot observed and model simulated ozone vertical profiles at Trinidad Head, off the coast of California, for the month of July (a representative month for peak season) for all 19 years (see Figure S5). The monthly mean modelled vertical O3 profile over Trinidad Head generally falls within the envelope of daily observational profiles within the MBL (say, below 850 hPa). Although, for multiple years, the vertical drop in modelled O3 concentration towards the surface is less sharp than that seen in observations, thereby suggesting a potential overproduction of O3 near the ocean surface in the model due to instantaneous distribution of ship NOx emissions in the model gridcell. This particular feature of our modelling system can partly explain the positive bias in simulated ozone.

Overall, we obtain very good model-observations agreement, with low biases and high correlations, better than previous studies (e.g., Butler et al., 2020; Li et al., 2023; Garatachea et al., 2024). The possible reasons for such improved performance could be 1) the use of the newly developed HTAPv3 emissions inventory 2) using only rural stations for evaluation which avoids urban titration which may be in the observations but not in model output 3) improved treatment of spatial and temporal representativeness (including the treatment of missing values) of the stations through the TOAR gridding tool 4) evaluating the policy-relevant MDA8 O_3 metric which avoids nighttime O_3 which may not be well-simulated due to improper estimation of the nighttime boundary layer. We note that our model evaluation is based on model results and observations of time series of MDA8 O3 that are averaged, both temporally (monthly) and spatially (first over model grid

cells and then over receptor regions) but such an evaluation is valid because all our subsequent analyses and conclusions depend on the same spatial and temporal scales.

After a satisfactory performance of the model across different world regions and, in particular, excellent performance in the simulation of MDA8 O_3 against rural stations from the TOAR-II database, we proceed to further analyses of trends and source contributions to ozone in different receptor regions. First, to explain the year-to-year trends, we present the full 19-year time series of Peak Season Ozone (PSO) for North America and Europe along with their NO_X- and VOC- source contributions derived from our two tagged simulations. After explaining the year-to-year trends in ozone in terms of the NO_X and VOC contributions, we further calculated a 19-year month-centered average MDA8 O_3 and its source contributions for each receptor region. This allows us to interpret the leading sources of ozone in each receptor region on a monthly basis averaged over the entire simulation period. We also present the first five year (2000-2004) and last five year (2014-2018) ~~then break down this 19-year~~ month-centered average MDA8 O_3 seasonal cycle ~~into a past (first five years) and recent (last five year) averaged seasonal cycle~~ and explain the shifts in terms of tagged contributions for all receptor regions during these periods. In the next subsections, we present these results for North America and Europe.

3.2 Ozone in North America:

3.2.1 Peak Season Ozone in North America: Regional Trends and Source Contributions:

In this section we discuss the trends in and contributions to PSO in North America. The Peak Season Ozone for any location is defined as the highest of the 6-month running average of monthly mean MDA8 O_3 values. In order to compute PSO, we performed the averaging over 6-month windows (Jan-Jun, Feb-July, Mar-Aug and so on) over the TOAR observations and the same time window was imposed over the modelled values for calculating the 6-month averaging (instead of independently selecting the peak 6-month time window for the model). This approach ensures temporal consistency between the observations and modelled values. Furthermore, for spatial consistency, the model values were sampled only from those grid cells where at least one TOAR-II station was present. Finally, these values from multiple grid cells were spatially averaged over various receptor regions after weighting them with the grid cell areas to derive a single PSO value per region per year for observations and the model along with tagged contributions.

Before examining the detailed temporal trends and source contributions to PSO in specific North American receptor regions, it is instructive to visualize the spatial distribution of NOx emissions and their impact on PSO. Figure 5 illustrates the gridded local anthropogenic NOx emissions (panels a, d), the total modelled PSO (panels b, e), and the modeled contribution of local anthropogenic NOx to PSO (panels c, f) for the initial (2000) and final (2018) years of our analysis. The NOx emissions, for each grid cell, are calculated for the same 6-month window as the PSO for the grid cell. In 2000 (Figure 5a), high NOx emissions were concentrated over the Eastern United States, particularly the Ohio River Valley and the Northeast

corridor, as well as in California and other major urban centers. By 2018 (Figure 5d), these emissions had substantially decreased across most of the continent, with the most dramatic reductions evident in the aforementioned historical hotspot regions. This widespread decline in local NOx emissions directly translated to changes in ozone levels. The spatial distribution of total PSO (Figure 5b, e) shows a corresponding general decrease between 2000 and 2018, particularly in the eastern and central US. The spatial features of PSO for both years are very similar to bias-corrected maps of PSO for 2000 and 2017 presented in Becker et al. (2023). More specifically, the contribution of local anthropogenic NOx to PSO (Figure 5c, f) shows a marked reduction in magnitude across the continent. In 2000, local NOx contributed significantly to PSO over large swathes of the eastern and southern US, whereas by 2018, this direct local contribution had diminished considerably, becoming more confined to residual emission hotspots. These spatial changes provide a crucial backdrop for understanding the regionally averaged trends discussed below.

Figure 6 presents the time series of observed and model-simulated total PSO (panels a, d, g, j, m), alongside the attributed contributions from NOx sources (panels b, e, h, k, n) and VOC sources (panels c, f, i, l, o). On a visual inspection of observed and modelled PSO trends (left column panels) we decided to fit Generalized Least Squares (GLS) linear trends to these data points. We note that some previous studies have fitted higher order functions to ozone data over North America as necessitated by their longer period of analysis where ozone concentrations increased, stagnated, and then decreased (Logan et al., 2012; Parrish et al., 2025; Parrish et al. 2020). However, a linear fit is appropriate for the period considered in this study when local emissions have only declined (Figure 2). Quantitative details of the trends and their significance for all contributions are provided in Table 2. A consistent observation across all North American regions is that the observed PSO levels generally exceed the WHO guideline (31 ppb) throughout the study period.

Observed PSO exhibits a decreasing trend in most North American regions (Figure 6, panels a, d, g, j, m). For instance, Eastern Canada shows a slight decline (-0.19 (0.01) [-0.32, -0.06] ppb/yr), while more substantial decreases are seen in the SW US (-0.33 (<0.01) [-0.45, -0.21] ppb/yr), NE US (-0.34 (<0.01) [-0.50, -0.18] ppb/yr), and SE US (-0.46 (<0.01) [-0.63, -0.28] ppb/yr). The NW US shows the smallest, albeit still decreasing, trend (-0.09 (0.11) [-0.20, 0.02] ppb/yr). The model generally captures these decreasing trends and the interannual variability reasonably well, though with some regional differences in magnitude (e.g., an overestimation in the NW US, but good trend reproduction with -0.11 (0.03) [-0.21, -0.01] ppb/yr).

The contributions from various NOx sources show distinct regional patterns in their temporal evolution (Figure 6, panels b, e, h, k, n; Table 2). The most significant driver of change is the local anthropogenic NOx contribution, which has declined steeply across all regions, reflecting successful emission control policies. This decline is particularly sharp in the eastern US regions: NE US (from ~35 ppb to ~22 ppb; trend of -0.97 (<0.01) [-1.19, -0.76] ppb/yr) and SE US (from ~38 ppb to ~20 ppb; trend of -1.09 (<0.01) [-1.25, -0.94] ppb/yr). SW US also shows considerable decline in the local NOx contribution

(from ~27 ppb to ~16 ppb; trend of -0.72 (<0.01) [-0.83, -0.62] ppb/yr) . Despite these reductions, local anthropogenic NOx often remained a dominant contributor, especially in the earlier part of the study period, though its share has notably diminished. These results are consistent with findings from Simon et al. (2024) who analysed observational trends over 51 sites in the US over roughly the same period (2002-2019) and found the marked impact of clean air policies across the US such that the difference between the weekend (lower NOx) and weekday (higher NOx) MDA8 O3 has diminished and become negative in recent years reflecting a transition from NOx-saturated to NOx-limited ozone formation regime.

To further quantify the relationship between these local emissions and their impact on ozone, we performed a gridded correlation analysis for the 2000-2018 period (Figure 7). Figure 7a reveals the temporal correlation between local anthropogenic NOx emissions and total PSO. Positive correlations are widespread, particularly strong (r > 0.6-0.8) over much of the central and eastern US, indicating that in these locations, year-to-year variations in local emissions significantly drive the variability in total PSO levels. However, in other areas, such as parts of the western US and more remote regions, these correlations are weaker or even negative. This suggests a greater relative importance of factors like intercontinental transport of ozone and its precursors, or the influence of natural emissions, in driving total PSO variability in those areas, especially as local anthropogenic emissions have decreased.This lack of correlation between local NOx emissions and observed MDA8 O3 has been reported by Simon et al. (2024) for rural California even at a higher temporal frequency through disappearing day-of-week activity patterns indicating an increasing role of transported ozone in this region.

More directly, Figure 7b demonstrates a very strong and spatially ubiquitous positive correlation (r > 0.8-0.9 in most populated areas) between local anthropogenic NOx emissions and the modeled contribution of these local emissions to PSO. This high correlation is an expected outcome and serves to validate that the model's attribution of ozone to local NOx sources is directly and robustly responsive to changes in those local emissions themselves. It underscores that reductions in local NOx emissions translate directly and proportionally to reductions in the ozone specifically formed from those local emissions within the model framework. The slightly weaker correlations in very remote northern areas likely reflect the minimal anthropogenic emissions and thus lower signal-to-noise for this specific contribution. These spatial analyses highlight that while local NOx emission reductions have been effective in decreasing their direct contribution to PSO across large areas, the impact on total PSO can be spatially heterogeneous due to the varying influence of other ozone sources and transport processes.

Conversely, the contribution from foreign anthropogenic NOx (including aircraft) has generally increased across all regions (Figure 6, panels b, e, h, k, n; Table 2). This increase is most prominent in the western US regions. In the NW US, where its contribution has grown at 0.12 (<0.01) [0.09, 0.16] ppb/yr (see Table 1) to become comparable to, and in recent years exceed, that of local anthropogenic NOx. Similarly, in SW US, the foreign NOx contribution has grown at 0.19 (<0.01) [0.15, 0.24] ppb/yr to match the local NOx contribution in recent years. Other regions like Eastern Canada and the NE US

also show a discernible rise in foreign NOx influence. The contribution from natural NOx sources (biogenic, fire, and lightning) shows a slightly increasing trend in most regions (e.g., 0.12 (<0.01) [0.08, 0.16] ppb/yr in NE US). This increase in contribution despite stable natural emissions (Figure 2) indicates an enhanced ozone production efficiency from these natural NOx sources in environments with lower overall anthropogenic NOx levels, consistent with previous findings (e.g., Liu et al., 1987). Global shipping NOx contributions, while smaller in absolute terms (typically <2-3 ppb), exhibit a consistent increasing trend across all receptor regions, reflecting rising emissions from this sector. Stratospheric intrusion provides a baseline ozone contribution with some interannual variability and small increasing trends in eastern regions (see Table 2).

The attribution of PSO to VOC sources (including methane) also reveals important trends and regional differences (Figure 6, panels c, f, i, l, o; Table 2). Methane is consistently the largest single VOC contributor to PSO across most North American regions, typically contributing 15-25 ppb. Interestingly, despite the global increase in methane concentrations (Figure 2h), the methane contribution to PSO has remained relatively stable or even slightly decreased in some regions like the SW US (-0.10 (<0.01) [-0.15, -0.06] ppb/yr), NE US (-0.09 (<0.01) [-0.15, -0.03] ppb/yr) and SE US (-0.15 (<0.01) [-0.20, -0.11] ppb/yr). This is likely due to the reduced availability of local NOx, which limits the efficiency of ozone production from methane oxidation. Contributions from local AVOC have generally declined across all regions, reflecting the reductions in their emissions as well as the local NOx emission reductions. For example, the NE US saw a local AVOC contribution trend of -0.36 (<0.01) [-0.41, -0.31] ppb/yr, and the SE US experienced a similar decline (-0.33 (<0.01) [-0.37, -0.29] ppb/yr).

The role of natural VOCs (biogenic and fire) varies regionally. In forested regions like Eastern Canada and the NE US, natural VOCs make a substantial contribution (e.g., ~10-18 ppb). The trend in their contribution is often negative (e.g., -0.17 (0.10) [-0.39, 0.04] ppb/yr in Eastern Canada, -0.24 (0.01) [-0.42, -0.06] ppb/yr in NE US), which, similar to methane, may reflect the decreasing local NOx rather than a decrease in natural VOC emissions themselves (which, for North America, Figure 2 shows variability and some recent increases). For all regions, the year-to-year variability in local anthropogenic NOx contributions often mirrors that of natural VOC contributions, suggesting strong chemical coupling between these local precursor pools. In arid regions like the NW US and SW US, the natural VOC contribution is understandably lower (~14-18 ppb initially, declining) than the methane contribution. Contributions from foreign AVOCs, shipping VOCs, and stratospheric intrusion (VOC perspective) are generally smaller and show modest trends, with foreign AVOCs and stratospheric intrusion showing a slight increasing trend in some regions (see Table 1 for p-values and 95% confidence intervals).

Our model-based findings of declining local anthropogenic contributions to PSO in North America differ quantitatively with recent observation-based studies such as Parrish et al. (2025), which also document a significant waning of local influence using different metrics and inferential techniques. For example, Parrish et al. (2025) estimate a local anthropogenic

enhancement to Ozone Design Values (ODVs) in the SW US of typically <6 ppb in recent years. Our direct tagging method quantifies a larger local anthropogenic NOx contribution to average PSO in this region (~16 ppb in 2014-2018, Figure 6h). This quantitative difference likely arises from several factors. First, PSO represents a 6-month seasonal average of MDA8 O3, while ODVs target specific high-percentile episodic conditions, and direct contributions to seasonal averages can be expected to differ from enhancements during specific episodes (although episodic contributions could be expected to have a higher share of local photochemistry than seasonal contributions). Second, and perhaps more fundamentally, inferential methods based on subtracting an estimated 'baseline' from total observed ozone may systematically underestimate the full impact of local anthropogenic emissions. Such approaches often define the baseline based on remote sites or specific statistical filtering, which may not fully account for the ozone produced from local emissions that is then regionally dispersed (as we also see indications of anthropogenic NOx and BVOC interactions in the tagged output) or the non-linear chemical feedbacks that occur when local emissions are present. In contrast, our emissions tagging technique directly attributes ozone formation to its original precursor sources as they undergo transport and chemical transformation within the model's complete and consistent chemical framework. This provides a mechanistic quantification of source contributions to the specific PSO metric under baseline conditions. While inferential methods provide valuable observational constraints, our tagging approach offers a complementary, process-explicit view of how different source categories contribute to the ozone burden, particularly illuminating the partitioning between local, regional, and intercontinental sources in the complex, evolving atmospheric environment

In summary, declining PSO trends across North America are primarily driven by substantial reductions in local anthropogenic NOx and, to a lesser extent, local AVOC contributions. However, these reductions are partially offset by increasing contributions from foreign anthropogenic NOx, shipping NOx, and, in some cases, an enhanced role of natural NOx in ozone formation under lower ambient NOx conditions. Methane remains a cornerstone of VOC-attributed ozone, but its contribution to PSO trends is heavily modulated by NOx availability. The interplay between declining local NOx and the ozone-forming potential of both natural VOCs and methane is a key feature influencing regional PSO trajectories. The NW US stands out as a region where foreign NOx contributions now rival or exceed local sources, highlighting the growing importance of intercontinental transport for this region.

~~Figure 5 shows the observed versus model-simulated time series of Peak Season Ozone along with its NO_X- and VOC-source contributions for five different receptor regions within North America (see Figure 2 for geographic definitions). We note that, for all regions in North America, the observed PSO exceeds the WHO guidelines (31 ppb) throughout the 2000-2018 period. For each row, the left and right panels show the same observed and model-derived PSO in dotted lines for a given receptor region but break it down in terms of the NO_X contributions and VOC contributions respectively, thereby providing us two distinct perspectives of seeing ozone in terms of its contributors. In terms of NO_X contributions, PSO is broken down~~

~~in terms of local anthropogenic NO_X contribution, foreign anthropogenic NO_X contribution which also includes global aircraft contribution, natural NO_X contribution which is a sum of biogenic, fire and lightning NO_X contribution, global shipping NO_X contribution, and stratospheric intrusion, regardless of the origin of the VOCs that interacted with them. It describes 100% of ozone at any given receptor wholly in terms of its NO_X sources only. Similarly, the right-hand panels describe the same ozone in terms of its VOC sources + global methane irrespective of its NO_X sources. Here, the different contributors are, local anthropogenic VOC sources, foreign anthropogenic VOC sources (including global aircraft VOC), natural VOC which is a combination of global biogenic VOCs and fire VOCs, global shipping VOC contribution, methane contribution, and stratospheric intrusion, which again explains the entire 100% of ozone abundance for any given receptor region. Analysing these contributions side-by-side can also provide qualitative insights into possible interactions between different NO_X and VOC sources along with some insights into plausible regional control measures.¶~~

~~¶~~

~~Figures 5 a & b show PSO for Eastern Canada in terms of NO_X and VOC contributions respectively. Overall, we see a slight negative trend in the observed PSO (-0.24 ppb/yr, (1.0)) with magnitudes in the range of 40-45 ppb. The model captures the PSO magnitude well but overestimates the trend (-0.35 ppb/yr, (0.99)). From the NO_X source perspective (Fig 5a), we see that the largest contribution is from local anthropogenic NO_X sources although with a declining trend of (-0.75 ppb/yr, (1.0)) over the 19-year period. The declining trend in the local NO_X contributions is sharper than the trend in overall PSO because all other sources show a small positive trend (see table S1 for details) which partially compensates the negative trend in local NO_X contributions. Despite declining trends, local NO_X remains the largest contributor (~15ppb) to PSO while each of the remaining contributions, though increasing, remain below 10 ppb. In terms of VOC contributions (Fig 5b), methane contribution is largest, at around 15 ppb. This is followed by natural VOC and local AVOC contributions. The declining trend in overall PSO is explained by declining trends in local AVOC contributions (-0.32 ppb/yr, (1.0)) and natural VOC contributions (-0.17 ppb/yr, (0.89)), partially offset by an increasing trend in stratospheric (0.12 ppb/yr, (0.99)) and foreign AVOC contributions (0.09 ppb/yr, (0.99)). It is worth noting that the year-to-year peaks and troughs in the local NO_X contributions correspond neatly with the natural VOC contributions and are also reflected in the overall shape of the PSO time series. This suggests a large interaction between local anthropogenic NO_X and local natural VOCs in the region.¶~~

~~¶~~

~~Figures 5 c and d show PSO time series for the Northwestern United States. We see PSO values around 45 ppb throughout the period but with a slight decreasing trend (-0.11 ppb/yr, (0.82)). The model overestimates the magnitude, for reasons discussed in the previous section, but reproduced the small declining trend very well (-0.11 ppb/yr, (0.97)). In the early years, local anthropogenic NO_X contribution remains the largest but declines steadily (-0.38 ppb/yr, (1.0)) to become comparable to foreign NO_X contributions by 2011. In recent years, the foreign NO_X contribution exceeds the local NO_X contributions. The declining contribution of local NO_X can be linked with the large decline in local NO_X emissions in this region along with a steady increase in northern hemispheric anthropogenic NO_X emissions (see Figure 3). In terms of VOC contributions, methane remains the largest contributor with a steady contribution at around 20 ppb. This is followed by natural VOC~~

~~contributions (10-12 ppb). Here, the overall decline in PSO is almost single handedly associated with the declining trend in local AVOC contributions (-0.15 ppb/yr, (1.0)). This decline can be linked to a combination of the decline in the North American AVOC and NO_X emissions (see Figure 3). There is also a small declining trend (-0.03 ppb/yr, (0.97)) in natural VOC contributions.~~¶

¶

~~Figures 5 e and f show PSO for Southwestern US. Here we see the highest PSO of any other region considered in our analysis, with concentrations reaching 60 ppb in the early years declining at (-0.34 ppb/yr, (1.0)) to reach 55 ppb in 2018, still well above the WHO guideline of 31 ppb. The model slightly overestimates the magnitude but captures the decreasing trend reasonably well (-0.25 ppb/yr, (1.0)). There is a very sharp downward trend (-0.71 ppb/yr, (1.0)) in local NO_X contributions which is partially offset by an increasing trend in foreign anthropogenic NO_X contributions (0.2 ppb/yr, (1.0)). These two together explain the decreasing trend in overall PSO. This region has seen a dramatic reduction in local NO_X emissions such that they were the single largest contributor to ozone in the initial years (up to 27 ppb) with more than double the contributions of foreign NO_X, but in recent years the local NO_X contributions have declined to 16 ppb which is comparable to foreign NO_X and natural NO_X contributions. In terms of VOC contributions, methane remains the largest contributor, at around 25 ppb albeit with a very small decreasing trend (-0.09 ppb/yr, (1.0)). This is remarkable given the rapidly increasing background concentration of methane, but is consistent with the lower availability of local NO_X during methane oxidation for producing ozone. Given the arid climate and sparse vegetation of this region, natural VOC contribution is much lower, at around 14-18 ppb. Similar to Eastern Canada, the stratosphere contributes up to 6-8 ppb, while foreign and local AVOC contributions remain low, beginning at equal strengths at around 5 ppb but followed by a steady decline in local AVOC contribution (-0.25 ppb/yr) as also seen in other parts of the United States.~~¶

¶

~~Figures 5 g and h show PSO time series for Northeastern United States along with its NO_X and VOC contributions respectively. Here, we see a substantial decline in observed PSO (-0.43 ppb/yr, (1.0)) from around 50 ppb in early 2000s down to 45 ppb in 2018. The model overestimates the magnitude but reproduces the declining trend well (-0.52 ppb/yr, (1.0)). From a NO_X source perspective, the PSO decline in this region is driven by a dramatic decline in local NO_X contributions from ~40 ppb to ~20 ppb (-0.94 ppb/yr, (1.0)) which is partially offset by a steadily increasing foreign NO_X (0.17 ppb/yr, (1.0)) and natural NO_X contribution (0.13 ppb/yr, (1.0)). It is notable that the natural NO_X contribution is increasing despite no increase in natural NO_X emissions (see Figure 2) which is consistent with the natural NO_X emissions becoming more productive due to overall lower NO_X levels (Liu et al., 1987). Stratospheric contribution remains low between 4-7 ppb and the ship NO_X contribution is the lowest, 0-2 ppb, albeit with an increasing trend consistent with the increasing shipping NO_X emissions. In terms of VOC contributions, we see comparable contributions from methane and natural VOC, around 18 ppb. The higher natural VOC contribution in this region suggests ample availability of natural VOC through vegetation and also ample local NO_X nearby the natural VOC sources. The peaks and troughs in local NO_X contributions and natural VOC contributions are coincident which also points to their interaction in this region. The~~

~~declining trend in PSO can be explained by the declining local AVOC contribution (-0.37 ppb/yr), natural VOC (-0.25 ppb/yr) and methane contributions (-0.11 ppb/yr) which shows that the ozone produced through the oxidation of VOCs is responding to the declining local NO_X emissions, especially because the natural VOC emissions and methane concentrations, themselves, are rising (Figure 2).~~¶

¶

~~Finally, Figures 5i and j show the PSO time series for the Southeastern US. This region shows the sharpest decline in observed PSO than any other receptor region in North America (-0.47 ppb/yr, (1.0)). The contributions are similar to those in Northeastern US: a sharp decline in local NO_X contribution (38 ppb to 20 ppb; -1.07 ppb/yr, (1.0)) which remains the largest contributor even after the decline, and modest increases in foreign NO_X, natural NO_X and ship NO_X contributions (see Table S1 for quantitative trends). Natural NO_X and foreign NO_X contributions remain around 10 ppb while stratospheric and ship NO_X contributions are under 5 ppb. In terms of VOC contributions, methane and natural VOC contributions are comparable and explain part of the declining trend in PSO (-0.16 ppb/yr, (1.0)) and (-0.33 ppb/yr, (0.9)). The remaining part of the declining trend is captured by a steady decline in local AVOC contribution which reduces from 10 ppb to under 4 ppb over the 19-year period; (-0.33 ppb/yr, (1.0)). Again, the peaks and troughs in natural VOC contribution coincide with those in the local NO_X contribution suggesting their interaction in ozone formation in this region. The quantitative Thiel-Sen trends for observed and modelled PSO in all receptor regions and their tagged contributions are included along with their significance in Table S1.~~ ¶

3.2.2 Ozone seasonal cycle in North America: Quantitative Characterization~~Trends~~ and Source Contributions:

~~Figure 86 shows the 19-year (2000-2018) average seasonal cycle of MDA8 O_3 over the different receptor regions within North America along with its source contributions. We see elevated levels of MDA8 O_3 in spring and summer and lower levels in winter, in line with the scientific understanding of ozone photochemistry (Logan 1985; Seinfeld & Pandis 2016). The model reproduces the 19-year average seasonal cycle over different parts of North America very well. For western regions, we see a consistent systematic positive bias of 2-4 ppb. For eastern regions we see a very good reproduction of the seasonal cycle during winter and spring but a notable overestimation during summertime.~~ ¶

¶

~~Figure 6a and b shows the average seasonal cycle of MDA8 O_3 in Eastern Canada along with its NO_X and VOC source contributions respectively. The MDA8 O_3 seasonal cycle in this region is characterized by a springtime peak (Mar - Apr; ~44 ppb) and a decline in the summertime (Jul - Sep; ~35 ppb). The springtime peak is driven by peaks in foreign anthropogenic NO_X contribution and stratospheric intrusion along with high local NO_X contribution. The summertime peak in the model (not seen in observations) is composed of peaks in local NO_X and natural NO_X. This modelled but not observed peak is likely the reason for the high model bias in this region seen in figure 4. And since the model performs well for springtime, this~~

~~summertime high bias points to nearby emissions being too high, or alternatively, an overactive photochemistry (see also NE and SE US). In terms of VOC contribution, the springtime peak is composed of methane contribution (12-14 ppb), stratospheric intrusion (up to 10 ppb), foreign AVOC contribution peak (8 ppb) and an increasing share of local AVOC contribution (~6ppb). natural VOC contribution peaks in the summertime, when there are more leaves and emissions of natural VOC – this also drives the summer peak in modelled PSO which is not seen in observations. The summertime model-observations gap warrants further investigation into uncertainties in local anthropogenic NO_X as well as local natural VOC emissions to further attribute this mismatch. Methane remains the highest overall contributor in terms of VOCs with slightly higher levels than foreign NO_X contributions suggesting its substantial interaction with both local and foreign NO_X in production of local as well as transported ozone in this region.~~ ¶

¶

~~Figures 6c and d show the average seasonal cycle of MDA8 O_3 in Northwestern US in terms of NO_X and VOC source contributions respectively. Here, we see high MDA8 O_3 from spring through summer in observations. The shape of the seasonal cycle is skilfully captured by the model albeit with a high bias. In contrast to the eastern regions, the bias here is high all year. This points to an overestimation of the background ozone rather than a high bias in local emissions and photochemistry. The spring peak is primarily driven by peaks in foreign NO_X and stratospheric intrusion. Ship NO_X contributions, although small, peak during springtime. Summer highs are driven by highs in local NO_X and natural NO_X contributions. A peculiar feature is a sustained high foreign anthropogenic NO_X contribution throughout the year which only dips in the summertime. This summertime dip in foreign contribution is likely because ozone lifetime is reduced at higher temperatures due to the increased ability of air to hold water vapour (Stevenson et al., 2006) and long-range transported ozone can be destroyed when it encounters moisture (Real et al., 2007). Thus, the overall long-range transport efficiency of ozone is reduced during summertime. A notable feature is the sustained high contribution from foreign anthropogenic NO_X throughout the year, with a distinct dip during summertime. This summertime reduction is likely due to the shorter lifetime of ozone at higher temperatures, which is associated with increased water vapor content in the atmosphere (Stevenson et al., 2006). Water vapor promotes ozone loss via photochemical pathways involving HO_x radicals, and transported ozone is more likely to be destroyed under moist conditions (Real et al., 2007). Consequently, the efficiency of long-range ozone transport decreases in summer. In terms of VOC contributions, springtime peak is primarily composed of methane, stratospheric, foreign AVOC contributions with smaller contributions from natural VOC and local AVOC. Summertime peak is composed of a peak in methane contribution and natural VOC peak. A natural VOC peak is expected during summertime due to a high leaf area during this time of the year. All other VOC contributions are very small during summertime in this region.~~ ¶

¶

~~Figures 6e and f show the average seasonal cycle of MDA8 O_3 in Southwestern US which is similar to that for the Northwestern US and is well reproduced by the model. Springtime peak is dominated by foreign NO_X and stratospheric contributions but also composed of an increasing local NO_X and natural NO_X component. Summertime peak is driven by~~

~~local NO_X and natural NO_X contributions. In terms of VOC contributions, methane, stratosphere and foreign AVOC drive the springtime peak while methane and natural VOC contributions drive the summertime peak.~~ ¶

¶

~~Figures 6g and h show the average seasonal cycle of MDA8 O_3 in Northeastern US which is characterized by a major springtime peak which declines over the summer until the winter months. The model skilfully captures the seasonal cycle for the first five months but overestimates the summertime ozone. Both the NO_X and VOC contributions show a similar cycle as in western US regions except for a very large local NO_X peak (and a corresponding natural VOC contribution peak) which drives the modelled summertime peak not seen in observations. Unlike the western regions, the summertime natural VOC contribution exceeds the methane contribution by a large margin and reaches up to 25 ppb. The higher natural VOC and lower methane contributions broadly correspond with the higher local NO_X and lower remote NO_X contributions. The accuracy of natural VOC emissions in this region is a matter of further investigation. There is also a sustained higher local AVOC contribution (> 5ppb) than in western US.~~ ¶

¶

~~Figures 6i and j show the average seasonal cycle of MDA8 O_3 in the Southeastern US which is very similar to that in the Northeastern US. The model reproduces the observed seasonal cycle well although with an overestimation of the summer peak. The shape of the seasonal cycle is primarily driven by local anthropogenic NO_X contributions from a NO_X perspective and by methane and natural VOC contributions from the VOC perspective. Foreign anthropogenic NO_X contributions are high, up to 10 ppb, during spring and winter but dip to around 5 ppb in the summer.~~¶

To characterize the climatological seasonal cycle of MDA8 O3 in North America and assess the model's ability to reproduce it, we performed a Fourier analysis (as detailed in section 3.1) on the 19-year (2000-2018) averaged month-centered mean MDA8 O_3 time series for both observations and model output in each receptor region. This analysis decomposes the climatological seasonal cycle into its annual mean (y0), the amplitude (A1) and phase (φ1) of the fundamental annual harmonic (related to local ozone photochemistry), and the amplitude (A2) and phase (φ2) of the second harmonic (semi-annual cycle; related to long-range transport, stratospheric intrusion and loss processes). The phase φ_1 indicates the timing of the annual peak, with numerically larger values typically corresponding to a later peak in the year (Bowdalo et al., 2016; Parrish et al., 2016; Bowman et al., 2022). These parameters are presented in the last rows of Tables S2-S6, while Figure 8 illustrates the 19-year average seasonal cycle of total MDA8 O_3 and its attributed NOx and VOC source contributions.

The observed annual mean MDA8 O_3 (y0) varies across North American regions, ranging from approximately 37 ppb in Eastern Canada to a notably higher 48.5 ppb in the SW US, reflecting differing baseline ozone levels and regional influences (Tables S2-S6). The model generally captures these mean levels, though with a tendency for overestimation. For instance, in Eastern Canada, the modeled y0 (37.66 ppb) is very close to observed (36.93 ppb). However, in western regions, the model

exhibits a consistent positive bias of approximately 3-4 ppb in y0 (e.g., 44.09 ppb modeled vs. 40.83 ppb observed in NW US). This suggests a potential overestimation of background ozone or the combined influence of persistent remote/natural source contributions by the model in these regions. Indeed, Figure 8 (panels d, f) shows sustained contributions from foreign anthropogenic NOx and methane in the NW US throughout the year, which could contribute to this higher baseline in the model.

The amplitude of the primary annual cycle (A1) signifies the magnitude of the seasonal swing in ozone concentrations. Observed A1 is largest in the SW US (11.25 ppb) and the NE US (9.3 ppb), indicating strong seasonal variation driven by photochemistry and precursor availability. Eastern Canada shows the smallest observed A1 (5.86 ppb). The model tends to overestimate A_1 in most regions, particularly in the eastern regions. For example, in the NE US, the modeled A1 (14.89 ppb) is substantially larger than observed (9.3 ppb), and in Eastern Canada, modeled A1 (9.89 ppb) is also significantly higher than observed (5.86 ppb). This overestimation of A1 in eastern regions is due to the model simulating an overly pronounced summer peak, likely due to an overestimation of summertime local photochemical production, as suggested by the pronounced summer peaks in modeled local NOx and natural VOC contributions (Figure 8a,b for E.Canada; 8g,h for NE US) which are not as prominent in the observed seasonal cycle implied by the total ozone. In contrast, for SW US, the modeled A1 (10.66 ppb) is slightly lower than observed (11.25 ppb), suggesting a slightly damped seasonal cycle in the model for this high-ozone region.

The phase of the annual cycle (φ_1), which dictates the timing of the seasonal maximum, shows regional differences. Observed φ_1 values range from 4.82 radians in Eastern Canada to 5.44 radians in SW US (Tables S2-S6, last rows). Higher φ_1 values suggest a later seasonal peak. The model generally reproduces the phase well, with modeled φ_1 values closely tracking the observed ones, indicating that the model captures the relative timing of the ozone maximum across regions correctly. For instance, in Eastern Canada, the observed (4.82 rad) and modeled (5.36 rad) φ_1 values, while differing, both point towards an earlier peak (spring, as seen in Figure 8a) compared to SW US (observed 5.44 rad, modeled 5.47 rad) which exhibits a clear summer maximum (Figure 8e). The springtime peak in Eastern Canada (Figure 8a) is driven by significant contributions from foreign anthropogenic NOx and stratospheric intrusion, while the summertime peak in SW US (Figure 8e) is dominated by local NOx and natural NOx contributions. The model's ability to capture these phase differences reflects its capacity to simulate the varying dominance of these seasonally distinct drivers.

The amplitude of the second harmonic (A2), representing semi-annual variations driven by processes other than the local ozone photochemistry, is generally smaller than A1 but provides insights into deviations from a simple sinusoidal annual cycle, such as the presence of distinct spring and summer maxima or a flattened peak. Observed A2 is most prominent in the SE US (3.32 ppb) and Eastern Canada (1.89 ppb), suggesting more complex seasonality than a single peak. The model tends to reproduce or even slightly overestimate A_2 (e.g., 3.78 ppb vs. 3.32 ppb in SE US; 2.07 ppb vs. 1.89 ppb in E. Canada). A

significant A2 can indicate a broadening of the peak ozone season or the influence of multiple processes peaking at different times (e.g., a spring transport peak and a summer photochemical peak). The model's higher A2 in regions like NE US (3.11 ppb modeled vs. 1.58 ppb observed) may again be linked to its overestimation of the summer photochemical peak, which, when combined with a reasonably simulated spring shoulder, could enhance the semi-annual component. The phase of the second harmonic (φ_2) varies, and its interpretation is complex, but model agreement with observed φ_2 is mixed, indicating varying skill in capturing these finer details of seasonal shape.

The quantitative Fourier parameters align well with the qualitative features observed in the source contributions (Figure 8). For Eastern Canada (Fig 8a,b), the relatively low y0 and A1 (observed) are consistent with lower overall photochemical activity and a seasonal cycle strongly influenced by springtime transport (foreign NOx and stratosphere; ~10 ppb each) rather than a dominant summer photochemical peak. The model's overestimation of A_1 here is driven by a simulated summer peak in local NOx and natural NOx/VOC contributions not evident in the overall observed seasonal structure, leading to the noted summertime bias.

For NW US (Fig 8c,d), the moderate y0 and A1 reflect a balance of influences: the model captures the year-round high foreign NOx contribution, with a summertime dip, contributing to y0, while local NOx and natural NOx/VOCs drive the summer high, contributing to A1. The summertime dip in foreign NOx contribution (also seen in other sub-regions) is likely due to shorter lifetime of ozone at higher temperatures, which is associated with increased water vapor content in the atmosphere (Stevenson et al., 2006). Water vapor promotes ozone loss via photochemical pathways involving HO_x radicals, and transported ozone is more likely to be destroyed under moist conditions (Real et al., 2007). Consequently, the efficiency of long-range ozone transport decreases in summer. The consistent positive bias in y0 in the model suggests an overestimation of these baseline contributions. For SW US (Fig 8e,f), the highest observed y0 and a large A1 are characteristic of this photochemically active region with significant local precursor influence in summer (local and natural NOx driving the summer peak). Methane is a dominant VOC contributor throughout the year. The model reproduces this structure well, including the dominance of local/natural NOx in summer. For NE US (Fig 8g,h), a large observed A1 reflects strong seasonality. The model overestimates this A1 due to a very pronounced modeled summer peak in local NOx and, consequently, natural VOC contributions, leading to summertime overestimations. Unlike western regions, natural VOCs play a more significant role than methane during the summer peak in this region according to the model, likely due to higher BVOC emissions in these regions as well as more local NOx availability enhancing their ozone production efficiency. SE US (Fig 8i,j), similar to NE US, shows a strong seasonal cycle (large A1). The model again overestimates A1 due to an exaggerated summer peak driven by local NOx and associated natural VOC chemistry. The significant A2 in observations and model suggests a broader ozone season or influences from both spring transport and summer photochemistry.

Overall, the model successfully reproduces the primary features of the 19-year average MDA8 O_3 seasonal cycle across North America, including the relative annual mean levels (y0) and the timing of the annual peak (φ_1). However, it tends to overestimate the amplitude of the annual cycle (A_1) in eastern regions, linked to summertime photochemical production. In western regions, a modest positive bias in the annual mean (y0) is observed. These findings highlight areas for further model refinement, particularly concerning the simulation of summer photochemistry and baseline ozone levels in different continental sub-regions.

3.2.3 Changes in seasonal cycle of ozone in United States: Role of Local vs Remote contributions

~~A careful analysis of the dominant contributors to MDA8 O_3 seasonal cycle for different months (Figure 8) alongside the changing dominant contributors to PSO over the two decades (Figure 6) suggests that the seasonal cycle as well as its composition must be changing significantly over the years. This led us to plot full envelopes of MDA8 O_3 cycles (instead of averages) to fully assess the changes in the shape of the O_3 seasonal cycle for different receptor regions. These envelope plots are shown in the supplement (Figure S2) which reveal the changes in the MDA8 O_3 seasonal cycle year-to-year. In Figure S2, we note that generally the spring and summertime MDA8 O_3 is decreasing while the wintertime O_3 is increasing for many regions which is consistent with decreasing local anthropogenic NO_X emissions reducing titration in winter and local production in summer. The wintertime ozone increase could also be partly due to increasing transported ozone from foreign contributions.~~ ¶

¶

~~To better understand how the seasonal cycle has changed over these two decades, we present the initial and final 5-year averaged MDA8 O_3 seasonal cycles (over 2000-2004 and 2014-2018, respectively) along with their NO_X and VOC contributions. Figures 7 a and d show the observed and modelled initial 5-year and final 5-year average seasonal cycles for Northwestern US. We see that between these two periods, the spring and summertime ozone has decreased while the wintertime ozone has increased. The model reproduces these seasonal changes reasonably well but with a high bias of up to 4 ppb. We see (in Figs 7b and e) that these changes in the seasonal cycle are driven by a substantial drop in local NO_X contributions especially in the summer along with an increase in summertime natural NO_X contribution which partially compensates for the drop in local anthropogenic NO_X contributions. As noted in the previous sections, there is no increase in the natural NO_X emissions in these two decades (Figure 2) however, under lower NO_X conditions, the same natural NO_X becomes more productive in forming ozone during summer (see Liu et al., 1987). The wintertime increases are primarily driven by an increased foreign NO_X contribution along with a small increase in ship NO_X contribution. From a VOC perspective (Figs 7c and f), the biggest changes occur in the local AVOC contributions which have declined throughout the year (probably in response to the declining local NO_X emissions but also a decline in their own emissions; see figure 2).~~

~~Wintertime increase in MDA8 O_3 is composed of increases in methane and foreign AVOC contributions in winter. Summertime decrease is associated with a decrease in methane and local AVOC contributions in the summer.~~ ¶

¶

~~Figure 8 shows a similar analysis but for Northeastern US. Here, in the observed seasonal cycle, we see a small decrease in springtime ozone (~48 ppb to ~45 ppb), a large decrease in summertime (~48 ppb to ~40 ppb), and an increase in wintertime ozone (28-32 ppb to 30-36 ppb). For the initial 5-year period, the model overestimates the summertime peak by a large margin (~10 ppb) and underestimates the wintertime levels by 4-8 ppb. This is likely due to high anthropogenic NO_X over this region in the HTAPv3 emissions dataset and has also been discussed in the model evaluation section (see section 3.1 and Figure 3c). The model captures the seasonal cycle for the final 5-year period much better over the winter and spring seasons but the summertime overestimation remains. However, the model is able to capture the directional changes in the seasonal cycle: small decrease in spring, large decrease in summer and an increase in winter. These changes can be understood in terms of decreasing summertime local NO_X contributions and increasing wintertime and springtime foreign NO_X contributions (Figs 8b and c). From a VOC point of view, the summertime drop is primarily due to a large drop in local AVOC contributions and to a lesser extent in natural VOC contributions, while the wintertime increase is due to an increase in methane contributions. We have performed a similar analysis for other receptor regions within North America which can be found in the supplement (Figures S3-S5). Our results are in agreement with observational studies which have also reported a decline in summer peaks and a shift in peak ozone to the springtime in North America (Bloomer et al., 2010; Parrish et al., 2013; Cooper et al., 2014). For the first time, through our tagging technique, we are able to explain these changes in terms of NO_X and VOC source contributions from local and remote regions. It is crucial to note the increased share of foreign NO_X contributions to springtime ozone which coincides with the growing season and highlights the increasing impact of transported ozone on crop yields (Dingenen et al., 2009; Avnery et al., 2011).~~ ¶

¶

The preceding analyses of 19-year average seasonal cycles (Figure 8) and long-term PSO trends (Figure 6) suggest significant evolution in the seasonality of surface ozone over the two decades (see Figure S2 for seasonal cycle envelopes over the entire period). To investigate these changes more quantitatively, we compare the 5-year averaged MDA8 O3 seasonal cycles for an initial period (2000-2004) and a recent period (2014-2018). This section focuses on two illustrative regions, the NW US and NE US, with Fourier analysis parameters for these periods detailed in Tables S3 and S4, respectively (and for other regions in Tables S2, S5-S6 in the Supplement). Figures 9 and 10 present these comparative seasonal cycles for NW US and NE US, respectively, alongside their attributed NOx and VOC source contributions. Results for Eastern Canada, SW US and SE US are included in the supplement (Figures S6-S8; Tables S1, S4-S5).

In the NW US (Figure 9, Table S2), the evolution of the seasonal cycle from 2000-2004 to 2014-2018 is characterized by subtle but distinct changes. The observed annual mean ozone (y0) decreased slightly from 41.43 ppb to 40.64 ppb, while the modeled y0 remained relatively stable at a higher level (43.54 ppb to 43.87 ppb), maintaining the positive bias noted earlier. More significantly, the amplitude of the primary annual cycle (A1) shows a marked decrease in both observations (from 6.50 ppb to 5.24 ppb) and the model (from 9.01 ppb to 5.33 ppb). This indicates a notable damping of the seasonal swing. Concurrently, the observed phase of the annual peak (φ_1) shifted slightly earlier, from 5.22 radians to 5.18 radians, a trend also captured by the model (5.43 to 5.33 radians). The amplitude of the second harmonic (A2) also decreased, particularly in the observations (1.08 ppb to 0.29 ppb), suggesting a smoother, less complex seasonal shape in the recent period.

These quantitative changes are driven by shifts in precursor contributions (Figure 9b,c,e,f). The most prominent change is the substantial reduction in the summertime peak of local anthropogenic NOx contributions between the two periods (Figure 9b vs. 9e). This directly contributes to the decreased A1. While this local contribution shrinks, the foreign anthropogenic NOx contribution remains a significant and relatively stable component throughout the year, becoming proportionally more important, especially during spring; a finding consistent with a long line of previous studies (Berntsen et al., 1999; Jacob et al., 1999; Jaffe et al., 1999; Fiore et al., 2002; Jaffe et al., 2003; Parrish et al., 2004; Cooper et al., 2010; Simon et al., 2014; Parris & Ennis, 2019; Parrish et al., 2022; Christiansen et al., 2022). The wintertime ozone levels show a slight increase (Figure 9a vs. 9d), primarily linked to an increase in the modeled foreign NOx contribution during these months in the later period. The springtime (March-May) ozone has seen increases in both foreign NOx contributions (13.16 ppb to 14.81 ppb) as well as stratospheric contributions (12.02 ppb to 12.55 ppb; see Table 3 for a comparison across regions). Springtime mean stratospheric contribution is 12.55 ppb in the recent period (even higher in SW US at 14.25 ppb; Figure S7; Table 3). Previous studies have reported modelled stratospheric contributions in North America during observationally-identified episodes with higher values (e.g., 20-40 ppb; Lin et al., 2012) as well as seasonal mean contributions (6-18 ppb; Mathur et al. 2022b). Our seasonal mean values are lower likely because we do not sample the model output extensively from the mountainous region of western US, where stratospheric contributions are highest, due to lack of TOAR observations in those regions.

From a VOC perspective (Figure 9c vs. 9f), the local AVOC contribution declined across all seasons, further contributing to the damping of the seasonal cycle (reduced A1). Methane remains a dominant VOC contributor, but its absolute contribution shows little change between the periods, suggesting its impact on seasonal amplitude is more modulated by NOx availability than by its own concentration changes over this timeframe. The decrease in natural VOC contribution, particularly in summer, also plays a role in reducing A1. The overall effect is a flattening of the summer peak and a slight elevation of winter/spring troughs, leading to the observed and modeled decrease in A1.

The NE US (Figure 10, Table S3) experienced more dramatic changes in its ozone seasonal cycle. The observed annual mean (y0) decreased from 40.35 ppb to 38.29 ppb. In contrast, the modeled y_0 remained remarkably stable (41.06 ppb to 41.13 ppb), causing the model's initial slight positive bias to increase in the later period, particularly as observed wintertime values increased more than modeled ones. The most striking change is the substantial reduction in the amplitude of the annual cycle (A_1), both in observations (from 11.85 ppb to 6.70 ppb) and even more so in the model (from a highly overestimated 20.01 ppb to 9.26 ppb). This signifies a major reduction in the summer peak. The phase of the annual peak (φ_1) also shifted significantly earlier in observations (from 5.40 radians to 5.01 radians), indicating a pronounced shift of the seasonal maximum from summer towards spring. The model also simulates an earlier peak (5.59 to 5.44 radians), though the shift is less pronounced than observed, and the model still peaks later than observations in the recent period. The amplitude of the second harmonic (A2) increased in observations (1.31 ppb to 2.17 ppb) but decreased in the model (3.94 ppb to 2.31 ppb), suggesting evolving complexity in the seasonal shape that the model captures with mixed success.

These transformations are clearly linked to changes in NOx and VOC contributions (Figure 10b,c,e,f). The dramatic decrease in A1 is primarily due to a large reduction in the summertime contribution from local anthropogenic NOx (Figure 10b vs. 10e). This local NOx peak, which was very pronounced in 2000-2004 (contributing ~35-45 ppb in the model during summer), is significantly curtailed in 2014-2018 (contributing ~15-20 ppb in summer). While the model still appears to overestimate this summer local NOx contribution in the later period (as suggested by a visual inspection of Figure 10d as well as the still present overestimation of A1), the reduction is substantial. Concurrently, winter and spring ozone levels have increased (Figure 10a vs. 10d). This is partly due to reduced wintertime titration by lower local NOx, but also, as seen in the model (Figure 10e), an increase in the foreign anthropogenic NOx contribution during spring (8.30 ppb to10.83 ppb) and winter months (see section 3.4 for a detailed analysis) as well as an increase in the stratospheric contributions (7.58 ppb to 11.00 ppb; see Table 3). This increased foreign and stratospheric influx in spring, combined with the diminished summer photochemical peak, explains the observed shift in φ_1 towards an earlier (springtime) maximum.

From the VOC perspective (Figure 10c vs. 10f), the summertime drop is driven by a large decrease in local AVOC contributions and a significant reduction in the contribution from natural VOCs. The latter is likely a consequence of the reduced local NOx, making the natural VOCs less efficient at producing ozone, given that there is no correspondingly large decreasing trend in the BVOCs (Figure 2). The wintertime increase in ozone is associated with an increased modeled contribution from methane, alongside the foreign AVOCs.

The quantitative analysis of seasonal cycle changes in NW US and NE US highlights the profound impact of declining local anthropogenic NOx emissions. In both regions, this has led to a significant reduction in the amplitude of the annual ozone cycle (A1), particularly by lowering summer peaks. Wintertime ozone levels have generally increased, partly due to reduced titration and partly due to increased contributions from remote sources like foreign anthropogenic NOx and methane. The

NE US exhibits a more pronounced shift, with a dramatic decrease in the summer peak and a clear move towards a spring-dominated seasonal maximum (earlier φ_1), a finding also reported by previous observation-based studies (Bloomer et al., 2010; Parrish et al., 2013; Cooper et al., 2014). This underscores the increasing relative importance of long-range transport in spring as local summer production wanes. This transition in the ozone seasonal cycle in the NE US, towards a springtime maximum, is expected to continue with future emissions changes, as discussed by Clifton et al. (2014). While the NW US also sees a damped cycle, its baseline remains more consistently influenced by foreign NOx throughout the year. Our tagging technique, combined with Fourier analysis, allows for a quantitative attribution and evaluation of these changes. The increased share of foreign NOx and methane in contributing to springtime ozone, which coincides with the agricultural growing season, highlights the impacts of intercontinental transported ozone on crop yields (Dingenen et al., 2009; Avnery et al., 2011) and ecosystem health, even as local emissions are successfully reduced.

3.3 Ozone in Europe:

Here, we present the observed and model-derived results for different sub-regions in Europe: Western Europe, Southern Europe, C&E Europe~~Central & Eastern Europe~~, and SE Europe~~Southeastern Europe~~ (see Figure 2 for geographical extents). We first present trends in PSO along with their NO_X and VOC contributions~~, and~~ then show the 19-year average seasonal cycle of MDA8 O_3 and its source contributions, and finally present changes in the seasonal cycle between initial and the final five years. Europe has undergone significant reductions in NO_X emissions over the past decades (see Figure 2~~3~~), particularly in Western and Southern Europe (see Figure 11). However, some countries in Central and Eastern Europe have not yet achieved the same level of reductions, suggesting potential variability in ozone trends across the continent. This raises important questions about how these uneven NO_X reductions might influence ozone formation dynamics in different sub-regions, which we~~ will~~ explore in detail in this section using our tagged model results.

3.3.1 Peak Season Ozone in Europe: Trends and Source Contributions:

~~Figure 9 shows the observed and modelled PSO in different regions of Europe along with the corresponding NO_X and VOC source contributions. We note that despite the large decline in European anthropogenic NO_X and NMVOC emissions (Figure 2) over the two decades, the observed PSO values exceed the WHO guidelines in all regions.¶~~

~~¶~~

~~Figures 9 a and b show the observed and modelled PSO for Western Europe along with its NO_X and VOC contributions respectively. The model does a near-perfect job of reproducing the magnitude and trend of the observed PSO (see Table S1 for quantitative trends). It also captures the high PSO for 2003 and 2006 which were associated with summertime heatwaves in Europe (Vautard et al., 2005; Solberg et al., 2008; Struzewska & Kaminski, 2008). We do not see any significant trends in the PSO for this region over the 19-year period. There is a decline in the local NO_X contribution (-0.26 ppb/yr, (1.0)) but it is~~

~~partially compensated by small increasing trends in foreign NO_X (0.06 ppb/yr, (0.99)) and ship NO_X (0.12 ppb/yr, (1.0)) contributions. These results demonstrate that the local NO_X emission controls did not translate into the local air quality improvement in this region, at least in terms of the policy-relevant PSO metric. Although, other studies have highlighted that summertime ozone extremes have been reduced in recent decades (Yan et al., 2018; Crespo-Miguel et al., 2024). From the VOC perspective, methane is the largest contributor at around 18 ppb with an increasing trend (0.08 ppb/yr, (1.0)) which is followed by natural VOC, stratosphere, foreign AVOC and local AVOC contributions in that order, all contributing between 4-10 ppb. The small declining trend in PSO is mainly captured by a declining trend in the local AVOC contributions (-0.16 ppb/yr, (1.0)) while other VOC contributions show modest trends (see Table S1 for details).~~ ¶

¶

~~Figures 9 c and d show the observed and model-derived PSO for Southern Europe along with its NO_X and VOC contributions respectively. The model captures the magnitude and trend of PSO extremely well. Here, we see a gentle decline in observed PSO (0.04 ppb/yr, (0.52)) from ~50 ppb in early years to ~46 ppb in 2016, albeit with an uptick in the final two years. The model captures the trend well for a large part of the time series but overestimates the overall decline (-0.17 ppb/yr, (0.98)). This declining trend is driven by a noticeable decline in local NO_X contribution (-0.51 ppb/yr, (1.0)) partially compensated by increasing trends in foreign NO_X (0.07 ppb/yr, (0.98)) and ship NO_X (0.16 ppb/yr, (1.0)) contributions. Despite the decline, local NO_X remains the largest contributor throughout the year, at 25 ppb in 2000 and 19 ppb in 2018. The large gap between the local NO_X and foreign NO_X contributions in early years has narrowed in recent years – and foreign anthropogenic NO_X contributions are becoming an important source of transported ozone in this region. In terms of VOC contributions, methane and natural VOC remain the largest contributors. The variability in the PSO time series corresponds with the variability in local NO_X contributions in the left panel and natural VOC contributions in the right panel, suggesting their interaction. From a VOC perspective, the declining PSO trend is mainly associated with declining local AVOC contributions (-0.22 ppb/yr, (1.0)).~~ ¶

¶

~~For Central & Eastern Europe (Figures 9 e and f), we see a noticeable negative trend of -0.43 ppb/yr (1.0) in the observed PSO. The model captures the PSO magnitude well but with a small underestimation for the early years and overestimation for the later years, which leads to a smaller negative modelled trend of -0.04 ppb/yr (0.47). Similar to Southern Europe, local NO_X contributions are the largest contributor but with a consistent decline (-0.27 ppb/yr, (1.0)) while foreign NO_X contributions are increasing (0.1 ppb/yr, (0.99)). Other contributions remain small. The VOC contributions are very similar to those seen in Southern Europe where the declining PSO trend is primarily captured by a decline in local AVOC contributions (-0.18 ppb/yr, (1.0)) which is consistent with both decreasing emissions of AVOC and decreasing availability of NO_X for ozone production (Figure 2).~~ ¶

¶

~~Finally, Figures 9 g and h show PSO time series for Southeastern Europe along with its NO_X and VOC contributions respectively. Here, we see a large model-observations gap for the early years which narrows and closes towards the later~~

~~years. There is considerable year-to-year variability in the observations which is not reproduced in the modelled results. This could be due to the complicated nature of model sampling from TOAR-valid grid cells which are changing from year-to-year while the number of stations within a grid cell are also changing rapidly in the region. We have explored the TOAR station-network for each of the receptor regions and plotted the number of valid stations per region as a time series in Figure S8. We see that Southeastern Europe only had 1-3 rural stations in the initial years which increased to up to 20 stations towards the end. Such a rapidly changing station network, especially when happening within a model grid cell, can complicate the model-observation agreement and interpretation. Due to these sampling issues, we do not overinterpret the results for this region. Instead, we refer the reader to Lin et al., (2015) for a discussion on the dependence of the modelled ozone trends on the co-sampling with observations.¶~~

Figure 12 shows the observed and modelled PSO in different sub-regions of Europe along with the corresponding NOX and VOC source contributions. We note that despite the large decline in European anthropogenic NOX and NMVOC emissions (Figure 2) over the two decades, the observed PSO values exceed the WHO guidelines (31 ppb) in all regions. To understand the geographical backdrop of PSO changes, Figure 11 presents a spatial map of local anthropogenic NOx emissions (panels a, d), total PSO (panels b, e), and the modeled contribution of local anthropogenic NOx to PSO (panels c, f) for the initial (2000) and final year (2018). In 2000 (Figure 11a), prominent NOx emission hotspots were evident (e.g., Benelux, Germany, Po Valley), parts of the UK, and major urban agglomerations across the continent. By 2018 (Figure 11d), substantial emission reductions occurred, particularly in Western and Central Europe. However, this decline is not obviously reflected in the spatial patterns of total PSO (Figure 11b, e), which generally decreased in the southern regions but not in northern regions, especially over areas with the largest emission cuts, as also seen in bias-corrected PSO maps by Becker et al. (2023). The direct contribution of local anthropogenic NOx to PSO (Figure 11c, f) mirrors these emission reductions more closely, with clear reductions from 2000 to 2018. This suggests the role of other contributions in offsetting the expected decline in PSO, especially in northern European regions.

Observed PSO time series (Figure 12, panels a, d, g, j) reveal diverse trends across Europe (see Table 2). Western Europe exhibits no significant long-term trend in observed PSO, despite a clear decline in local NOx contributions. This region notably experienced high PSO during the 2003 and 2006 heatwaves (Vautard et al., 2005; Solberg et al., 2008; Struzewska & Kaminski, 2008), events which the model captures. Southern Europe shows a slight overall decline in observed PSO (-0.09 (0.45) [-0.33, 0.15] ppb/yr, Table 2), though with an uptick in the final years. C&E Europe displays a more pronounced decreasing trend in observed PSO (-0.40 (<0.01), [-0.58, -0.22] ppb/yr). The model's performance in reproducing these trends varies: it captures the lack of trend in Western Europe and the declining trend in Southern Europe (albeit overestimating the declining trend; -0.20 (0.01) [-0.35, -0.06] ppb/yr), but simulates a much weaker or even insignificant decline in C&E Europe than observed. SE Europe presents a challenge for PSO trend interpretation due to lack of sufficient observational stations for most of the study period (see Figure S11). Due to these sampling issues, we do not overinterpret

the results for this region. Instead, we refer the reader to Lin et al., (2015) for a discussion on the dependence of the modelled ozone trends on the co-sampling with observations. Our results are in general agreement with the findings of Yan et al. (2018) who found insignificant trends for mean ozone but declining trends for the 95th %ile ozone in Europe during spring-summer.

The evolution of NOx contributions to PSO (Figure 12, panels b, e, h, k; Table 2) is key to understanding European PSO trends. Local anthropogenic NOx contributions (red lines) have declined significantly across all European regions. In Western Europe, this decline (-0.28 (<0.01) [-0.38, -0.18] ppb/yr) is offset by increases in other contributions, leading to a flat overall PSO trend. This quantitatively demonstrates that while local NOx emission controls have reduced direct local ozone production, other contributions have compensated. In Southern Europe, the more stringent decline in local NOx contribution (from ~25 ppb in 2000 to ~19 ppb in 2018) is the primary driver of the overall PSO decrease. C&E Europe also shows a substantial decline in local NOx contribution (-0.28 (<0.01), [-0.36, -0.20] ppb/yr).

The relationship between local NOx emissions and PSO is further illuminated by the correlation analysis in Figure 13. The gridcell-level correlation between local anthropogenic NOx emissions (averaged over the corresponding 6-month PSO window per year) and total PSO (Figure 13a) is moderately positive over large parts of Central and Southern Europe (r ~ 0.4-0.7), but weaker or even negative in parts of Western and Northern Europe. This indicates that while local emissions are a factor, total PSO in the northern belts of Europe is highly susceptible to other influences. In contrast, the correlation between local NOx emissions and their direct contribution to PSO (Figure 13b) is very high (r > 0.7-0.9) across most of Europe. This confirms the model's source attribution capability and reinforces that reducing local NOx directly curtails its specific ozone yield.

Foreign anthropogenic NOx contributions have shown small increases across Europe (e.g., 0.04 (0.03) [0.00, 0.07] ppb/yr in Western Europe, 0.07 (0.01) [0.02, 0.13] ppb/yr in S Europe, 0.08 (<0.01), [0.04, 0.13] ppb/yr in C&E Europe), offsetting the benefits of local reductions (Figure 12, panels b, e, h, k; Table 2). Global shipping NOx contributions also show a consistent increasing trend across all European regions (e.g., 0.12 (<0.01) [0.10, 0.14] ppb/yr in Western Europe, 0.16 (<0.01) [0.14, 0.19] ppb/yr in Southern Europe), reflecting rising maritime emissions and their growing impact on coastal and inland air quality. Contributions from natural NOx sources are also rising (see Table 2) despite the lack of a significant increase in natural NOx emissions (Figure 2) suggesting an increased ozone production efficiency by these emissions in a lower-NOx environment, as also noted in North American regions. Stratospheric intrusion remains relatively small and a stable contributor to PSO without any significant trends (Table 2).

The VOC source contributions to PSO (Figure 12, panels c, f, i, l; Table 2) reveal the significant role of methane and the impact of local emission changes. Methane is the largest VOC contributor to PSO across all European regions, typically

around 15-20 ppb. Its contribution generally shows a slight increasing trend (e.g., 0.08 (<0.01) [0.05, 0.11] ppb/yr in Western Europe), consistent with rising global methane concentrations, though this increase is modest compared to the overall PSO levels. Contributions from local AVOC have declined in all regions, mirroring reductions in their emissions and contributing to the overall PSO decrease where observed. For example, in Western Europe, local AVOCs declined by -0.17 (<0.01) [-0.21, -0.12] ppb/yr, and in Southern Europe by -0.21 (<0.01) [-0.25, -0.16] ppb/yr. This decline is consistent with reduced availability of both AVOCs and local NOx for ozone formation. Natural VOCs (from biogenic and fire emissions) are the second most important VOC contributors after methane. Their absolute contribution varies, but like methane, their ozone production capacity is linked to NOx availability. The interaction between local anthropogenic NOx and natural VOCs is evident in all regions, where variability in the contribution from these two sources is highly similar. Foreign AVOCs, shipping VOCs, and stratospheric intrusion (VOC perspective) are smaller contributors, with foreign AVOCs and stratospheric components generally stable.

3.3.2 Ozone seasonal cycle in Europe: Quantitative Characterization~~Trends~~ and Source Contributions:

Figure 14 shows the 19-year average seasonal cycle of MDA8 O_3 for different sub-regions of Europe along with its NO_X and VOC source contributions. The observed seasonal cycle is distinct in each receptor region: we see a major spring peak in Western Europe, a sustained spring-to-summer peak in Southern Europe and C&E Europe~~Central & Eastern Europe~~, and a major summer peak in SE Europe~~Southeastern Europe~~. The model reproduces the average seasonal cycles in these regions ~~extremely~~ reasonably well, particularly in Western and Southern Europe. The model underestimates the MDA8 O_3 for C&E Europe~~Central & Eastern Europe~~ in winter months and systematically overestimates the full seasonal cycle for SE Europe~~Southeastern Europe~~.

~~For all regions, we see that, in the left panels, the local anthropogenic NO_X and natural NO_X contributions peak in the summertime, along with methane and natural VOC contributions in the right panels. The foreign NO_X and stratospheric contributions peak in the springtime. In all sub-regions, the springtime peak is composed of a peaking contribution from foreign NO_X and stratosphere along with an increasing local NO_X contribution. Methane remains the highest contributor throughout the year in terms of VOC contributions for all sub-regions. The lack of a summer peak for Western Europe is explained by lower local NO_X contributions as compared to other regions. For all regions, the wintertime MDA8 O_3 levels are sustained by high foreign NO_X contributions, mostly greater than 10 ppb. Ship NO_X contribution remains low, but can reach up to 5 ppb in spring and summer. Foreign AVOC contributions remain low, below 10 ppb, much lower than the~~

~~foreign NO_X contributions, pointing to their low interaction and potentially a higher interaction of foreign NO_X with natural VOC and methane globally.~~ ¶

The 19-year (2000-2018) average seasonal cycle of MDA8 O3 across European sub-regions was characterized using Fourier analysis, with parameters detailed in Tables S7-S10 and the cycles, along with source contributions, depicted in Figure 14. Observed annual mean MDA8 O3 (y0) across Europe is generally lower than in many North American regions, ranging from ~35 ppb in Western Europe to ~41 ppb in Southern Europe (Tables S7-S10). The model reproduces these annual means reasonably well for Western Europe (observed 35.36 ppb, modeled 34.67 ppb) and Southern Europe (observed 41.15 ppb, modeled 42.39 ppb). However, it underestimates y0 by ~1.5 ppb in C&E Europe (observed 38.1 ppb, modeled 36.62 ppb) and significantly overestimates it by ~7.5 ppb in SE Europe (observed 39.86 ppb, modeled 47.35 ppb). This large positive bias in y0 for SE Europe, also evident in the full seasonal cycle (Figure 14g,h), may be influenced by uncertainties due to limited observational network affecting the gridded observational product in this sub-region (see Figure S11).

The amplitude of the fundamental harmonic (A1), indicating the magnitude of seasonal variation, is substantial across Europe. Observed A1 ranges from 8.61 ppb in Western Europe to 11.62 ppb in Southern Europe. The model consistently overestimates A1 in all European regions, suggesting an overestimation of the summer photochemical peak. This overestimation is most pronounced in C&E Europe (modeled 15.18 ppb vs. observed 11.33 ppb) and Western Europe (modeled 11.13 ppb vs. observed 8.61 ppb). This pattern of overestimated A1 mirrors the findings for eastern North America and points towards a common model tendency to exaggerate summertime ozone production, likely linked to the modeled response of local and natural NOx/VOC contributions during summer months (Figure 14, left and right panels respectively).

The phase of the annual peak (φ_1) is relatively consistent across the regions, with observed values around 5.05-5.39 radians, indicating a late spring to early summer maximum. SE Europe exhibits a slightly later observed peak (φ_1 = 5.55 radians). The model generally captures this timing well, with modeled φ_1 values closely matching observations (e.g., Western Europe: obs. 5.05, mod. 5.2; Southern Europe: obs. 5.39, mod. 5.45). This agreement suggests the model correctly simulates the relative seasonal contributions of different processes driving the main ozone peak. For instance, the spring peak in Western Europe (Figure 14a) is notably influenced by foreign NOx and stratospheric contributions, while the broader spring-summer peak in Southern Europe and C&E Europe (Figure 14c) reflects a strong summertime peak in local and natural NOx contributions, alongside springtime transport influences.

The amplitude of the second harmonic (A2), representing semi-annual features, is generally smaller than A1 but non-negligible, with observed values between 1.76 ppb (C&E Europe) and 2.76 ppb (SE Europe). The model tends to reproduce A2 reasonably well for Western Europe and C&E Europe but overestimates it in Southern Europe (observed 1.79

ppb vs modeled 2.65 ppb). A significant A2 can reflect the interplay between springtime transport-driven ozone enhancements and summer photochemical production. The phase of this second harmonic (φ_2) shows more variability and model-observation agreement is mixed.

The Fourier parameters are consistent with the source attribution patterns: for Western Europe (Fig 14a,b), the distinct spring peak (captured by φ_1) is clearly driven by peaks in foreign NOx and stratospheric contributions. The model's overestimation of A1 stems from a more pronounced modeled summertime contribution from local and natural NOx than is suggested by the overall observed seasonal shape, which lacks a strong summer maximum. Methane is the dominant VOC contributor year-round. Southern and C&E Europe (Fig 14c-f) exhibit a broader spring-to-summer high. Their larger A1 values reflect a strong summer peak in local anthropogenic NOx and natural NOx contributions, which the model captures but tends to exaggerate, leading to the overestimation of A1. Foreign NOx contributes significantly to the spring shoulder and winter baseline. Methane and natural VOCs are key VOC contributors, especially during the warmer months. SE Europe (Fig 14g,h) shows a clear summer maximum in observations and model (larger φ_1; delayed peak). Local and natural NOx contributions drive the strong summer peak in the model.

The model effectively simulates the timing of the annual ozone peak (φ_1) across Europe. However, it consistently overestimates the amplitude of this annual cycle (A1), pointing to an overactive summer photochemistry in the model, a characteristic also noted for parts of North America. The annual mean ozone (y0) is well-reproduced for Western and Southern Europe but shows biases for Central & Eastern and particularly SE Europe. Wintertime ozone levels in all regions are sustained by significant foreign NOx contributions (often >10 ppb), while summertime peaks are primarily driven by local anthropogenic and natural NOx chemistry. Foreign AVOC contributions remain low (<5-7 ppb), suggesting limited interaction with European NOx, implying that transported NOx more significantly interacts with natural VOCs and globally present methane.

3.3.3 Changes in seasonal cycle of ozone in Europe: Role of Local vs Remote contributions

~~A long-term average of the ozone seasonal cycle as shown in the previous section provides us with a general sense of monthly contributions from various sources but it may conceal the (possibly large) year-to-year variations within the cycle. Therefore, in this section we compare the early 5-year average seasonal cycle with the recent 5-year seasonal cycle to understand the changing shape of the cycle and its contributing factors in terms of NO_X and VOC sources. Figure 11 presents the observed and modelled 5-year averaged MDA8 O_3 seasonal cycles for the initial (2000-2004) and final (2014-2018) periods along with their NO_X and VOC contributions for Western Europe. The model captures both the spring and summer peaks and their changes in this region extremely well. Between these initial and final periods, we see a significant drop in the summer peak (from 44 ppb to 40 ppb) along with an increase in the wintertime ozone levels. The summertime drop is due to~~

~~a drop in local NO_X contributions while the wintertime increase is due to an increase in foreign NO_X contributions (Figs 11b and c). It is noteworthy that the summertime drop in the local NO_X contributions is larger than the overall drop in summertime PSO. For example, for the month of August, the observed PSO dropped by 3.86 ppb between the two periods. This drop is 4.63 ppb in the model. However, the drop in the local NO_X contributions is larger (7.06 ppb) and there is also a drop in foreign NO_X contribution (0.25 ppb). These combined decreases in local and foreign NO_X contributions (7.31 ppb) are offset by increases in contributions from shipping NO_X (1.65 ppb), natural NO_X (0.96 ppb) and stratosphere (0.06 ppb) such that the overall drop in PSO in August is smaller. While the increase in shipping NO_X contribution is consistent with an increase in the northern hemispheric shipping NO_X emissions (Figure 2e), there is no significant increase in natural NO_X between the two periods, which shows the increasing ozone producing efficiency of natural NO_X when overall NO_X emissions are decreasing. In terms of VOCs, the summertime drop is associated with a drop in local AVOC contributions and the wintertime increase is primarily due to increased share of methane contribution as well as some foreign AVOC contribution. ¶~~

~~¶~~

~~Figure 12 presents the changes in the MDA8 O_3 seasonal cycle for Southern Europe. The model reproduces the seasonal cycles for both the initial and final periods extremely well. We broadly see a flattening of the ozone seasonal cycle in this region between the two periods, with the summertime peak coming down (due to reduced local NO_X contribution partially offset by increases in natural and ship NO_X contributions) and wintertime levels rising due to increase in wintertime foreign NO_X contributions, same as in Western Europe. From a VOC perspective, the summertime drop is associated with a decrease in local AVOC contributions and a small drop in methane contributions. The wintertime increase is associated with an increase in methane and foreign AVOC contributions but also stratospheric intrusion.¶~~

To understand the evolution of ozone seasonality in Europe, we compare the 5-year average MDA8 O3 seasonal cycles from an initial period (2000-2004) with a recent period (2014-2018). Here, we present the results for Western Europe and Southern Europe, with detailed Fourier parameters in Tables S7 and S8, and the corresponding seasonal cycles and source contributions in Figures 15 and 16. Results for the remaining European sub-regions are included in the supplement (Figures S9-S10; Tables S8-S9).

In Western Europe (Figure 15, Table S6), the most notable change between 2000-2004 and 2014-2018 is a distinct flattening of the summer ozone peak alongside an increase in wintertime ozone levels. The observed annual mean MDA8 O_3 (y0) remained remarkably stable (35.84 ppb to 35.85 ppb), a feature well-captured by the model (34.07 ppb to 35.28 ppb). However, the amplitude of the primary annual cycle (A1), representing the summer-winter difference, decreased in both observations (from 10.08 ppb to 7.95 ppb) and the model (from 13.16 ppb to 9.46 ppb). This indicates a significant damping of the seasonal swing. The phase of the fundamental harmonic (φ_1) shifted slightly earlier in observations (5.18 to 5.09 radians), as well as the model (5.32 to 5.18 radians).

These changes are primarily driven by shifts in NOx contributions (Figure 15b vs. 15e). The summertime contribution from local anthropogenic NOx decreased substantially between the two periods. This reduction in local summer production is the main cause of the lower summer peak and reduced A1. Conversely, wintertime ozone levels increased. This rise is linked to an increase in the foreign anthropogenic NOx contribution during winter and spring months in the later period, coupled with reduced titration from lower local NOx emissions (see section 3.4 where these two effects are disentangled). It is noteworthy that the reduction in the local NOx contribution during summer is larger than the overall decrease in total MDA8 O3 during these months, because offsetting increases from other sources like shipping NOx (which increased from ~2 ppb to ~4 ppb in August) and a more efficient ozone production from remaining natural NOx under lower overall NOx conditions partly compensated for the local reductions. As noted previously, while Northern Hemispheric shipping NOx emissions increased (Figure 2e), the increased contribution from natural NOx highlights its enhanced ozone-forming efficiency in a lower-NOx environment. From a VOC perspective (Figure 15c vs. 15f), the summertime decrease is associated with a reduction in local AVOC contributions. The wintertime ozone increase is supported by a larger share of methane contribution and, to a lesser extent, foreign AVOCs during winter in the recent period.

Southern Europe (Figure 16, Table S7) also exhibits a notable evolution in its seasonal ozone cycle, characterized by a flattening of the seasonal cycle. The observed annual mean ozone (y0) slightly increased (from 40.83 ppb to 41.81 ppb), a trend also seen in the model (42.05 ppb to 42.76 ppb). The amplitude of the fundamental harmonic (A1) decreased significantly in observations (from 13.02 ppb to 10.64 ppb) and even more so in the model (from 15.18 ppb to 9.93 ppb), indicating a substantial reduction in the peak summer concentrations. The phase of the peak (φ_1) remained relatively stable, suggesting the timing of the summer maximum did not shift considerably.

The primary driver for the reduced summer peak and lower A1 is the marked decrease in the summertime contribution from local anthropogenic NOx (Figure 16b vs. 16e). While this local source remains the dominant contributor to the summer peak, its magnitude is considerably lower in 2014-2018 compared to 2000-2004. Similar to Western Europe, contributions from foreign anthropogenic NOx have become relatively more important throughout the year, particularly sustaining spring and winter ozone levels. Natural NOx and shipping NOx contributions also show slight increases in summer in the later period, partially offsetting the local NOx reductions.

Regarding VOC contributions (Figure 16c vs. 16f), the summertime decrease in ozone is linked to reductions in both local AVOC and methane contributions during the peak season in the later period. Methane remains the largest VOC contributor overall, but its peak summer contribution has diminished. Wintertime ozone increases are associated with higher contributions from methane and foreign AVOCs, along with stratospheric intrusion.

3.4 Increasing Foreign Ozone in North America and Europe: increasing Foreign NOx emissions versus reduced local titration of background ozone:

Previous sections highlighted an increasing trend in the contribution of foreign anthropogenic NOx to ozone in various North American and European receptor regions, particularly during winter and spring (Jan-Apr). This observed increase in ozone attributed to foreign anthropogenic NOx (hereafter, O3_FOREIGN) could stem from two primary mechanisms: (i) an actual increase in the intercontinental transport of ozone produced from foreign NOx emissions, or (ii) an "unmasking" of existing transported ozone due to weakened local titration ($NO + O_3 \rightarrow NO_2 + O_2$) as local NO emissions have declined in these regions. Disentangling these factors is crucial for making informed decisions on local as well as global emission reduction policies. For example, if the second mechanism is dominant, it would imply that with further local NOx reductions we should expect more increases in winter-springtime ozone (which may potentially be a barrier to such policymaking). However, if the first mechanism is dominant, then further decreases in local NOx will principally decrease local ozone while the transported component can be controlled through international policies.

To investigate this, we analyzed the combined contribution of O_3_FOREIGN and the NO_2 formed from the titration of O_3_FOREIGN (hereafter, NO_2_FOREIGN). It is noteworthy that this NO2_FOREIGN, locally recovered from foreign ozone titration, is separately tagged in our modelling system than the NO2 directly flowing from foreign regions (which we do not discuss here). The sum, Ox_FOREIGN (O3_FOREIGN + NO2_FOREIGN), represents the total reactive odd oxygen attributable to foreign anthropogenic NOx sources. An increasing trend in Ox_FOREIGN would more strongly indicate an actual rise in transported reactive oxygen from foreign sources, whereas an increase in O_3_FOREIGN with relatively stable Ox_FOREIGN might suggest a dominant role of reduced local titration.

Figure 17 presents the time series of winter-spring (Jan-Apr) mean O_3_FOREIGN (blue shaded area) and the additional NO_2_FOREIGN component (grey shaded area, making up the total Ox_FOREIGN indicated by the top of the grey area) for selected North American and European receptor regions over the 2000-2018 period. In both the NW US (Figure 17a) and SW US (Figure 17b), a clear increasing trend is evident not only in O_3_FOREIGN but also in the total Ox_FOREIGN over the 2000-2018 period. For instance, in NW US, Jan-Apr mean O_3_FOREIGN increased from approximately 10.3 ppb in 2000 to 13.3 ppb in 2018, while Ox_FOREIGN increased from approximately 10.8 ppb to 13.6 ppb. Similarly, in SW US, O_3_FOREIGN rose from around 10.6 ppb to 13.7 ppb, and Ox_FOREIGN from 11.2 ppb to 14.0 ppb. The NO2_FOREIGN component (grey area) is consistently small, typically ranging from 0.2 to 0.7 ppb during these cold, low-photolysis months. The key finding here is that the total Ox_FOREIGN shows a clear increasing trend. This robust increase in Ox_FOREIGN demonstrates that the rising influence of foreign NOx on winter-spring ozone in western North America is substantially driven by an actual increase in the import of reactive odd oxygen from foreign sources, rather than solely by reduced local titration unmasking more foreign-produced background ozone. While reduced local titration plays a minor role (NO2_FOREIGN decreases over time), the fundamental increase in O3_FOREIGN is due to increasing foreign NOx

emissions. The Ox_FOREIGN peaks in 2013 when Northern Hemispheric NOx emissions also peaked (see Figure 2e). These results are consistent with findings of Elshorbany et al., (2024) and Lu et al., (2024) who report increasing ozone trends in Asia both in the troposphere and at the surface which stabilize around 2013. After 2013, we see a decline in both Ox_FOREIGN and O3_FOREIGN which is principally driven by a decline in foreign NOx emissions (Crippa et al., 2023), which is primarily due to the implementation of China's Clean Air Programme (Zheng et al., 2018)

Similar patterns are observed in Western Europe and Southern Europe (Figures 17c and d, respectively). In Western Europe, winter-spring O3_FOREIGN increased from 10.6 ppb in 2000 to 11.6 ppb in 2018, with Ox_FOREIGN rising from 11.9 ppb to 12.6 ppb. Southern Europe saw O3_FOREIGN increase from around 10.7 ppb to 12.9 ppb, and Ox_FOREIGN from 11.8 ppb to 13.4 ppb. Again, the NO_2_FOREIGN component remains a minor fraction of the total Ox_FOREIGN during these Jan-Apr periods and slightly decreases with time, reflecting reduced titration of O3_FOREIGN. The consistent increase in the total Ox_FOREIGN across these European regions, much like in North America, demonstrates an increasing influx of reactive odd oxygen attributed to foreign NOx sources. This suggests that the observed rise in foreign ozone contributions during European winter-spring is not merely an artifact of changing local chemical environments (i.e., reduced titration) but reflects a more fundamental increase in the amount of pollution arriving from upwind, foreign sources.

4. Conclusion, Limitations and Future Outlook:

In this study we explain the long-term trends and the evolving shape of~~changes in~~ the seasonal cycle of surface ozone in ~~Europe and~~ North America and Europe (an issue raised by many previous observational studies) in terms of changing contributions from various NOx and VOC sources, through the use of an ozone tagging system in a global chemical transport model. ~~for the period 2000-2018.~~ While both regions have experienced rapid reductions in locally-emitted ozone precursors in recent decades, we note that the Peak Season Ozone (PSO) in both regions exceeds the WHO guidelines for the entire study period.

Our model is generally in good agreement with ground observations from rural stations in the newly-developed TOAR-II database, allowing us to attribute the observed trends in terms of the changing contributions from local and foreign emission sources of NO_X and VOC. While A~~anthropogenic NM~~VOC emissions contribute a relatively small fraction of the total PSO, anthropogenic NO_X emissions have a much stronger influence. The decreasing trend in NO_X emissions in both North America and Europe leads to a lower fraction of the PSO attributable to these local NO_X emissions towards the recent years, however the total modelled decrease in PSO in both regions is partially offset by increasing contributions from natural NO_X, foreign anthropogenic NO_X, and international shipping.

While the increasing trend in ozone attributable to international shipping (despite potential overestimation of ozone produced from ships) is consistent with increasing emissions from this sector, the increasing trend in modelled contribution of natural NO_X emissions~~ we find in our study~~, especially during the summertime, suggests~~ is most likely due to the~~ increasing ozone productivity of these emissions since there is no ~~noticeable~~ increasing trend in natural NOx emissions in our model and a slight decreasing trend in Lightning NOx emissions (Figure 3 a, c, e, g)~~.~~. The decreases in local NO_X emissions in both regions lead to strong reductions in summertime ozone, but have a smaller effect in the springtime, when long-range transport of ozone produced from foreign anthropogenic NO_X emissions and stratosphere is more important (Table 3). All regions show a modest increasing trend in the foreign anthropogenic NO_X contribution to the PSO~~peak season ozone~~ over the study period. Especially in the western sub-regions of Europe and North America, the foreign anthropogenic NO_X contribution to PSO has become comparable in magnitude to the local NO_X contribution. Foreign anthropogenic NOx contribution to winter-springtime ozone has increased significantly and is primarily driven by increases in foreign NOx emissions rather than reduced titration of foreign transported ozone, although the latter also plays a minor role. We have shown that local anthropogenic NOX emissions still contribute significantly to PSO in both Europe and North America and its further reduction would not unmask a large amount of previously titrated ozone over regional scales in winter and spring. As an emission source which can be controlled with domestic policy interventions, future policy should continue to target these emissions.

¶

Due to the nature of our ozone tagging system, we perform two separate source attributions, one for NO_X emissions, and another for VOC emissions. When attributing ozone to VOC emissions, we note the strong contribution of BVOC emissions to the summertime peak ozone, which is clearly linked with the strong contribution of local anthropogenic NO_X emissions to summertime ozone. The co-variability of these two sources is also apparent in the PSO time series for all regions and emphasizes the interaction of anthropogenic NOx with BVOC in rural and background regions. This is an emerging finding made possible due to our dual-tagging approach; a relatively recent regional modelling study (Lupascu et al., 2022) focusing on two high ozone episodes in Germany that also utilized the TOAST1.0 system also noted the interaction of local anthropogenic NOx and BVOC in driving ozone peaks.~~and emphasizes the interaction of anthropogenic NOx with BVOC in rural and background regions.~~ This finding highlights that, at least for rural and background regions, the interaction of anthropogenic NOx with BVOC exceeds its interaction with AVOC which might be contained within the urban centres. It is noteworthy that BVOC emissions also either match or exceed AVOC emissions in North America and Europe during the peak season. In all of the sub-regions in our study except for the eastern parts of the United States, the contribution of methane to ozone is greater than that of BVOC. While global methane concentrations have risen from 1787 ppb to 1875 ppb during our study period (an increase of about 5%), this has only led to a modest increasing trend in methane contributions to PSO in Europe. In all regions of the US except NW US, the methane contribution to PSO has slightly decreased over this time. This is consistent with the large reductions in local NO_X emissions, leading to a lower efficiency of ozone production

during methane oxidation over both regions. ~~Given the strong role of methane as an ozone precursor, as noted in this study and consistent with previous work, targeted reductions of methane along with other AVOC can also be expected to contribute to the reductions in PSO needed to comply with the WHO guideline value~~.

The TOAST1.0 dual-tagging technique uniquely allows us to unveil many interesting results summarized above, which would not be possible to disentangle through perturbative approaches or other tagging approaches that tag a specific region with all its (NOx+VOC) emissions or the geographic area of ozone production. It provides us with a parallel view of the composition of ozone trends in terms of NOx and VOC precursors belonging to their original source locations, thereby facilitating a more targeted species-specific policy response. Many key results, for example: the separation of Foreign NOx versus stratospheric contributions in explaining springtime ozone increase; separation of increased wintertime ozone to increased foreign NOx versus reduced local titration; decreasing methane contribution to ozone in many regions despite increasing background methane; and in general the co-attribution of ozone to anthropogenic and biogenic emission sources under baseline conditions, would not be unveiled without the aid of our novel tagging system. Our innovative approach to model evaluation by breaking down the observed and modelled ozone seasonal cycles into a fundamental and secondary harmonic using Fourier transform and then comparing them against the seasonal cycles of tags (e.g., comparison of the fundamental harmonic against the local NOx contribution to seasonal cycle) allows us to test the validity of such statistical decomposition techniques in different contexts and improve their theoretical interpretation; something which could not be achieved without tagged model simulations. Once sufficiently validated, such statistical decomposition could be applied more broadly, thereby unveiling new scientific insights from observations alone.¶

While this study has yielded an array of novel scientific results and policy-relevant insights, a number of limitations remain. First, our model spatial resolution ($1.9^{o}\times2.5^{o}$), necessitated by the extra computational burden of tagged species and the long duration of the simulation period, is admittedly quite coarse and potentially introduces model biases. A recent study by Gao et al. (2025) has highlighted that the long-standing problem of overestimating surface ozone in the northern hemispheric mid-latitudes by global models can be addressed in large part by increasing the model resolution. Therefore, future modelling studies with tagging can be performed over short duration but high model resolution to assess the effect of model resolution on model bias and source contributions. Second, ~~While~~ our ~~ozone~~ source attribution, while ~~is~~ capable of determining the contributions of different local and remote emission sources to the ozone under baseline conditions~~as simulated in our model, it~~ is only of limited usefulness in predicting the response of ozone levels to any future emission reductions. For such an assessment, it is necessary to perform model sensitivity studies reflecting the actual policy interventions aimed at reducing ozone. Studies like ours can however identify the major contributing emission sources. Given the strong role of methane as an ozone precursor, targeted reductions of methane along with other AVOC can also be expected to contribute to the reductions in PSO needed to comply with the WHO guideline value but such an assessment

would require model perturbation studies wherein methane and AVOCs are reduced. Third, our approach does not attribute any changes in ozone to meteorological changes which might become increasingly important in a warming world. Instead, all changes in ozone are essentially attributed to precursor emissions. However, changing contributions from certain emission sources do not necessarily imply only changing emissions but could also be due to more/less efficient transport of foreign produced ozone due to meteorological changes.

~~We have shown here that local anthropogenic NO_x emissions still contribute significantly to PSO in both Europe and North America and its further reduction would not unmask a large amount of previously titrated ozone in winter and spring. As an emission source which can be controlled with policy interventions, future policy should continue to target these emissions. Given the strong role of methane as an ozone precursor, as noted in this study and consistent with previous work, targeted reductions of methane along with other Aanthropogenic NMVOC can also be expected to contribute to the reductions in PSO needed to comply with the WHO guideline value.¶~~

~~Increasing productivity of natural NOx under a lower NOx environment could be tested in future perturbation+tagging studies.¶~~

Author Contributions:

TA and TB together designed the study. TA performed the model simulations, performed all the analyses and produced the visualizations with inputs from TB. AN and AL provided support in model setup, source code changes for incorporating new tags, and generating the tagged chemical mechanisms for NOx and VOC attribution. CH and SG created and provided the gridded TOAR dataset for model evaluation. TA wrote the manuscript with inputs from TB. All co-authors provided their inputs to the discussion and the final manuscript.

Acknowledgements:

This work utilized high-performance computing resources made possible by funding from the Ministry of Science, Research and Culture of the State of Brandenburg (MWFK) and are operated by the IT Services and Operations unit of the Helmholtz Centre Potsdam. TA would like to thank Dr. Edward Chan at RIFS for his technical assistance in setting-up the model on the GFZ GLIC supercluster.

The following programs, organizations and persons contributed to the TOAR gridded dataset: **programmes:** Global Atmospheric Watch Program; Research and Development Programme of Ministry of Education Culture Sports Science and Technology Japan and Environmental Research and Technology Development Fund of Ministry of Environment Japan;

organizations: AECOM; Aethon Energy; Air Quality Services; Air Resource Specialists, Inc; Akron Regional Air Pollution Control Agency; Al Dept Of Env Mgt; Albuquerque Environmental Health Department, Air Quality Division; Anadarko, WY; Arizona Department Of Environmental Quality; Arkansas Department of Energy and Environment; Bay Area Air Quality Management District; Bayerisches Landesamt für Umwelt; Boulder City-County Health Department; CH2M Hill; Cabazon Band of Mission Indians, CA; California Air Resources Board; Canton City Health Department Air Pollution Control; Chattanooga-Hamilton County Air Pollution Control; Cherokee Nation, Oklahoma; Cherokee Nation/ITEC (consortium); Choctaw Nation of Oklahoma; City of Huntsville, Div of Natural Resources; City of Jacksonville Environmental Quality Division; City of Toledo, Environmental Services Division; Clark County, NV DAQEM; Colorado Department of Public Health And Environment; Confederated Tribes of Umatilla Reservation of Oregon; Connecticut Department of Environmental Protection; Dames & Moore, Inc; Dayton Regional Air Pollution Control Agency; Delaware Dept Natural Resources and Environmental Control; Delaware Nation, OK; EBAS; Eastern Band Of Cherokee Indians of North Carolina; Eastern Shoshone and Northern Arapaho Tribes of Wyoming; Enefit; Environment and Climate Change Canada / Government of Canada; Environmental Monitoring Company (Emc); European Environment Agency; Evansville Division Of Air Pollution Control; FDEP Ambient Monitoring Section; Florida Department of Environmental Protection (FDEP); Florida Dept of Environmental Protection, Central District; Florida Dept of Environmental Protection, Northeast District; Florida Dept of Environmental Protection, Northwest District; Florida Dept of Environmental Protection, South District; Florida Dept of Environmental Protection, Southeast District; Florida Dept of Environmental Protection, Southwest District; Forest County Potawatomi Community, WI; Forsyth County Environmental Affairs Department; Georgia Air Protection Branch Ambient Monitoring Program; Gila River Indian Community of Gila River Indian Reservation, AZ; Goodyear Tire Obion County, TN; Great Basin Unified APCD; Hamilton County Department Of Environmental Services; Hessisches Landesamt für Umwelt und Geologie; Hillsborough County Environmental Protection Commission; Idaho Department Of Health And Welfare-Environment Division; Illinois Environmental Protection Agency; Imperial County APCD; Indiana Depart Of Environ Management/Office Of Air Quality; Indianapolis Office of Environmental Services; Institut für Hygiene und Umwelt Hamburg; Inter-tribal Council of MIchigan, Inc.; Japan Agency for Marine-Earth Science and Technology; Jefferson County, AL Department Of Health; Kansas City Health Department, Air Quality Section; Kansas Department Of Health And Environment; Kentucky Division For Air Quality; KNO_X County Department Of Air Pollution Control; La Posta Band of Dieguento Mission Indians of La Posta Indian Reservation, CA; Lake County Health Department Division Air Pollution Control; Landesamt für Natur, Umwelt und Verbraucherschutz Nordrhein-Westfalen; Landesamt für Umwelt, Naturschutz und Geologie; Landesamt für Umwelt, Wasserwirtschaft und Gewerbeaufsicht; Landesamt für Umweltschutz Sachsen-Anhalt; Landesanstalt für Umwelt, Messungen und Naturschutz Baden-Württemberg; Lane Regional Air Pollution Authority; Las Vegas Tribe of Paiute Indians of the Las Vegas Indian Colony, NV; Lincoln-Lancaster County Health Department; MT Dept Of Environmental Quality, Air Quality Division; Mactec, Inc; Mahoning-Trumbull Air Pollution Control Agency; Maine D.E.P. Bureau Of Air Quality Control, Augusta; Manatee County Environmental Management Department; Maricopa County Air Quality ; Maryland Department of the Environment; Mass Dept

Environmental Protection-Div Air Quality Control; Mecklenburg County Air Quality; Memphis-Shelby County Health Department; Meteorological Solutions, Inc.; Metropolitan Health Department/Nashville & Davidson County; Miami-Dade County Department of Environmental Resources Management ; Michigan Dept Of Environment, Great Lakes, and Energy-Air Quality Division; Ministerium für Energiewende, Landwirtschaft, Umwelt und ländliche Räume; Ministerium für Umwelt und Verbraucherschutz Saarland; Minnesota Chippewa Tribe, MN (Fond du Lac Band); Minnesota Pollution Control Agency, Division Of Air Quality; Mississippi DEQ, Office Of Pollution; Missouri Laboratory Services Program; Mojave Desert AQMD; Monterey Bay Unified APCD; Morongo Band of Mission Indians, CA; National Institute for Environmental Studies; National Park Service; Navajo Nation, AZ, NM, UT; Nevada Division Of Environmental Protection; New Hampshire Air Resources Agency; New Jersey State Department Of Environmental Protection; New Mexico Environment Department; New York State Department Of Environmental Conservation; Niedersächsiches Ministerium für Umwelt, Energie und Klimaschutz; North Carolina Dept Of Environmental Quality; North Coast Unified Air Quality Management District; North Dakota DEQ; Northern Sonoma County APCD; Northwestern Band of Shoshoni Nation of Utah (Washakie); Ohio EPA Central Office; Ohio EPA, Central District Office; Ohio EPA, Northeast District Office; Ohio EPA, Northwest District Office; Ohio University, Athens, OH; Oklahoma Dept. Of Environmental Quality Air Quality Division; Olympic Air Pollution Control Authority; Omaha-Douglas County Health Department; Open Air Quality; Oregon Department Of Environmental Quality; Paiute-Shoshone Indians of Bishop Community of Bishop Colony, CA; Pala Band of Luiseno Mission Indians of Pala Reservation, CA; Passamaquoddy Tribe of Maine (Pleasant Point); Pennsylvania Department Of Environmental Protection; Pennsylvania State University (Penn State); Penobscot Tribe of Maine; Picayune Rancheria of Chukchansi Indians of California; Pima County Department of Environmental Quality; Pinal County APCD; Pinellas County Department Of Environmental Management; Polk County Physical Planning; Ponca Tribe of Indians of Oklahoma; Portsmouth City Health Dept Division Air Pollution Control; Pueblo of Jemez, NM; Quapaw Tribe of Indians, OK; Quebecor; RR Donnley, IN; Sac and Fox Nation, OK; Sacramento County APCD; Salt River Pima-Maricopa Indian Community of Salt River Reservation, AZ; San Diego County Air Pollution Control District; San Joaquin Valley Unified Air Pollution Control District; San Luis Obispo County APCD; Santa Barbara County APCD; Santa Rosa Indian Community of Santa Rosa Rancheria, CA; Senat für Umwelt, Bau und Verkehr, Bremen; Senatsverwaltung für Stadtentwicklung und Umwelt; Senatsverwaltung für Umwelt, Verkehr und Klimaschutz Berlin; Servicio Meteorologico Nacional; Shasta County APCD; South Carolina Department Health And Environmental Control; South Coast Air Quality Management District; South Dakota Department of Agriculture and Natural Resources; South East Texas Regional Planning Commission (SETRPC); Southern Ute Indian Tribe of Southern Ute Reservation, CO; St Louis County Health Department Air Pollution Control; St. Regis Mohawk Tribe, New York; State Of Louisiana; Swinomish Indians of Swinomish Reservation, WA; Sächsisches Landesamt für Umwelt, Landwirtschaft und Geologie; Table Mountain Rancheria; Taiwan Environmental Protection Agency; Tallgrass Energy Partners; Tata Chemicals; Tennessee Division Of Air Pollution Control; Tennessee Valley Authority; Texas Commission On Environmental Quality; Thüringer Landesanstalt für Umwelt und Geologie; Torres-Martinez Cahuilla Indians, California; Toyota; Tracer Technologies; US Forest Service; USEPA - Clean Air Markets

Division; Umweltbundesamt; United States Environmental Protection Agency; University Hygenic Laboratory (University of Iowa); Utah Department Of Environmental Quality; Ute Indian Tribe of Uintah & Ouray Reservation, UT; Vandenberg AFB; Ventura County APCD; Vermont Agency Of Environmental Conservation; Vigo County Division Of Air Pollution Control; Virginia Department of Environmental Quality; WAUPACA Foundry; Wampanoag Tribe of Gay Head (Aquinnah) of Massachusetts; Warren Energy Services, LLC; Washington State Department Of Ecology; West Virginia Division of Air Quality; Weston Solutions, TX; Wisconsin Dept Of Natural Resources, Air Monitoring Section; Wyoming Air Quality Division, Dept Of Environmental Quality; Wyoming Bureau of Land Management; **persons**: Maria; Adela Holubova; Anne-Cathrine Nilsen; Aude Bourin; Christine F Braban; Christoph Hueglin; Christopher Conolly; Chrysanthos Savvides; Erik Andresen; Erzsebet Gyarmatine Meszaros; Gabriela Vitkova; Gerardo Carbajal Benitez; Gerardo Carbajal Benítez; Hiroshi Tanimoto; Indriksone Iveta; Iveta Indriksone; Jan Silhavy; Jaroslav Pekarek; Jasmina Knezevic; Juan Martinez; Karin Sjoberg; Karin Sjöberg; Karin Sjøberg; Keith Vincent; Lino Fabian Condori; Magdalena Bogucka; Maj-Britt Larka; Marcin Syrzycki; Maria Barlasina; Marijana Murovec; Mateja Gjere; Milan Vana; Ming-Tung Chuang; Monistrol Jose Antonio Fernandez; Muinasmaa Urmas; Murovec Marijana; Nikolova Yana; Robert Gehrig; Roman Prokes; Rune Keller; Stefan Reimann; Truuts Toivo; Ursul Gina; Usin Eve; Veronika Minarikova; Wenche Aas; Willis Paul; Yugo Kanaya; Zdzislaw Przadka (2024). Ozone data obtained from TOAR Database for rural stations between 2000 and 2018.

Competing Interests

TB is a member of the editorial board of Atmospheric Chemistry and Physics.

Data Availability

Please contact tabish.ansari@rifs-potsdam.de for availing the model output of our simulations.

References:

Ansari, T. U., Wild, O., Li, J., Yang, T., Xu, W., Sun, Y., and Wang, Z.: Effectiveness of short-term air quality emission controls: a high-resolution model study of Beijing during the Asia-Pacific Economic Cooperation (APEC) summit period, Atmos. Chem. Phys., 19, 8651–8668, https://doi.org/10.5194/acp-19-8651-2019, 2019.

Ansari, T. U., Wild, O., Ryan, E., Chen, Y., Li, J., and Wang, Z.: Temporally resolved sectoral and regional contributions to air pollution in Beijing: informing short-term emission controls, Atmos. Chem. Phys., 21, 4471–4485, https://doi.org/10.5194/acp-21-4471-2021, 2021.

Ashmore, M. R.: Assessing the future global impacts of ozone on vegetation, Plant Cell & Environment, 28, 949–964, https://doi.org/10.1111/j.1365-3040.2005.01341.x, 2005.

Atkinson, R.: Gas-phase tropospheric chemistry of organic compounds: A review, Atmos. Environ. Part A. Gen. Top., 24, 1–41, https://doi.org/10.1016/0960-1686(90)90438-S, 1990.

Atkinson, R.: Gas-phase tropospheric chemistry of organic compounds, J. Phys. Chem. Ref. Data, Monograph 2, 1–216, 1994.

Atkinson, R.: Gas-phase tropospheric chemistry of volatile organic compounds: 1. Alkanes and alkenes, J. Phys. Chem. Ref. Data, 26, 215–290, https://doi.org/10.1063/1.556012, 1997.

Avnery, S., Mauzerall, D. L., Liu, J., and Horowitz, L. W.: Global crop yield reductions due to surface ozone exposure: 1. Year 2000 crop production losses and economic damage, Atmospheric Environment, 45, 2284–2296, https://doi.org/10.1016/j.atmosenv.2010.11.045, 2011.

Beaton, S. P., Bishop, G. A., Zhang, Y., Stedman, D. H., Ashbaugh, L. L., and Lawson, D. R.: On-Road Vehicle Emissions: Regulations, Costs, and Benefits, Science, 268, 991–993, https://doi.org/10.1126/science.268.5213.991, 1995.

Becker, J. S., Butler, T., Nalam, A., Lupascu, A., and Kipling, Z.: Using Regionalized Air Quality Model Performance and Bayesian Maximum Entropy data fusion to map global surface ozone concentration, Elementa: Sci. Anth., 11, e2022.00025, https://doi.org/10.1525/elementa.2022.00025, 2023.

¶

Berntsen, T. K., Karlsdóttir, S., and Jaffe, D. A.: Influence of Asian emissions on the composition of air reaching the north western United States, Geophys. Res. Lett., 26, 2171–2174, https://doi.org/10.1029/1999GL900477, 1999.

Bowdalo, D. R., Evans, M. J., and Sofen, E. D.: Spectral analysis of atmospheric composition: application to surface ozone model–measurement comparisons, Atmos. Chem. Phys., 16, 8295–8308, https://doi.org/10.5194/acp-16-8295-2016, 2016.

Bloomer, B. J., Vinnikov, K. Y., and Dickerson, R. R.: Changes in seasonal and diurnal cycles of ozone and temperature in the eastern U.S., Atmospheric Environment, 44, 2543–2551, https://doi.org/10.1016/j.atmosenv.2010.04.031, 2010.

Bowman, H., Turnock, S., Bauer, S. E., Tsigaridis, K., Deushi, M., Oshima, N., O'Connor, F. M., Horowitz, L., Wu, T., Zhang, J., Kubistin, D., and Parrish, D. D.: Changes in anthropogenic precursor emissions drive shifts in the ozone seasonal cycle throughout the northern midlatitude troposphere, Atmos. Chem. Phys., 22, 3507–3524, https://doi.org/10.5194/acp-22-3507-2022, 2022.

Brook, R. D., Franklin, B., Cascio, W., Hong, Y., Howard, G., Lipsett, M., Luepker, R., Mittleman, M., Samet, J., Smith, S. C. Jr., and Tager, I.: Air pollution and cardiovascular disease: a statement for healthcare professionals from the Expert Panel on Population and Prevention Science of the American Heart Association, Circulation, 109, 2655–2671, https://doi.org/10.1161/01.CIR.0000128587.30041.C8, 2004.

Burr, M. J. and Zhang, Y.: Source apportionment of fine particulate matter over the Eastern U.S. Part II: source apportionment simulations using CAMx/PSAT and comparisons with CMAQ source sensitivity simulations, Atmospheric Pollution Research, 2, 318–336, https://doi.org/10.5094/APR.2011.037, 2011.

Butler, T., Lupascu, A., and Nalam, A.: Attribution of ground-level ozone to anthropogenic and natural sources of nitrogen oxides and reactive carbon in a global chemical transport model, Atmos. Chem. Phys., 20, 10707–10731, https://doi.org/10.5194/acp-20-10707-2020, 2020.

Butler, T., Lupascu, A., Coates, J., and Zhu, S.: TOAST 1.0: Tropospheric Ozone Attribution of Sources with Tagging for CESM 1.2.2, Geosci. Model Dev., 11, 2825–2840, https://doi.org/10.5194/gmd-11-2825-2018, 2018.

Butler, T., Lupascu, A., Coates, J., and Zhu, S.: TOAST 1.0: Tropospheric Ozone Attribution of Sources with Tagging for CESM 1.2.2, Geosci. Model Dev., 11, 2825–2840, https://doi.org/10.5194/gmd-11-2825-2018, 2018.

Calvert, J. G., Heywood, J. B., Sawyer, R. F., and Seinfeld, J. H.: Achieving Acceptable Air Quality: Some Reflections on Controlling Vehicle Emissions, Science, 261, 37–45, https://doi.org/10.1126/science.261.5117.37, 1993.

Carslaw, D. C.: On the changing seasonal cycles and trends of ozone at Mace Head, Ireland, Atmos. Chem. Phys., 5, 3441–3450, https://doi.org/10.5194/acp-5-3441-2005, 2005.

Chang, K.-L., Petropavlovskikh, I., Cooper, O. R., Schultz, M. G., and Wang, T.: Regional trend analysis of surface ozone observations from monitoring networks in eastern North America, Europe and East Asia, Elementa: Science of the Anthropocene, 5, 50, https://doi.org/10.1525/elementa.243, 2017.

Chang, K.-L., Cooper, O. R., Gaudel, A., Petropavlovskikh, I., Effertz, P., Morris, G., and McDonald, B. C.: Technical note: Challenges in detecting free tropospheric ozone trends in a sparsely sampled environment, Atmos. Chem. Phys., 24, 6197–6218, https://doi.org/10.5194/acp-24-6197-2024, 2024.

Cheesman, A. W., Brown, F., Artaxo, P., and others: Reduced productivity and carbon drawdown of tropical forests from ground-level ozone exposure, Nat. Geosci., 17, 1003–1007, https://doi.org/10.1038/s41561-024-01530-1, 2024.

Chen, G., Blake, D. R., Heikes, B., Huey, G., Lueb, R., Ryerson, T. B., Thornton, D., and Williams, E.: An investigation of the chemistry of ship emission plumes during ITCT 2002, J. Geophys. Res., 110, D10S90, https://doi.org/10.1029/2004JD005236, 2005.

Chen, T.-M., Kuschner, W. G., Gokhale, J., and Shofer, S.: Outdoor Air Pollution: Ozone Health Effects, The American Journal of the Medical Sciences, 333, 244–248, https://doi.org/10.1097/MAJ.0b013e31803b8e8c, 2007.

Christiansen, A., Mickley, L. J., Liu, J., Oman, L. D., and Hu, L.: Multidecadal increases in global tropospheric ozone derived from ozonesonde and surface site observations: can models reproduce ozone trends?, Atmos. Chem. Phys., 22, 14751–14782, https://doi.org/10.5194/acp-22-14751-2022, 2022.

Clean Air Act (1963). United States Congress. Clean Air Act of 1963. Public Law 88-206, 77 Stat. 392. Enacted December 17, 1963. Available at: U.S. EPA.

Clean Air Act Amendments (1990). United States Congress. Clean Air Act Amendments of 1990. Public Law 101-549, 104 Stat. 2399. Enacted November 15, 1990. Available at: U.S. EPA.

Clifton, O. E., Fiore, A. M., Correa, G., Horowitz, L. W., and Naik, V.: Twenty-first century reversal of the surface ozone seasonal cycle over the northeastern United States, Geophys. Res. Lett., 41, 7343–7350, https://doi.org/10.1002/2014GL061378, 2014.

Cooper, O. R., Gao, R., Tarasick, D., Leblanc, T., and Sweeney, C.: Long-term ozone trends at rural ozone monitoring sites across the United States, 1990–2010, J. Geophys. Res., 117, 2012JD018261, https://doi.org/10.1029/2012JD018261, 2012.

Cooper, O. R., Parrish, D. D., Stohl, A., Trainer, M., Nédélec, P., Thouret, V., Cammas, J. P., Oltmans, S. J., Johnson, B. J., Tarasick, D., Leblanc, T., McDermid, I. S., Jaffe, D., Gao, R., Stith, J., Ryerson, T., Aikin, K., Campos, T., Weinheimer, A., and Avery, M. A.: Increasing springtime ozone mixing ratios in the free troposphere over western North America, Nature, 463, 344–348, https://doi.org/10.1038/nature08708, 2010.

Cooper, O. R., Parrish, D. D., Ziemke, J., Balashov, N. V., Cupeiro, M., Galbally, I. E., Gilge, S., Horowitz, L., Jensen, N. R., Lamarque, J.-F., Naik, V., Oltmans, S. J., Schwab, J., Shindell, D. T., Thompson, A. M., Thouret, V., Wang, Y., and Zbinden, R. M.: Global distribution and trends of tropospheric ozone: An observation-based review, Elementa: Science of the Anthropocene, 2, 000029, https://doi.org/10.12952/journal.elementa.000029, 2014.

Cooper, O. R., Schultz, M. G., Schröder, S., Chang, K.-L., Gaudel, A., Benítez, G. C., Cuevas, E., Fröhlich, M., Galbally, I. E., Molloy, S., Kubistin, D., Lu, X., McClure-Begley, A., Nédélec, P., O'Brien, J., Oltmans, S. J., Petropavlovskikh, I., Ries, L., Senik, I., Sjöberg, K., Solberg, S., Spain, G. T., Spangl, W., Steinbacher, M., Tarasick, D., Thouret, V., and Xu, X.: Multi-decadal surface ozone trends at globally distributed remote locations, Elem Sci Anth, 8, 23, https://doi.org/10.1525/elementa.420, 2020.

Council Directive 96/62/EC (Framework Directive on Ambient Air Quality Assessment and Management) European Parliament and Council. Council Directive 96/62/EC on Ambient Air Quality Assessment and Management. Official Journal of the European Communities, L 296, 21 November 1996, pp. 55-63. Available at: EUR-Lex.

~~Crespo-Miguel, R., Ordóñez, C., García-Herrera, R., Schnell, J. L., and Turnock, S. T.: Large-scale ozone episodes in Europe: Decreasing sizes in the last decades but diverging changes in the future, Science of The Total Environment, 949, 175071, https://doi.org/10.1016/j.scitotenv.2024.175071, 2024.~~

Crippa, M., Guizzardi, D., Butler, T., Keating, T., Wu, R., Kaminski, J., Kuenen, J., Kurokawa, J., Chatani, S., Morikawa, T., Pouliot, G., Racine, J., Moran, M. D., Klimont, Z., Manseau, P. M., Mashayekhi, R., Henderson, B. H., Smith, S. J., Suchyta, H., Muntean, M., Solazzo, E., Banja, M., Schaaf, E., Pagani, F., Woo, J.-H., Kim, J., Monforti-Ferrario, F., Pisoni, E., Zhang, J., Niemi, D., Sassi, M., Ansari, T., and Foley, K.: The HTAP_v3 emission mosaic: merging regional and global monthly emissions (2000–2018) to support air quality modelling and policies, Earth Syst. Sci. Data, 15, 2667–2694, https://doi.org/10.5194/essd-15-2667-2023, 2023.

Crutzen, P. J.: Tropospheric ozone: An overview, in: Isaksen, I. S. A. (Ed.), Tropospheric Ozone, NATO ASI Series, Vol. 227, Springer, Dordrecht, https://doi.org/10.1007/978-94-009-2913-5_1, 1988.

Derwent, R. G., Utembe, S. R., Jenkin, M. E., and Shallcross, D. E.: Tropospheric ozone production regions and the intercontinental origins of surface ozone over Europe, Atmospheric Environment, 112, 216–224, https://doi.org/10.1016/j.atmosenv.2015.04.049, 2015.

Derwent, R. G. and Parrish, D. D.: Analysis and assessment of the observed long-term changes over three decades in ground-level ozone across north-west Europe from 1989 - 2018, Atmospheric Environment, 286, 119222, https://doi.org/10.1016/j.atmosenv.2022.119222, 2022.

Derwent, R. G., Parrish, D. D., and Faloona, I. C.: Opinion: Establishing a science-into-policy process for tropospheric ozone assessment, Atmos. Chem. Phys., 23, 13613–13623, https://doi.org/10.5194/acp-23-13613-2023, 2023.

Elshorbany, Y., Ziemke, J. R., Strode, S., Petetin, H., Miyazaki, K., De Smedt, I., Pickering, K., Seguel, R. J., Worden, H., Emmerichs, T., and Taraborrelli, D.: Tropospheric ozone precursors: global and regional distributions, trends, and variability, Atmos. Chem. Phys., 24, 12225–12257, https://doi.org/10.5194/acp-24-12225-2024, 2024.

Devlin, R. B., McDonnell, W. F., Mann, R., Becker, S., House, D. E., Schreinemachers, D., and Koren, H. S.: Exposure of humans to ambient levels of ozone for 6.6 hours causes cellular and biochemical changes in the lung, Am. J. Respir. Cell Mol. Biol., 4, 72–81, https://doi.org/10.1165/ajrcmb/4.1.72, 1991.

Directive 2008/50/EC on Ambient Air Quality and Cleaner Air for Europe. European Parliament and Council. Directive 2008/50/EC on Ambient Air Quality and Cleaner Air for Europe. Official Journal of the European Union, L 152, 11 June 2008, pp. 1-44. Available at: EUR-Lex.

Du, Q., Zhao, C., Zhang, M., Dong, X., Chen, Y., Liu, Z., Hu, Z., Zhang, Q., Li, Y., Yuan, R., and Miao, S.: Modeling diurnal variation of surface PM2.5 concentrations over East China with WRF-Chem: impacts from boundary-layer mixing and anthropogenic emission, Atmos. Chem. Phys., 20, 2839–2863, https://doi.org/10.5194/acp-20-2839-2020, 2020.

Emmons, L. K., Schwantes, R. H., Orlando, J. J., Tyndall, G., Kinnison, D., Lamarque, J.-F., Marsh, D., Mills, M. J., Tilmes, S., Bardeen, C., et al.: The chemistry mechanism in the community earth system model version 2 (CESM2), Journal of Advances in Modeling Earth Systems, 12, e2019MS001 882, 2020.

Emmons, L., Hess, P., Lamarque, J.-F., and Pfister, G.: Tagged ozone mechanism for MOZART-4, CAM-chem and other chemical transport models, Geoscientific Model Development, 5, 1531–1542, 2012.

European Environment Agency.: Air quality in Europe: 2020 report., Publications Office, LU, 2020.

Felzer, B. S., Cronin, T., Reilly, J. M., Melillo, J. M., and Wang, X.: Impacts of ozone on trees and crops, Comptes Rendus. Géoscience, 339, 784–798, https://doi.org/10.1016/j.crte.2007.08.008, 2007.

Fiore, A. M., Jacob, D. J., Bey, I., Yantosca, R. M., Field, B. D., Fusco, A. C., and Wilkinson, J. G.: Background ozone over the United States in summer: Origin, trend, and contribution to pollution episodes, J. Geophys. Res.-Atmos., 107, ACH 11-1–ACH 11-25, https://doi.org/10.1029/2001JD000982, 2002.

Fiore, A. M., Dentener, F., Wild, O., Cuvelier, C., Schultz, M., Hess, P., Textor, C., Schulz, M., Doherty, R., Horowitz, L., et al.: Multimodel estimates of intercontinental source-receptor relationships for ozone pollution, Journal of Geophysical Research: Atmospheres, 114, 2009

Fleming, Z. L., Doherty, R. M., Von Schneidemesser, E., Malley, C. S., Cooper, O. R., Pinto, J. P., Colette, A., Xu, X., Simpson, D., Schultz, M. G., Lefohn, A. S., Hamad, S., Moolla, R., Solberg, S., and Feng, Z.: Tropospheric Ozone Assessment Report: Present-day ozone distribution and trends relevant to human health, Elementa: Science of the Anthropocene, 6, 12, https://doi.org/10.1525/elementa.273, 2018.

Galmarini, S., Koffi, B., Solazzo, E., Keating, T., Hogrefe, C., Schulz, M., Benedictow, A., Griesfeller, J. J., JanssensMaenhout, G., Carmichael, G., et al.: Coordination and harmonization of the multi-scale, multi-model activities HTAP2, AQMEII3, and MICS-Asia3: simulations, emission inventories, boundary conditions, and model output formats, Atmospheric Chemistry and Physics, 17, 1543–1555, 2017

Gao, Y., Kou, W., Cheng, W., Guo, X., Qu, B., Wu, Y., et al.: Reducing long-standing surface ozone overestimation in Earth system modeling by high-resolution simulation and dry deposition improvement, J. Adv. Model. Earth Sy., 17, e2023MS004192, https://doi.org/10.1029/2023MS004192, 2025.

Garatachea, R., Pay, M. T., Achebak, H., Jorba, O., Bowdalo, D., Guevara, M., Petetin, H., Ballester, J., and Pérez García-Pando, C.: National and transboundary contributions to surface ozone concentration across European countries, Commun Earth Environ, 5, 588, https://doi.org/10.1038/s43247-024-01716-w, 2024.

Goldberg, D. L., Anenberg, S. C., Lu, Z., Streets, D. G., Lamsal, L. N., E McDuffie, E., and Smith, S. J.: Urban NO_X emissions around the world declined faster than anticipated between 2005 and 2019, Environ. Res. Lett., 16, 115004, https://doi.org/10.1088/1748-9326/ac2c34, 2021.

Grewe, V., Tsati, E., and Hoor, P.: On the attribution of contributions of atmospheric trace gases to emissions in atmospheric model applications, Geosci. Model Dev., 3, 487–499, https://doi.org/10.5194/gmd-3-487-2010, 2010.

Grewe, V., Tsati, E., Mertens, M., Frömming, C., and Jöckel, P.: Contribution of emissions to concentrations: the TAGGING 1.0 submodel based on the Modular Earth Submodel System (MESSy 2.52), Geosci. Model Dev., 10, 2615–2633, https://doi.org/10.5194/gmd-10-2615-2017, 2017.

Grulke, N. E. and Heath, R. L.: Ozone effects on plants in natural ecosystems, Plant Biol J, 22, 12–37, https://doi.org/10.1111/plb.12971, 2020.

Guenther, A., Karl, T., Harley, P., Wiedinmyer, C., Palmer, P. I., and Geron, C.: Estimates of global terrestrial isoprene emissions using MEGAN (Model of Emissions of Gases and Aerosols from Nature), Atmos. Chem. Phys., 6, 3181–3210, https://doi.org/10.5194/acp-6-3181-2006, 2006.

Houweling, S., Bergamaschi, P., Chevallier, F., Heimann, M., Kaminski, T., Krol, M., Michalak, A. M., and Patra, P.: Global inverse modeling of CH_4 sources and sinks: an overview of methods, Atmos. Chem. Phys., 17, 235–256, https://doi.org/10.5194/acp-17-235-2017, 2017.

Hu, F., Xie, P., Tian, X., Xu, J., Li, A., Lupaşcu, A., Butler, T., Hu, Z., Lv, Y., Zhang, Z., and Zheng, J.: Integrated analysis of the transport process and source attribution of an extreme ozone pollution event in Hefei at different vertical heights: A case of study, Science of The Total Environment, 906, 167237, https://doi.org/10.1016/j.scitotenv.2023.167237, 2024.

Huang, G., Brook, R., Crippa, M., Janssens-Maenhout, G., Schieberle, C., Dore, C., Guizzardi, D., Muntean, M., Schaaf, E., and Friedrich, R.: Speciation of anthropogenic emissions of non-methane volatile organic compounds: a global gridded data set for 1970–2012, Atmos. Chem. Phys., 17, 7683–7701, https://doi.org/10.5194/acp-17-7683-2017, 2017.

Huang, Y., Partha, D. B., Harper, K., and Heyes, C.: Impacts of Global Solid Biofuel Stove Emissions on Ambient Air Quality and Human Health, GeoHealth, 5, e2020GH000362, https://doi.org/10.1029/2020GH000362, 2021.

Huszar, P., Cariolle, D., Paoli, R., Halenka, T., Belda, M., Schlager, H., Miksovsky, J., and Pisoft, P.: Modeling the regional impact of ship emissions on NOx and ozone levels over the Eastern Atlantic and Western Europe using ship plume parameterization, Atmos. Chem. Phys., 10, 6645–6660, https://doi.org/10.5194/acp-10-6645-2010, 2010.

Jacob, D. J., Logan, J. A., and Murti, P. P.: Effect of rising Asian emissions on surface ozone in the United States, Geophys. Res. Lett., 26, 2175–2178, https://doi.org/10.1029/1999GL900450, 1999.

Jacobson, M. Z.: Fundamentals of Atmospheric Modeling, 2nd edn., Cambridge University Press, Cambridge, UK, 2005.

Jaffe, D., Anderson, T., Covert, D., Kotchenruther, R., Trost, B., Danielson, J., Simpson, W., Berntsen, T., Karlsdottir, S., and Blake, D.: Transport of Asian air pollution to North America, Geophys. Res. Lett., 26, 711–714, https://doi.org/10.1029/1999GL900100, 1999.

Jaffe, D., Price, H., Parrish, D., Goldstein, A., and Harris, J.: Increasing background ozone during spring on the west coast of North America, Geophysical Research Letters, 30, 2003GL017024, https://doi.org/10.1029/2003GL017024, 2003.

Jaffe, D. A., Cooper, O. R., Fiore, A. M., Henderson, B. H., Krol, M., Oltmans, S. J., Parrish, D. D., Prather, M. J., Prinn, R. G., Stohl, A., Van Dingenen, R., and Zhang, L.: Scientific assessment of background ozone over the U.S.: Implications for air quality management, Elem. Sci. Anth., 6, 56, https://doi.org/10.1525/elementa.309, 2018.

Jonson, J. E., Simpson, D., Fagerli, H., and Solberg, S.: Can we explain the trends in European ozone levels?, Atmos. Chem. Phys., 2006.

Kasibhatla, P., Levy II, H., Moxim, W. J., Pandis, S. N., Corbett, J. J., Peterson, M. C., Honrath, R. E., Frost, G. J., Knapp, K., Parrish, D. D., and Ryerson, T. B.: Do emissions from ships have a significant impact on concentrations of nitrogen oxides in the marine boundary layer?, Geophys. Res. Lett., 27, 2229–2232, https://doi.org/10.1029/2000GL011387, 2000.

Lamarque, J.-F., Emmons, L., Hess, P., Kinnison, D. E., Tilmes, S., Vitt, F., Heald, C., Holland, E. A., Lauritzen, P., Neu, J., et al.: CAM-chem: Description and evaluation of interactive atmospheric chemistry in the Community Earth System Model, Geoscientific Model Development, 5, 369–411, 2012.

Lawrence, P. J. and Chase, T. N.: Representing a new MODIS consistent land surface in the Community Land Model (CLM 3.0), J. Geophys. Res., 112, 2006JG000168, https://doi.org/10.1029/2006JG000168, 2007.

Li, P., Yang, Y., Wang, H., Li, S., Li, K., Wang, P., Li, B., and Liao, H.: Source attribution of near-surface ozone trends in the United States during 1995–2019, Atmos. Chem. Phys., 23, 5403–5417, https://doi.org/10.5194/acp-23-5403-2023, 2023.

Lin, M., Fiore, A. M., Cooper, O. R., Horowitz, L. W., Langford, A. O., Levy II, H., Johnson, B. J., Naik, V., Oltmans, S. J., and Senff, C. J.: Springtime high surface ozone events over the western United States: Quantifying the role of stratospheric intrusions, J. Geophys. Res., 117, D00V22, https://doi.org/10.1029/2012JD018151, 2012.

Lin, M., Horowitz, L. W., Cooper, O. R., Tarasick, D., Conley, S., Iraci, L. T., Johnson, B., Leblanc, T., Petropavlovskikh, I., and Yates, E. L.: Revisiting the evidence of increasing springtime ozone mixing ratios in the free troposphere over western North America: TROPOSPHERIC OZONE TRENDS IN WESTERN NA, Geophys. Res. Lett., 42, 8719–8728, https://doi.org/10.1002/2015GL065311, 2015.

Lin, M., Horowitz, L. W., Payton, R., Fiore, A. M., and Tonnesen, G.: US surface ozone trends and extremes from 1980 to 2014: quantifying the roles of rising Asian emissions, domestic controls, wildfires, and climate, Atmos. Chem. Phys., 17, 2943–2970, https://doi.org/10.5194/acp-17-2943-2017, 2017.

Lippmann, M.: Health effects of tropospheric ozone, *Environ. Sci. Technol.*, 25, 1954–1962, https://doi.org/10.1021/es00024a001, 1991.

Liu, S. C., Trainer, M., Fehsenfeld, F. C., Parrish, D. D., Williams, E. J., Fahey, D. W., Hübler, G., and Murphy, P. C.: Ozone production in the rural troposphere and the implications for regional and global ozone distributions, J. Geophys. Res., 92, 4191–4207, https://doi.org/10.1029/JD092iD04p04191, 1987.

Logan, J. A.: Nitrogen oxides in the troposphere: Global and regional budgets, J. Geophys. Res., 88, 10785–10807, https://doi.org/10.1029/JC088iC15p10785, 1983.

Logan, J. A.: Tropospheric ozone: Seasonal behavior, trends, and anthropogenic influence, J. Geophys. Res., 90, 10463–10482, https://doi.org/10.1029/JD090iD06p10463, 1985.

Logan, J. A., Staehelin, J., Megretskaia, I. A., Cammas, J.-P., Thouret, V., Claude, H., De Backer, H., Steinbacher, M., Scheel, H. E., Stübi, R., Fröhlich, M., and Derwent, R.: Changes in ozone over Europe: analysis of ozone measurements from sondes, regular aircraft (MOZAIC) and alpine surface sites, J. Geophys. Res., 117, D09301, https://doi.org/10.1029/2011JD016952, 2012.

Lu, X., Zhang, L., Wang, X., Gao, M., Zhao, Y., Chen, D., Zhou, M., Zhang, Q., Chang, K.-L., Cooper, O. R., Lin, M., Lin, J., Meng, J., Ni, R., Su, H., Virkkula, A., Yan, Y., and Zhang, Y.: Tropospheric ozone trends and attributions over East and Southeast Asia in 1995–2019: An integrated assessment using statistical methods, machine learning models, and multiple chemical transport models, Atmos. Chem. Phys. Discuss. [preprint], https://doi.org/10.5194/acp-2023-741, in review, 2024.

Lupascu, A. and Butler, T.: Source attribution of European surface O_3 using a tagged O_3 mechanism, Atmospheric Chemistry and Physics, 19, 14 535–14 558, 2019.

Lupascu, A., Otero, N., Minkos, A., and Butler, T.: Attribution of surface ozone to NO_X and volatile organic compound sources during two different high ozone events, Atmospheric chemistry and physics, 22, 11 675–11 699, 2022

Lupaşcu, A., Otero, N., Minkos, A., and Butler, T.: Attribution of surface ozone to NO_X and volatile organic compound sources during two different high ozone events, Atmos. Chem. Phys., 22, 11675–11699, https://doi.org/10.5194/acp-22-11675-2022, 2022.

Mathur, R., Kang, D., Napelenok, S. L., Xing, J., Hogrefe, C., Sarwar, G., Itahashi, S., and Henderson, B. H.: How Have Divergent Global Emission Trends Influenced Long-Range Transported Ozone to North America?, JGR Atmospheres, 127, e2022JD036926, https://doi.org/10.1029/2022JD036926, 2022a.

Mathur, R., Kang, D., Napelenok, S. L., Xing, J., Hogrefe, C., Sarwar, G., Itahashi, S., and Henderson, B. H.: How Have Divergent Global Emission Trends Influenced Long-Range Transported Ozone to North America?, JGR Atmospheres, 127, e2022JD036926, https://doi.org/10.1029/2022JD036926, 2022b.

Mertens, M., Kerkweg, A., Grewe, V., Jöckel, P., and Sausen, R.: Attributing ozone and its precursors to land transport emissions in Europe and Germany, Atmos. Chem. Phys., 20, 7843–7873, https://doi.org/10.5194/acp-20-7843-2020, 2020.

Mertens, M., Kerkweg, A., Grewe, V., Jöckel, P., and Sausen, R.: Attributing ozone and its precursors to land transport emissions in Europe and Germany, Atmospheric Chemistry and Physics (ACP), pp. 7843–7873, 2020.

Mills, G., Sharps, K., Simpson, D., Pleijel, H., Frei, M., Burkey, K., Emberson, L., Uddling, J., Broberg, M., Feng, Z., Kobayashi, K., and Agrawal, M.: Ozone pollution will compromise efforts to increase global wheat production, Glob. Change Biol., 24, 3560–3574, https://doi.org/10.1111/gcb.14157, 2018.

Molod, A., Takacs, L., Suarez, M., and Bacmeister, J.: Development of the GEOS-5 atmospheric general circulation model: evolution from MERRA to MERRA2, Geosci. Model Dev., 8, 1339–1356, https://doi.org/10.5194/gmd-8-1339-2015, 2015.

Nalam, A., Lupaşcu, A., Ansari, T., and Butler, T.: Regional and sectoral contributions of NOx and reactive carbon emission sources to global trends in tropospheric ozone during the 2000–2018 period, Atmos. Chem. Phys., 25, 5287–5311, https://doi.org/10.5194/acp-25-5287-2025, 2025.~~Nalam, A., Lupascu, A., Ansari, T., and Butler, T.: Regional and sectoral contributions of NO_X and reactive carbon emission sources to global trends in tropospheric ozone during the 2000–2018 period, EGUsphere [preprint], https://doi.org/10.5194/egusphere-2024-432, 2024.¶~~

Oeschger, H., and Dütsch, H. U.: Ozone and the greenhouse effect, *Nature*, 339, 19, https://doi.org/10.1038/339019a0, 1989.

Parrish, D. D. and Ennis, C. A.: Estimating background contributions and US anthropogenic enhancements to maximum ozone concentrations in the northern US, Atmos. Chem. Phys., 19, 12587–12605, https://doi.org/10.5194/acp-19-12587-2019, 2019.

Parrish, D. D., Law, K. S., Staehelin, J., Derwent, R., Cooper, O. R., Tanimoto, H., Volz-Thomas, A., Gilge, S., Scheel, H.-E., Steinbacher, M., and Chan, E.: Lower tropospheric ozone at northern midlatitudes: Changing seasonal cycle, Geophysical Research Letters, 40, 1631–1636, https://doi.org/10.1002/grl.50303, 2013.

Parrish, D. D., Lamarque, J.-F., Naik, V., Horowitz, L., Shindell, D. T., Staehelin, J., Derwent, R., Cooper, O. R., and Tanimoto, H.: Seasonal cycles of O3 in the marine boundary layer: Observation and model simulation comparisons, J. Geophys. Res.-Atmos., 121, 538–557, https://doi.org/10.1002/2015JD024101, 2016.

Parrish, D. D., Derwent, R. G., Steinbrecht, W., Stübi, R., Van Malderen, R., Steinbacher, M., and others: Zonal similarity of long-term changes and seasonal cycles of baseline ozone at northern mid-latitudes, J. Geophys. Res.: Atmos., 125, e2019JD031908, https://doi.org/10.1029/2019JD031908, 2020.

Parrish, D. D., Faloona, I. C., and Derwent, R. G.: Observational-based assessment of contributions to maximum ozone concentrations in the western United States, Journal of the Air & Waste Management Association, 72, 434–454, https://doi.org/10.1080/10962247.2022.2050962, 2022.

Parrish, D. D., Faloona, I. C., and Derwent, R. G.: Maximum ozone concentrations in the southwestern US and Texas: implications of the growing predominance of the background contribution, Atmos. Chem. Phys., 25, 263–289, https://doi.org/10.5194/acp-25-263-2025, 2025.

Price, C. and Rind, D.: A simple lightning parameterization for calculating global lightning distributions, J. Geophys. Res., 97, 9919–9933, doi:10.1029/92JD00719, 1992.

Price, C., Penner, J., and Prather, M.: NO_X from lightning 1, Global distribution based on lightning physics, J. Geophys. Res., 102, 5929–5941, 1997

Real, E., Law, K. S., Weinzierl, B., Fiebig, M., Petzold, A., Wild, O., Methven, J., Arnold, S., Stohl, A., Huntrieser, H., Roiger, A., Schlager, H., Stewart, D., Avery, M., Sachse, G., Browell, E., Ferrare, R., and Blake, D.: Processes influencing ozone levels in Alaskan forest fire plumes during long-range transport over the North Atlantic, J. Geophys. Res., 112, 2006JD007576, https://doi.org/10.1029/2006JD007576, 2007.

Reidmiller, D. R., Fiore, A. M., Jaffe, D. A., Bergmann, D., Cuvelier, C., Dentener, F. J., Duncan, B. N., Folberth, G., Gauss, M., Gong, S., Hess, P., Jonson, J. E., Keating, T., Lupu, A., Marmer, E., Park, R., Schultz, M. G., Shindell, D. T., Szopa, S.,

Vivanco, M. G., Wild, O., and Zuber, A.: The influence of foreign vs. North American emissions on surface ozone in the US, Atmos. Chem. Phys., 2009.

Rieger, V. S., Mertens, M., and Grewe, V.: An advanced method of contributing emissions to short-lived chemical species (OH and HO₂): the TAGGING 1.1 submodel based on the Modular Earth Submodel System (MESSy 2.53), Geosci. Model Dev., 11, 2049–2066, https://doi.org/10.5194/gmd-11-2049-2018, 2018.

Romero-Alvarez, J., Lupaşcu, A., Lowe, D., Badia, A., Archer-Nicholls, S., Dorling, S., Reeves, C. E., and Butler, T.: Sources of surface O_3 in the UK: tagging O_3 within WRF-Chem, Atmos. Chem. Phys., 22, 13797–13815, https://doi.org/10.5194/acp-22-13797-2022, 2022.

Schultz, M. G., Schröder, S., Lyapina, O., Cooper, O. R., Galbally, I., Petropavlovskikh, I., Von Schneidemesser, E., Tanimoto, H., Elshorbany, Y., Naja, M., et al.: Tropospheric Ozone Assessment Report: Database and metrics data of global surface ozone observations, Elem Sci Anth, 5, 58, 2017.

Schultz, M. G., Schröder, S., Lyapina, O., Cooper, O. R., Galbally, I., Petropavlovskikh, I., Von Schneidemesser, E., Tanimoto, H., Elshorbany, Y., Naja, M., Seguel, R. J., Dauert, U., Eckhardt, P., Feigenspan, S., Fiebig, M., Hjellbrekke, A.-G., Hong, Y.-D., Kjeld, P. C., Koide, H., Lear, G., Tarasick, D., Ueno, M., Wallasch, M., Baumgardner, D., Chuang, M.-T., Gillett, R., Lee, M., Molloy, S., Moolla, R., Wang, T., Sharps, K., Adame, J. A., Ancellet, G., Apadula, F., Artaxo, P., Barlasina, M. E., Bogucka, M., Bonasoni, P., Chang, L., Colomb, A., Cuevas-Agulló, E., Cupeiro, M., Degorska, A., Ding, A., Fröhlich, M., Frolova, M., Gadhavi, H., Gheusi, F., Gilge, S., Gonzalez, M. Y., Gros, V., Hamad, S. H., Helmig, D., Henriques, D., Hermansen, O., Holla, R., Hueber, J., Im, U., Jaffe, D. A., Komala, N., Kubistin, D., Lam, K.-S., Laurila, T., Lee, H., Levy, I., Mazzoleni, C., Mazzoleni, L. R., McClure-Begley, A., Mohamad, M., Murovec, M., Navarro-Comas, M., Nicodim, F., Parrish, D., Read, K. A., Reid, N., Ries, L., Saxena, P., Schwab, J. J., Scorgie, Y., Senik, I., Simmonds, P., Sinha, V., Skorokhod, A. I., Spain, G., Spangl, W., Spoor, R., Springston, S. R., Steer, K., Steinbacher, M., Suharguniyawan, E., Torre, P., Trickl, T., Weili, L., Weller, R., Xiaobin, X., Xue, L., and Zhiqiang, M.: Tropospheric Ozone Assessment Report: Database and metrics data of global surface ozone observations, Elementa: Science of the Anthropocene, 5, 58, https://doi.org/10.1525/elementa.244, 2017.

Seinfeld, J. H. and Pandis, S. N.: Atmospheric Chemistry and Physics: From Air Pollution to Climate Change, 3rd edn., Wiley, Hoboken, NJ, USA, 2016.

Seltzer, K. M., Shindell, D. T., Kasibhatla, P., and Malley, C. S.: Magnitude, trends, and impacts of ambient long-term ozone exposure in the United States from 2000 to 2015, Atmos. Chem. Phys., 20, 1757–1775, https://doi.org/10.5194/acp-20-1757-2020, 2020.

¶

Shaw, S. and Van Heyst, B.: Nitrogen Oxide (NO_X) emissions as an indicator for sustainability, Environmental and Sustainability Indicators, 15, 100188, https://doi.org/10.1016/j.indic.2022.100188, 2022.

Sicard, P.: Ground-level ozone over time: An observation-based global overview, Current Opinion in Environmental Science & Health, 19, 100226, https://doi.org/10.1016/j.coesh.2020.100226, 2021.

Simon, H., Reff, A., Wells, B., Xing, J., and Frank, N.: Ozone Trends Across the United States over a Period of Decreasing NO_X and VOC Emissions, Environ. Sci. Technol., 49, 186–195, https://doi.org/10.1021/es504514z, 2015.

Simon, H., Hogrefe, C., Whitehill, A., Foley, K. M., Liljegren, J., Possiel, N., Wells, B., Henderson, B. H., Valin, L. C., Tonnesen, G., Appel, K. W., and Koplitz, S.: Revisiting day-of-week ozone patterns in an era of evolving US air quality, Atmos. Chem. Phys., 24, 1855–1871, https://doi.org/10.5194/acp-24-1855-2024, 2024.

Sindelarova, K., Markova, J., Simpson, D., Huszar, P., Karlicky, J., Darras, S., Granier, C.: Copernicus Atmosphere Monitoring Service Global Biogenic VOC emissions version 3.0 (CAMS-GLOB-BIO v3.0), ECCAD, https://doi.org/10.24380/xs64-gj42, 2021.

Sitch, S., Cox, P. M., Collins, W. J., and Huntingford, C.: Indirect radiative forcing of climate change through ozone effects on the land-carbon sink, Nature, 448, 791–794, https://doi.org/10.1038/nature06059, 2007.

Solberg, S., Hov, Ø., Søvde, A., Isaksen, I. S. A., Coddeville, P., De Backer, H., Forster, C., Orsolini, Y., and Uhse, K.: European surface ozone in the extreme summer 2003, J. Geophys. Res., 113, 2007JD009098, https://doi.org/10.1029/2007JD009098, 2008.

Stevenson, D. S., Dentener, F. J., Schultz, M. G., Ellingsen, K., Van Noije, T. P. C., Wild, O., Zeng, G., Amann, M., Atherton, C. S., Bell, N., Bergmann, D. J., Bey, I., Butler, T., Cofala, J., Collins, W. J., Derwent, R. G., Doherty, R. M., Drevet, J., Eskes, H. J., Fiore, A. M., Gauss, M., Hauglustaine, D. A., Horowitz, L. W., Isaksen, I. S. A., Krol, M. C., Lamarque, J. -F., Lawrence, M. G., Montanaro, V., Müller, J. -F., Pitari, G., Prather, M. J., Pyle, J. A., Rast, S., Rodriguez, J. M., Sanderson, M. G., Savage, N. H., Shindell, D. T., Strahan, S. E., Sudo, K., and Szopa, S.: Multimodel ensemble

simulations of present-day and near-future tropospheric ozone, J. Geophys. Res., 111, 2005JD006338, https://doi.org/10.1029/2005JD006338, 2006.

Strode, S. A., Rodriguez, J. M., Logan, J. A., Cooper, O. R., Witte, J. C., Lamsal, L. N., Damon, M., Van Aartsen, B., Steenrod, S. D., and Strahan, S. E.: Trends and variability in surface ozone over the United States, JGR Atmospheres, 120, 9020–9042, https://doi.org/10.1002/2014JD022784, 2015.

Struzewska, J. and Kaminski, J. W.: Formation and transport of photooxidants over Europe during the July 2006 heat wave – observations and GEM-AQ model simulations, Atmos. Chem. Phys., 8, 721–736, https://doi.org/10.5194/acp-8-721-2008, 2008.

Szopa, S., Naik, V., Adhikary, B., Artaxo, P., Berntsen, T., Collins, W. D., Fuzzi, S., Gallardo, L., Gidden, M., Kirtman, B., Krishnan, R., Lecocq, F., Mbow, C., Myhre, G., Pörtner, H.-O., Riahi, K., Rogelj, J., Sillmann, J., and Zanis, P.: Short-Lived Climate Forcers, in: Climate Change 2021: The Physical Science Basis. Contribution of Working Group I to the Sixth Assessment Report of the Intergovernmental Panel on Climate Change, edited by: Masson-Delmotte, V., Zhai, P., Pirani, A., Connors, S. L., Péan, C., Berger, S., Caud, N., Chen, Y., Goldfarb, L., Gomis, M. I., Huang, M., Leitzell, K., Lonnoy, E., Matthews, J. B. R., Maycock, T. K., Waterfield, T., Yelekçi, Ö., Yu, R., and Zhou, B., Cambridge University Press, Cambridge, United Kingdom and New York, NY, USA, pp. 817–922, https://doi.org/10.1017/9781009157896.008, 2021.

Tilmes, S., Lamarque, J.-F., Emmons, L., Kinnison, D., Ma, P.-L., Liu, X., Ghan, S., Bardeen, C., Arnold, S., Deeter, M., et al.: Description and evaluation of tropospheric chemistry and aerosols in the Community Earth System Model (CESM1. 2), Geoscientific Model Development, 8, 1395–1426, 2015

TOAR Gridding Tool. https://gitlab.jsc.fz-juelich.de/esde/toar-public/toargridding; Last access 22nd October 2024.

TOAR analysis. Selke, Niklas; Schröder, Sabine; Schultz, Martin. TOAR Analysis Service. FZ-Juelich. https://toar-data.fz-juelich.de/api/v2/analysis/, 2023

TOAR-II. Schröder, Sabine; Schultz, Martin G.; Selke, Niklas; Sun, Jianing; Ahring, Jessica; Mozaffari, Amirpasha; Romberg, Mathilde; Epp, Eleonora; Lensing, Max; Apweiler, Sander; Leufen, Lukas H.; Betancourt, Clara; Hagemeier, Björn; Rajveer, Saini. TOAR Data Infrastructure. FZ-Juelich B2SHARE. https://doi.org/10.34730/4D9A287DEC0B42F1AA6D244DE8F19EB3, 2021

UNEP and CCAC: Global Methane Assessment: Benefits and Costs of Mitigating Methane Emissions, United Nations Environment Programme and Climate and Clean Air Coalition, Nairobi, Kenya, 2021.

U.S. EPA: Preparation of Emissions Inventories for the Version 7.1 2016 Hemispheric Emissions Modeling Platform, U.S. Environmental Protection Agency, available at: https://www.epa.gov/sites/default/files/2019-12/documents/2016fe_hemispheric_tsd.pdf, last access: [27 November 2024], November 2019.

Van der Werf, G. R., Randerson, J. T., Giglio, L., Collatz, G., Mu, M., Kasibhatla, P. S., Morton, D. C., DeFries, R., Jin, Y. v., and van Leeuwen, T. T.: Global fire emissions and the contribution of deforestation, savanna, forest, agricultural, and peat fires (1997–2009), Atmospheric chemistry and physics, 10, 11 707–11 735, 2010.

Van Dingenen, R., Dentener, F. J., Raes, F., Krol, M. C., Emberson, L., and Cofala, J.: The global impact of ozone on agricultural crop yields under current and future air quality legislation, Atmospheric Environment, 43, 604–618, https://doi.org/10.1016/j.atmosenv.2008.10.033, 2009.

Vautard, R., Gobiet, A., Jacob, D., Belda, M., Colette, A., Déqué, M., Fernández, J., García-Díez, M., Goergen, K., Güttler, I., Halenka, T., Karacostas, T., Katragkou, E., Keuler, K., Kotlarski, S., Mayer, S., Van Meijgaard, E., Nikulin, G., Patarčić, M., Scinocca, J., Sobolowski, S., Suklitsch, M., Teichmann, C., Warrach-Sagi, K., Wulfmeyer, V., and Yiou, P.: The simulation of European heat waves from an ensemble of regional climate models within the EURO-CORDEX project, Clim Dyn, 41, 2555–2575, https://doi.org/10.1007/s00382-013-1714-z, 2013.

Wang, Y., and Jacob, D. J.: Anthropogenic forcing on tropospheric ozone and OH since preindustrial times, J. Geophys. Res.: Atmos., 103, 31123–31135, https://doi.org/10.1029/98JD02225, 1998.

Wild, O., Fiore, A. M., Shindell, D. T., Doherty, R. M., Collins, W. J., Dentener, F. J., Schultz, M. G., Gong, S., MacKenzie, I. A., Zeng, G., Hess, P., Duncan, B. N., Bergmann, D. J., Szopa, S., Jonson, J. E., Keating, T. J., and Zuber, A.: Modelling future changes in surface ozone: a parameterized approach, Atmos. Chem. Phys., 12, 2037–2054, https://doi.org/10.5194/acp-12-2037-2012, 2012.

Wolff, G. T., Dunker, A. M., Rao, S. T., Porter, P. S., and Zurbenko, I. G.: Ozone Air Quality over North America: Part I—A Review of Reported Trends, Journal of the Air & Waste Management Association, 51, 273–282, https://doi.org/10.1080/10473289.2001.10464270, 2001.

World Health Organization. WHO Global Air Quality Guidelines: Particulate Matter (PM2.5 and PM10), Ozone, Nitrogen Dioxide, Sulfur Dioxide, and Carbon $MoNO_x$ide. Geneva: World Health Organization. Available at: WHO IRIS Repository. License: CC BY-NC-SA 3.0 IGO, 2021

Yan, Y., Pozzer, A., Ojha, N., Lin, J., and Lelieveld, J.: Analysis of European ozone trends in the period 1995–2014, Atmos. Chem. Phys., 18, 5589–5605, https://doi.org/10.5194/acp-18-5589-2018, 2018.

Young, P. J., Archibald, A. T., Bowman, K. W., Lamarque, J.-F., Naik, V., Stevenson, D. S., Tilmes, S., Voulgarakis, A., Wild, O., Bergmann, D., Cameron-Smith, P., Cionni, I., Collins, W. J., Dalsøren, S. B., Doherty, R. M., Eyring, V., Faluvegi, G., Horowitz, L. W., Josse, B., Lee, Y. H., MacKenzie, I. A., Nagashima, T., Plummer, D. A., Righi, M., Rumbold, S. T., Skeie, R. B., Shindell, D. T., Strode, S. A., Sudo, K., Szopa, S., and Zeng, G.: Pre-industrial to end 21st century projections of tropospheric ozone from the Atmospheric Chemistry and Climate Model Intercomparison Project (ACCMIP), Atmos. Chem. Phys., 13, 2063–2090, https://doi.org/10.5194/acp-13-2063-2013, 2013.

Young, P. J., Naik, V., Fiore, A. M., Gaudel, A., Guo, J., Lin, M. Y., Neu, J. L., Parrish, D. D., Rieder, H. E., Schnell, J. L., Tilmes, S., Wild, O., Zhang, L., Ziemke, J., Brandt, J., Delcloo, A., Doherty, R. M., Geels, C., Hegglin, M. I., Hu, L., Im, U., Kumar, R., Luhar, A., Murray, L., Plummer, D., Rodriguez, J., Saiz-Lopez, A., Schultz, M. G., Woodhouse, M. T., and Zeng, G.: Tropospheric Ozone Assessment Report: Assessment of global-scale model performance for global and regional ozone distributions, variability, and trends, Elementa: Science of the Anthropocene, 6, 10, https://doi.org/10.1525/elementa.265, 2018.

Zheng, B., Tong, D., Li, M., Liu, F., Hong, C., Geng, G., Li, H., Li, X., Peng, L., Qi, J., Yan, L., Zhang, Y., Zhao, H., Zheng, Y., He, K., and Zhang, Q.: Trends in China's anthropogenic emissions since 2010 as the consequence of clean air actions, Atmos. Chem. Phys., 18, 14095–14111, https://doi.org/10.5194/acp-18-14095-2018, 2018.

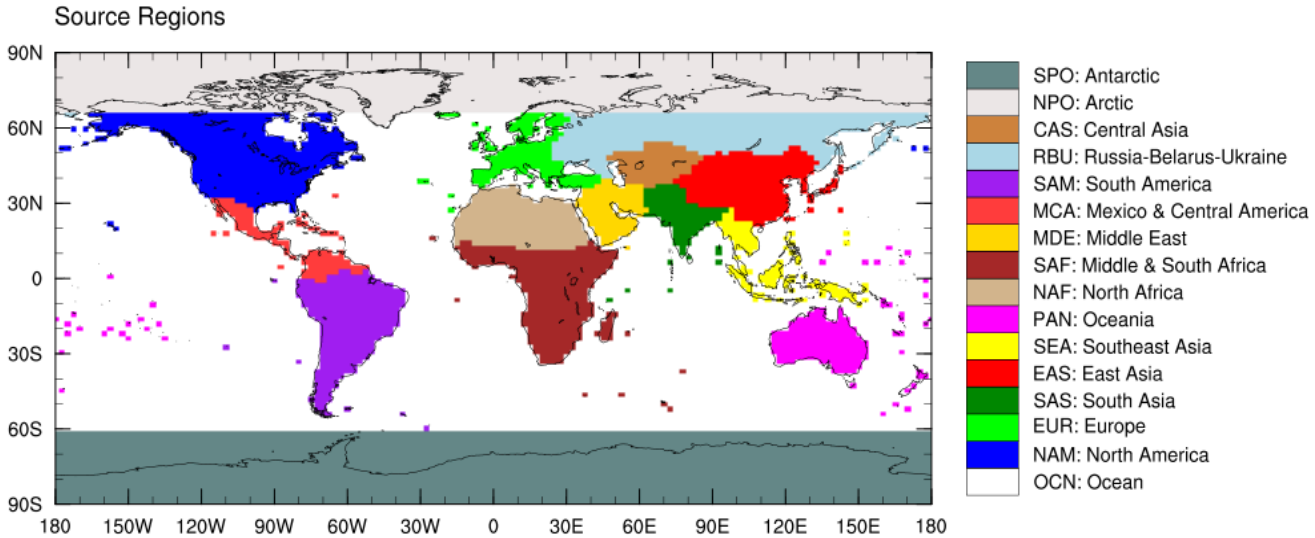

Figure 1: HTAP Tier 1 regions which form the basis for source regions for NO_X and VOC tagging. Oceanic tagged regions are shown in Figure S12. More details on tagged regions are provided in Table 1.

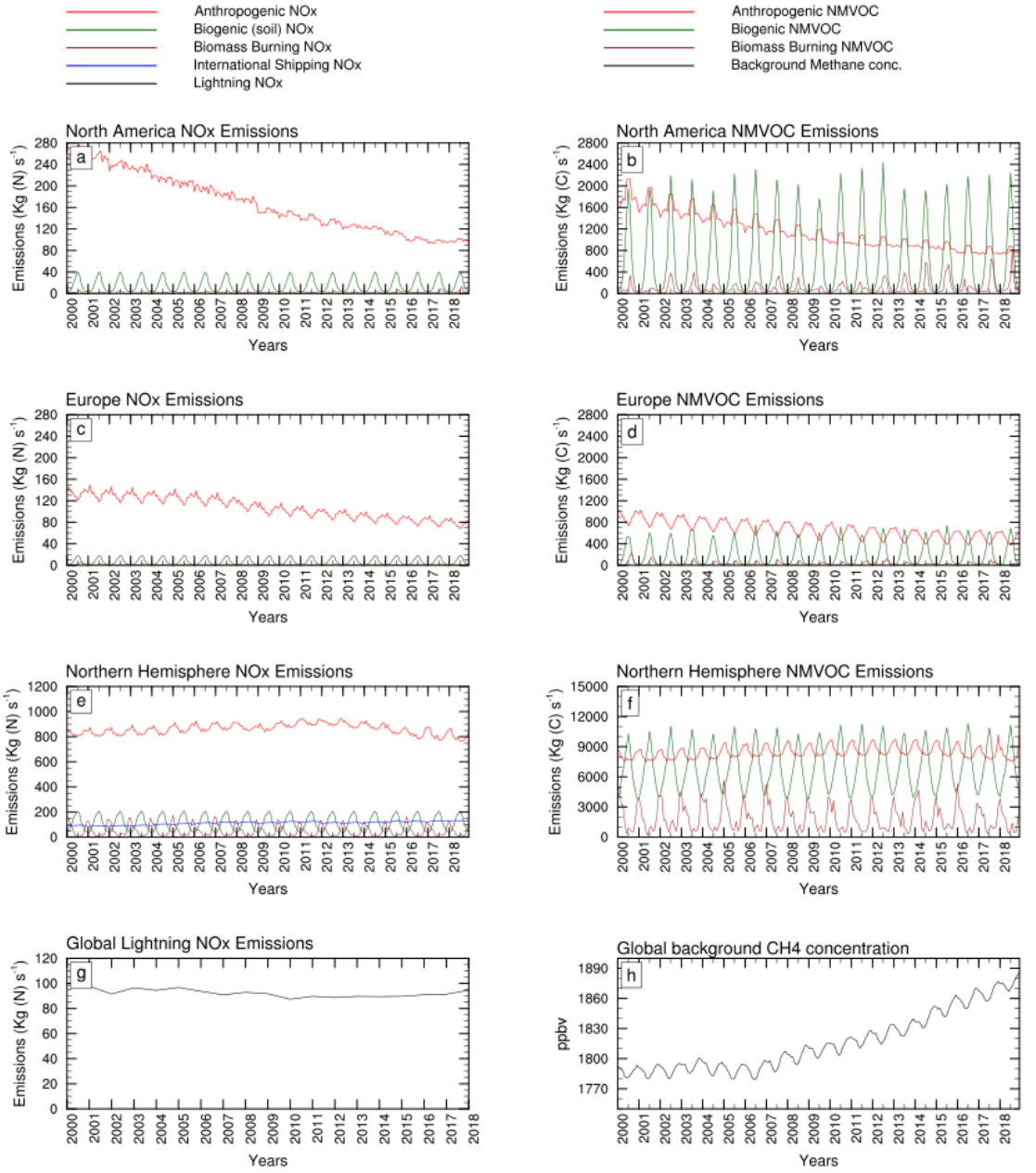
Anthropogenic NOx
Biogenic (soil) NOx
Biomass Burning NOx
International Shipping NOx
Lightning NOx
Anthropogenic NMVOC
Biogenic NMVOC
Biomass Burning NMVOC
Background Methane conc.
North America NOx Emissions
North America NMVOC Emissions
Europe NOx Emissions
Europe NMVOC Emissions
Northern Hemisphere NOx Emissions
Northern Hemisphere NMVOC Emissions
Global Lightning NOx Emissions
Global background CH4 concentration
Emissions (Kg (N) s-1)
Emissions (Kg (C) s-1)
ppbv
Years

Figure 2: Time-series of NO_X- (left panels) and VOC-emissions (right panels) for North America (a, b), and Europe (c, d) source regions along with Northern Hemispheric totals (e, f) and global totals of lightning NO_X and background CH_4 concentrations over the study period.

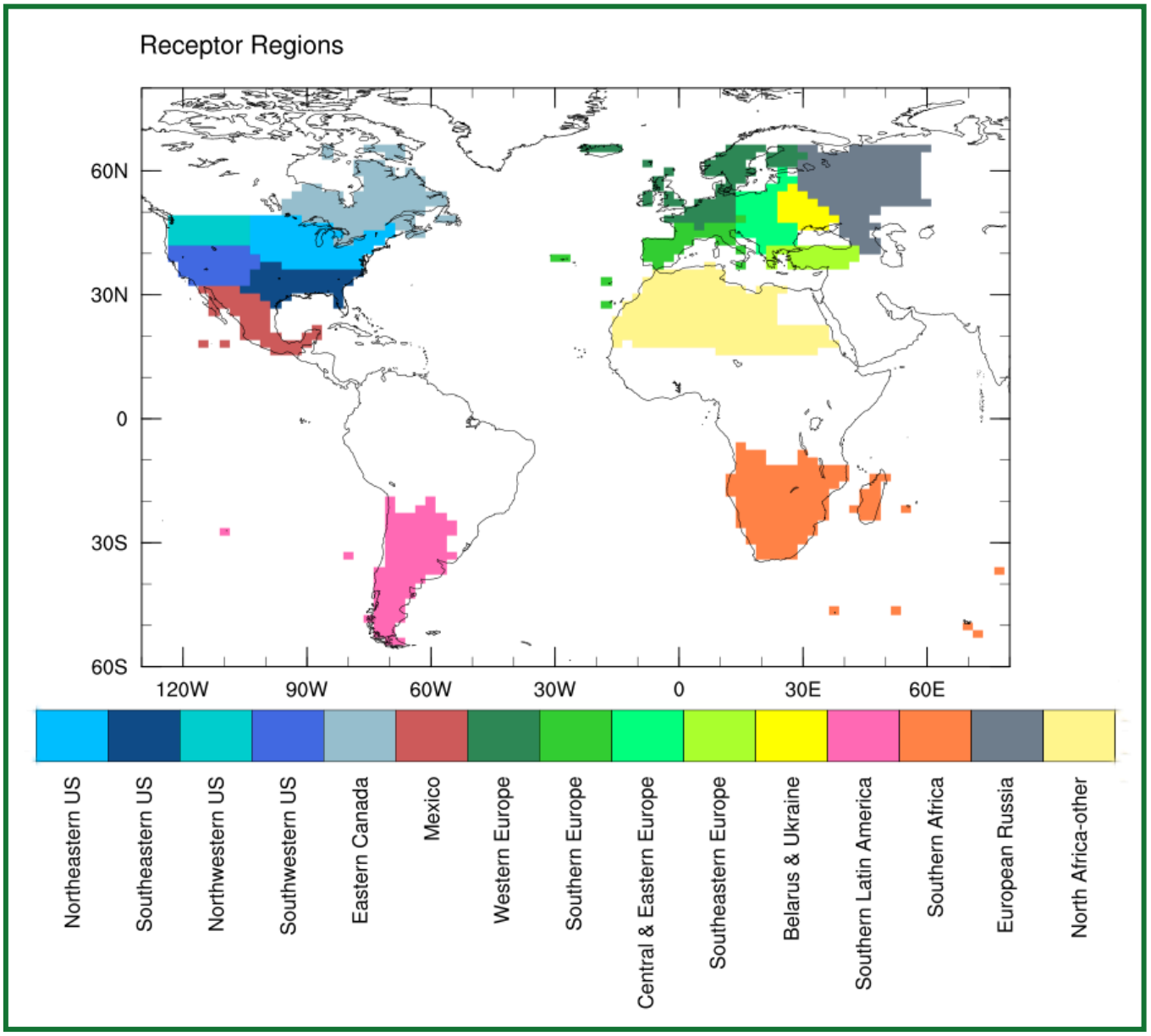
Receptor Regions
60N
30N
0
30S
60S
120W
90W
60W
30W
0
30E
60E
Northeastern US
Southeastern US
Northwestern US
Southwestern US
Eastern Canada
Mexico
Western Europe
Southern Europe
Central & Eastern Europe
Southeastern Europe
Belarus & Ukraine
Southern Latin America
Southern Africa
European Russia
North Africa-other

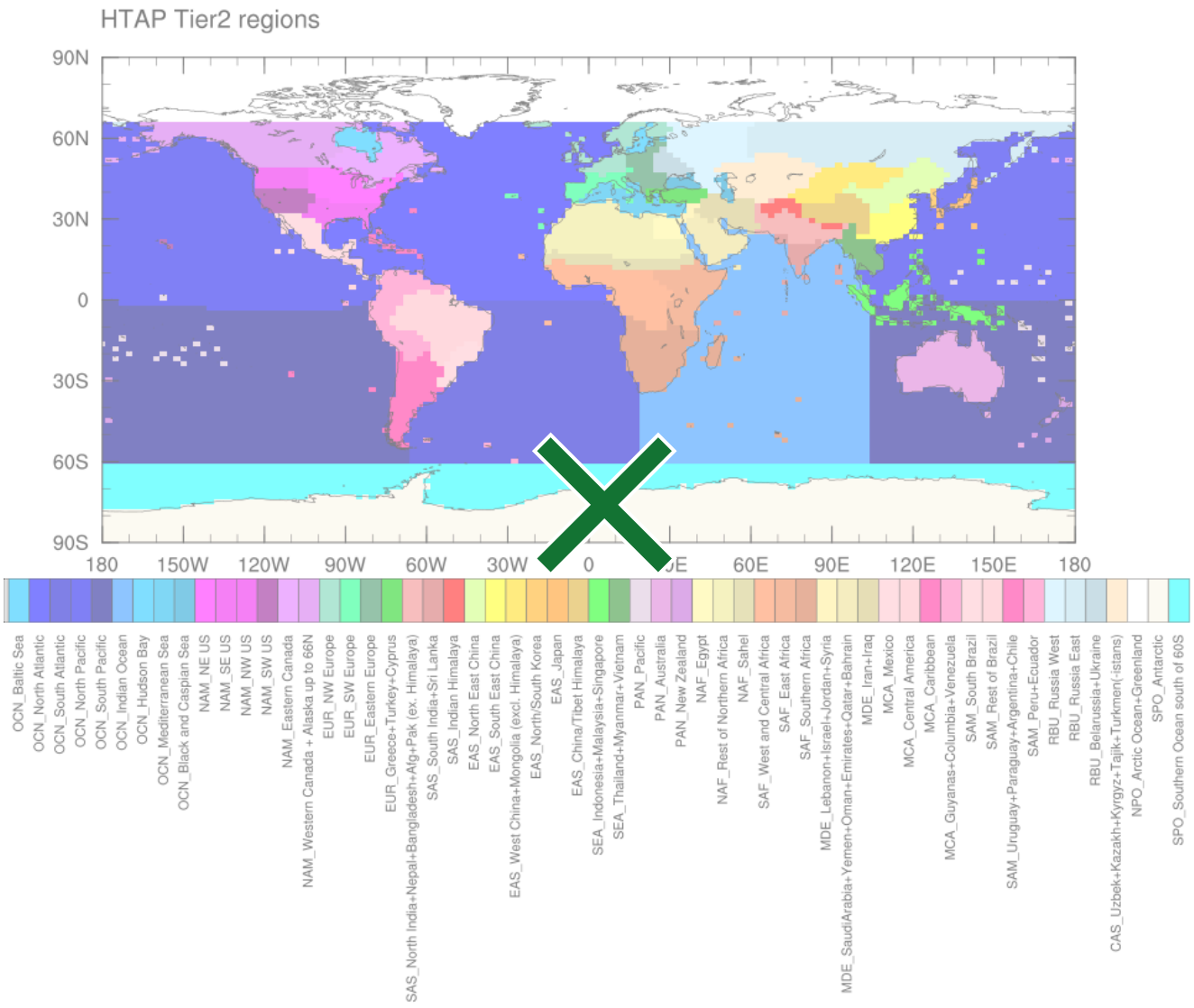

Figure 3: ~~RHTAP Tier 2~~ receptor regions considered for model evaluation or analysis. Note that many regions were sparsely sampled due to lack of a wide rural observational network within these regions.

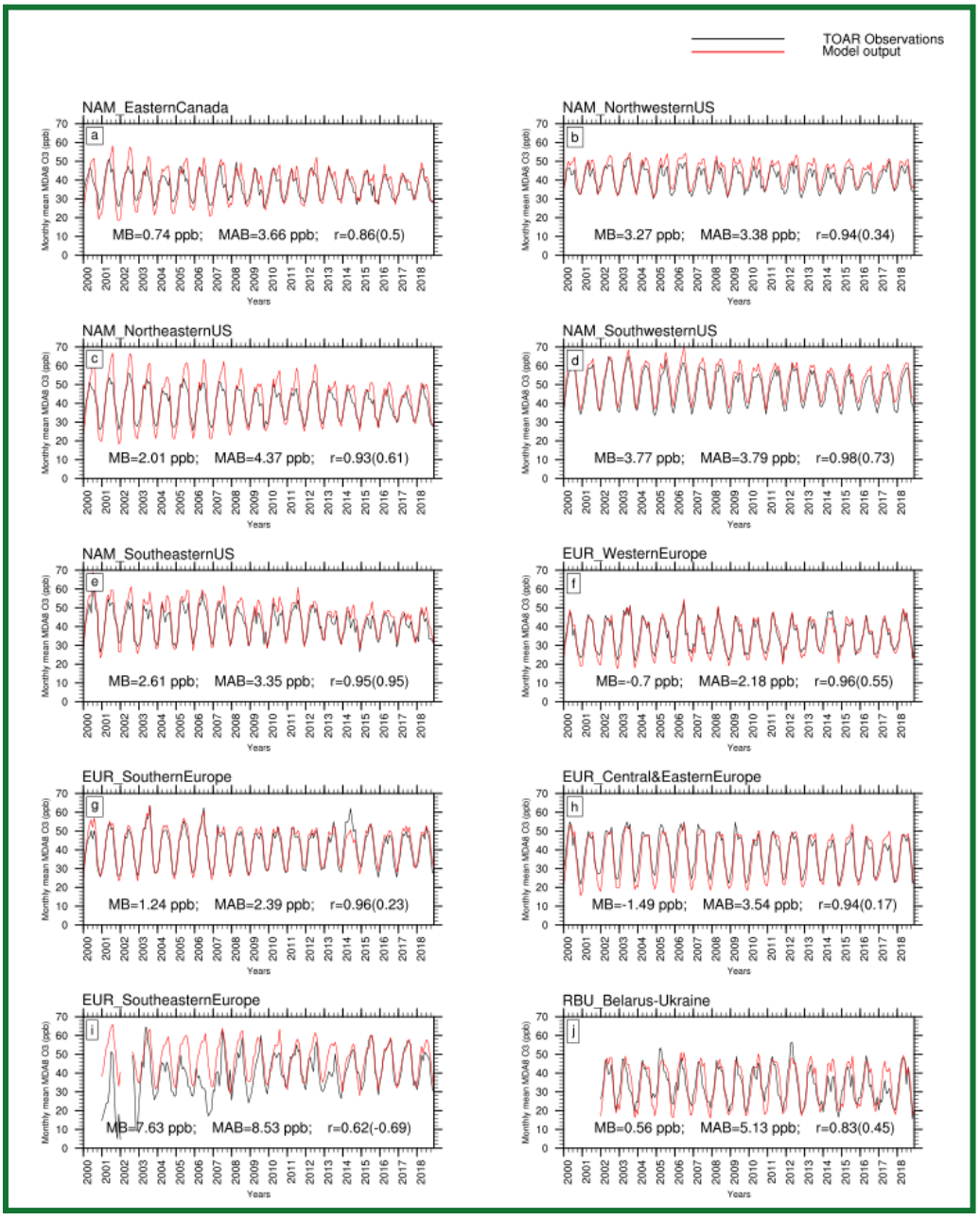
TOAR Observations
Model output
NAM_EasternCanada
a
MB=0.74 ppb; MAB=3.66 ppb; r=0.86(0.5)
NAM_NorthwesternUS
b
MB=3.27 ppb; MAB=3.38 ppb; r=0.94(0.34)
NAM_NortheasternUS
c
MB=2.01 ppb; MAB=4.37 ppb; r=0.93(0.61)
NAM_SouthwesternUS
d
MB=3.77 ppb; MAB=3.79 ppb; r=0.98(0.73)
NAM_SoutheasternUS
e
MB=2.61 ppb; MAB=3.35 ppb; r=0.95(0.95)
EUR_WesternEurope
f
MB=-0.7 ppb; MAB=2.18 ppb; r=0.96(0.55)
EUR_SouthernEurope
g
MB=1.24 ppb; MAB=2.39 ppb; r=0.96(0.23)
EUR_Central&EasternEurope
h
MB=-1.49 ppb; MAB=3.54 ppb; r=0.94(0.17)
EUR_SoutheasternEurope
i
MB=-7.63 ppb; MAB=8.53 ppb; r=0.62(-0.69)
RBU_Belarus-Ukraine
j
MB=0.56 ppb; MAB=5.13 ppb; r=0.83(0.45)
Monthly mean MDA8 O3 (ppb)
Years

2143


TOAR Observations
Model output
NAM_EasternCanada (MB=0.68 ppb r=0.86)
NAM_NorthwesternUS (MB=3.36 ppb r=0.92)
NAM_NortheasternUS (MB=1.97 ppb r=0.93)
NAM_SouthwesternUS (MB=3.65 ppb r=0.98)
NAM_SoutheasternUS (MB=2.62 ppb r=0.95)
EUR_WesternEurope (MB=-0.73 ppb r=0.97)
EUR_SouthernEurope (MB=1.25 ppb r=0.96)
EUR_Central&EasternEurope (MB=-1.54 ppb r=0.94)
EUR_SoutheasternEurope (MB=7.63 ppb r=0.62)
RBU_Belarus-Ukraine (MB=0.56 ppb r=0.83)
Monthly mean MDA8 O3 (ppb)
Years

2144

Figure 4: Time series of observed versus simulated monthly mean MDA8 O_3 along with mean bias, mean absolute bias, and correlation coefficients for various receptor regions. Correlation coefficients for annual averaged data are mentioned in brackets. Only rural stations data were utilized from the TOAR database and model output was fetched only for those grid cells where observations were available.

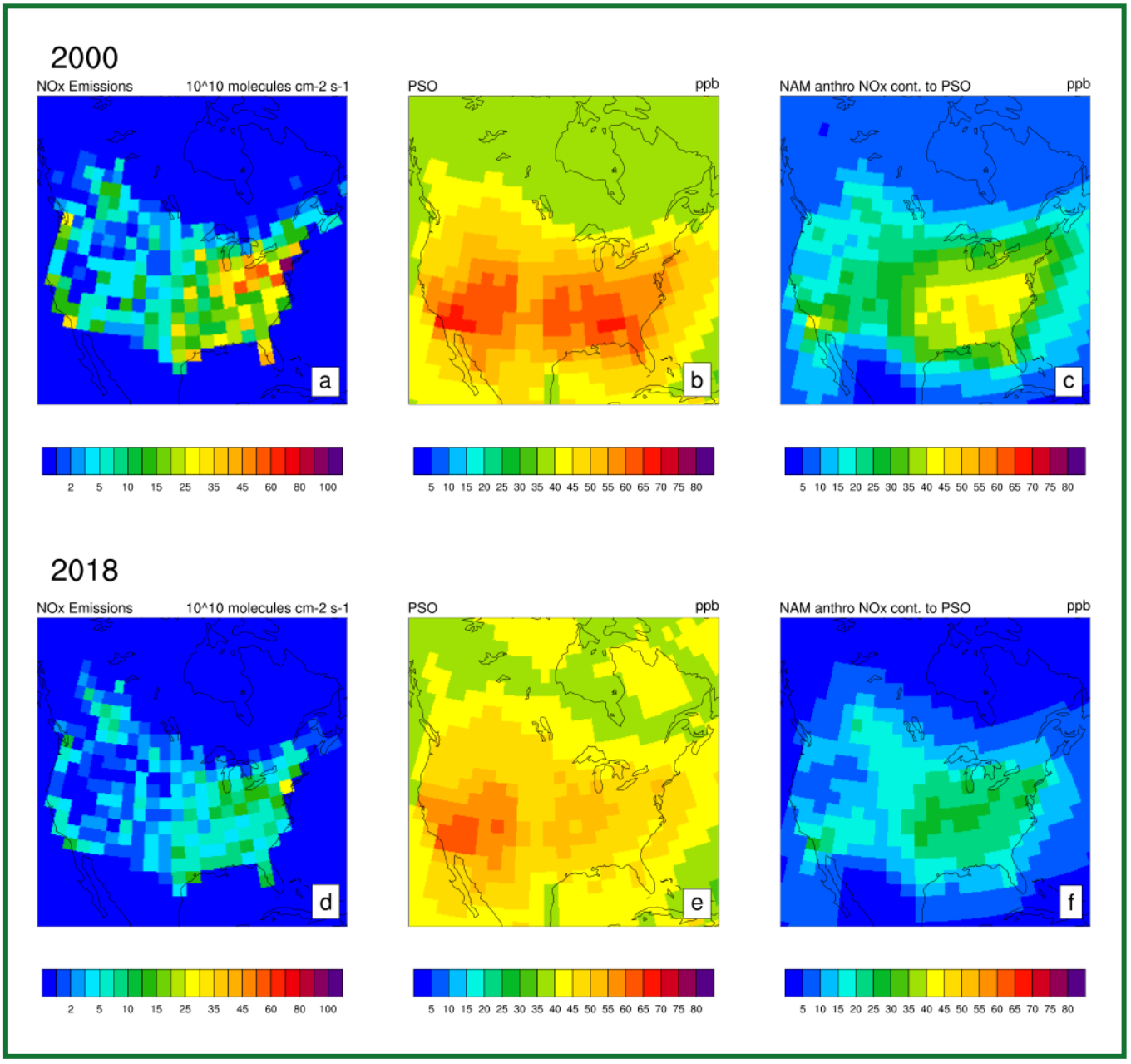

Figure 5: Spatial distribution of local anthropogenic NOx emissions during peak season (a, d), PSO (b, e), and local anthropogenic NOx contribution to PSO (c, f) for North America during the initial (2000) and final year (2018). Here,

emissions for each grid cell were calculated by averaging over a 6-month time window that matches the PSO window over the grid cell.

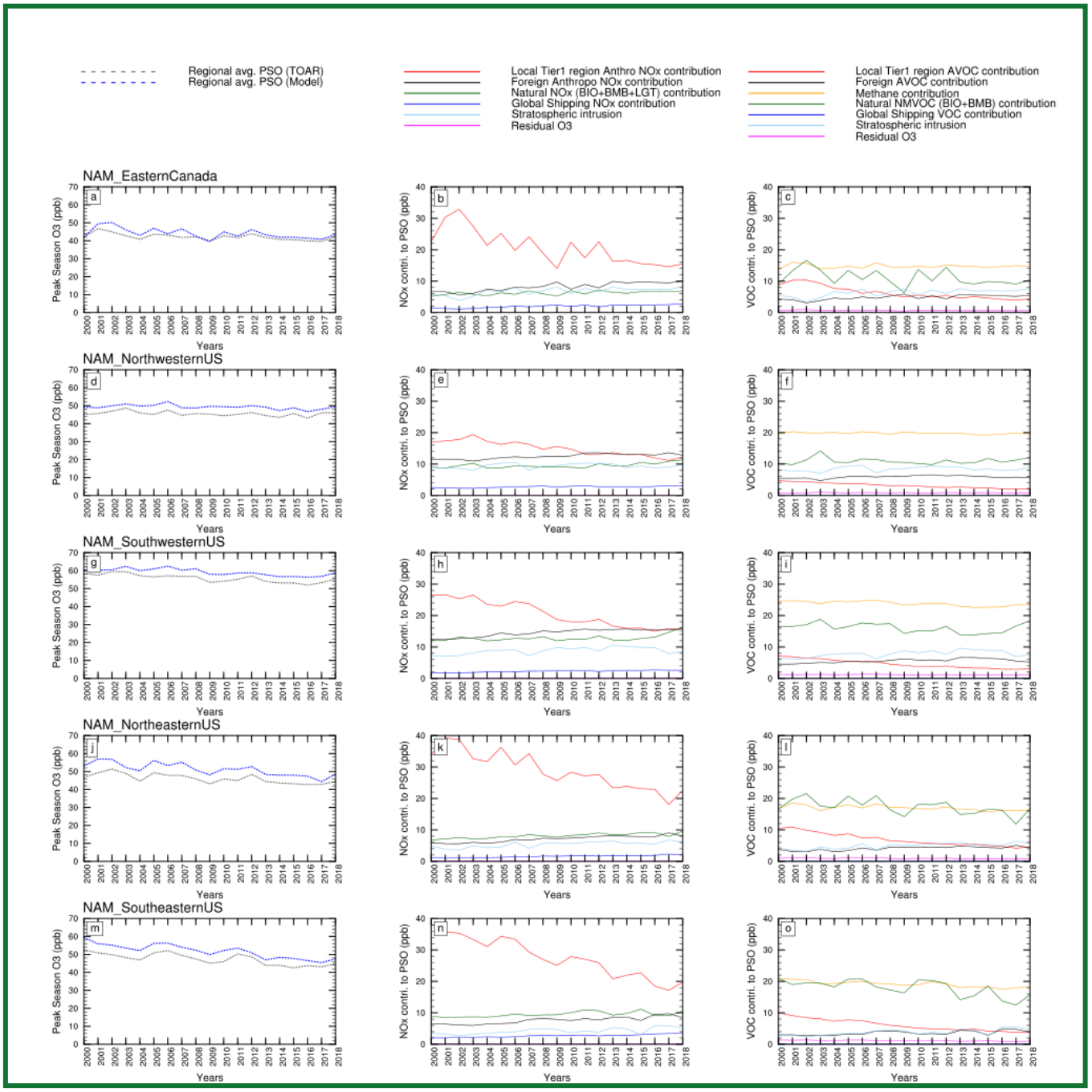
Regional avg. PSO (TOAR)
Regional avg. PSO (Model)
Local Tier1 region Anthro NOx contribution
Foreign Anthropo NOx contribution
Natural NOx (BIO+BMB+LGT) contribution
Global Shipping NOx contribution
Stratospheric intrusion
Residual O3
Local Tier1 region AVOC contribution
Foreign AVOC contribution
Methane contribution
Natural NMVOC (BIO+BMB) contribution
Global Shipping VOC contribution
Stratospheric intrusion
Residual O3
NAM_EasternCanada
NAM_NorthwesternUS
NAM_SouthwesternUS
NAM_NortheasternUS
NAM_SoutheasternUS
Peak Season O3 (ppb)
NOx contri. to PSO (ppb)
VOC contri. to PSO (ppb)
Years

2155

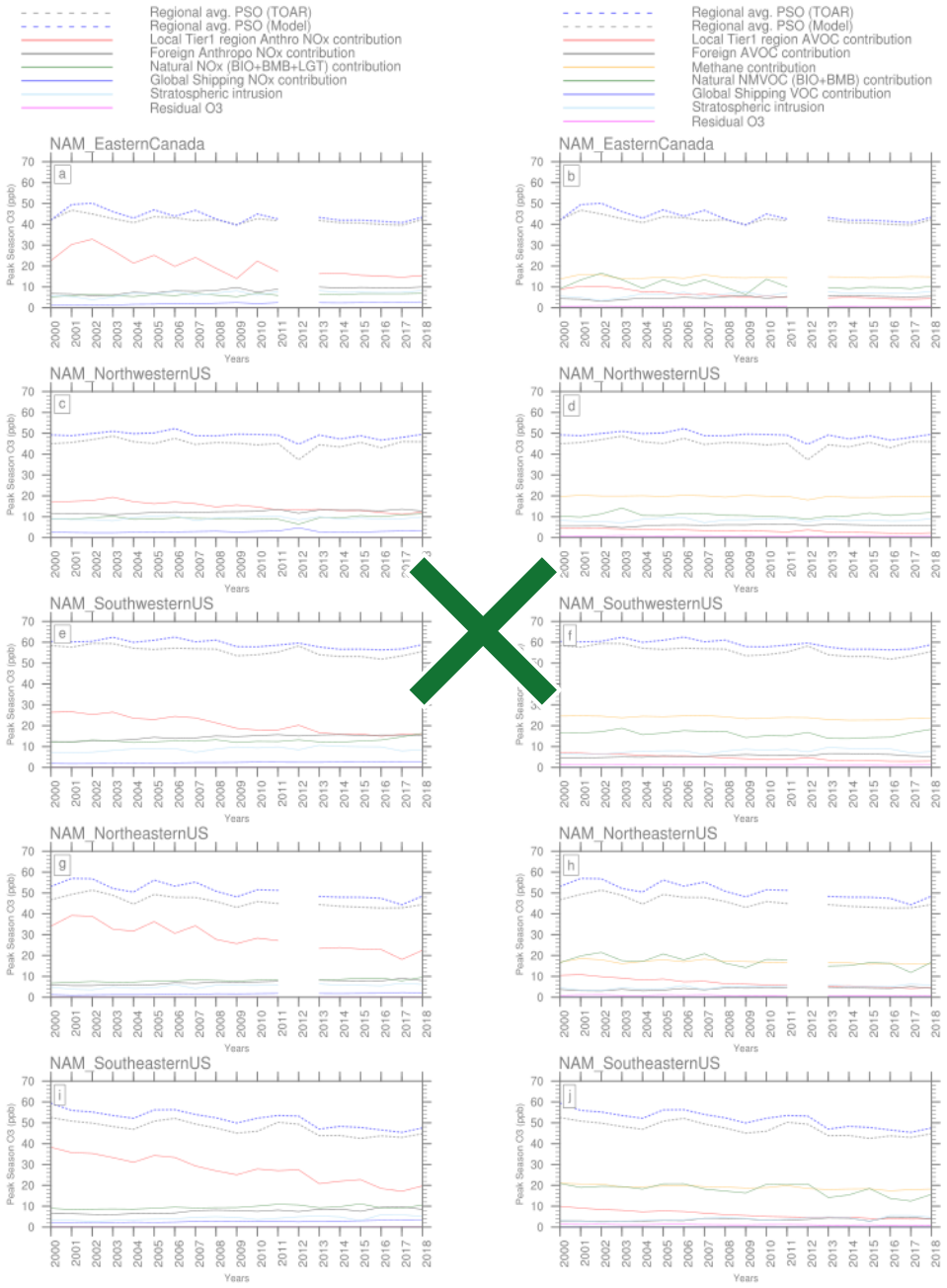

Figure 65: Time-series of observed and model-derived Peak Season Ozone for various receptor regions in North America for 2000-2018 (left panels) and its source contributions in terms of NO_X sources (middle panels~~left~~ panels) and VOC sources (right panels). Model output was sampled from TOAR-valid grid cells only.

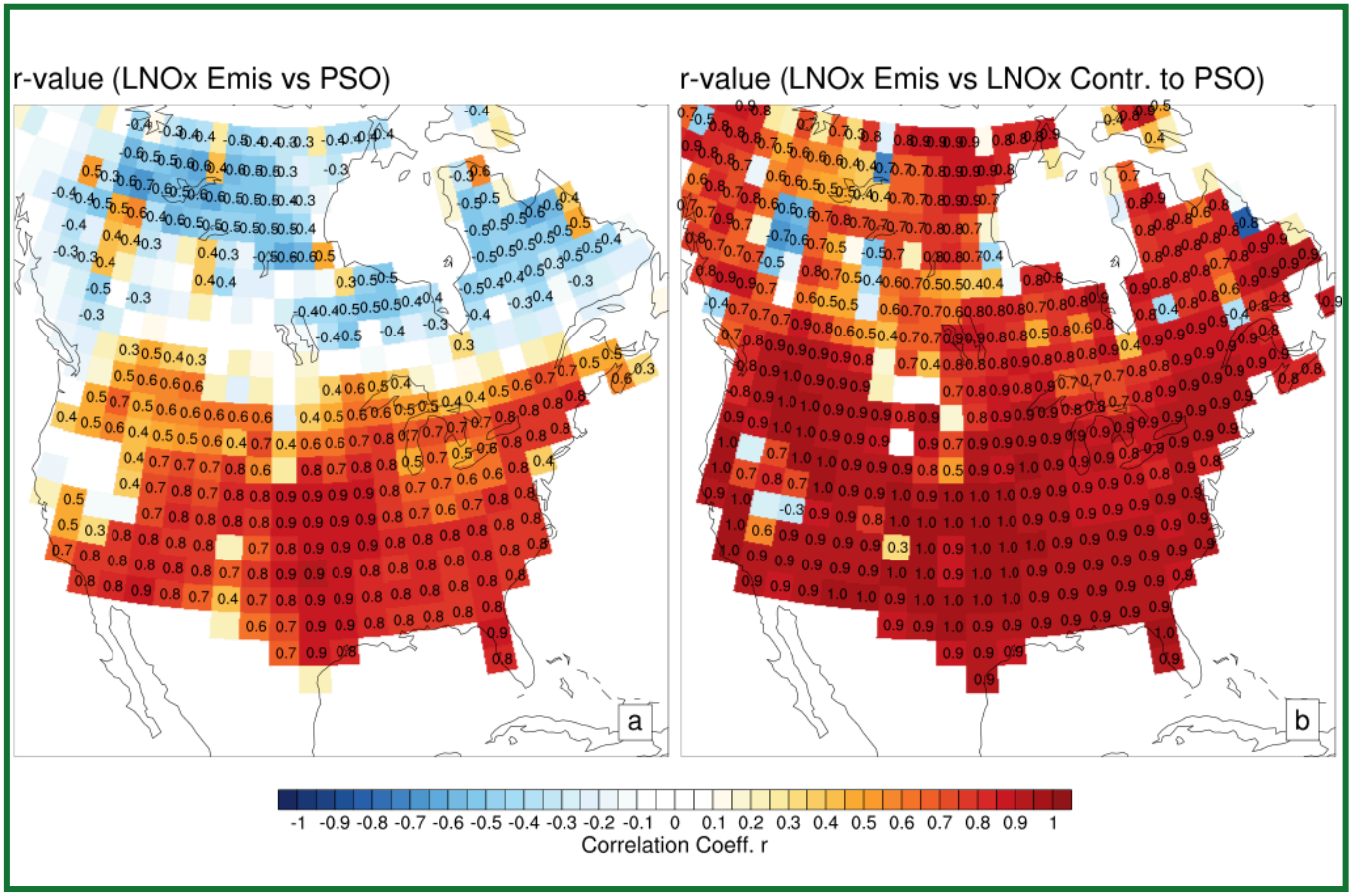
r-value (LNOx Emis vs PSO)
r-value (LNOx Emis vs LNOx Contr. to PSO)
a
b
-1 -0.9 -0.8 -0.7 -0.6 -0.5 -0.4 -0.3 -0.2 -0.1 0 0.1 0.2 0.3 0.4 0.5 0.6 0.7 0.8 0.9 1
Correlation Coeff. r

Figure 7: A spatial map showing correlation coefficient (r) between local (North American) anthropogenic NOx versus PSO (a) and local anthropogenic NOx versus local anthropogenic NOx contribution to PSO (b) over the 19 years for North America. For each year, and each gridcell, only peak season NOx emissions were used.

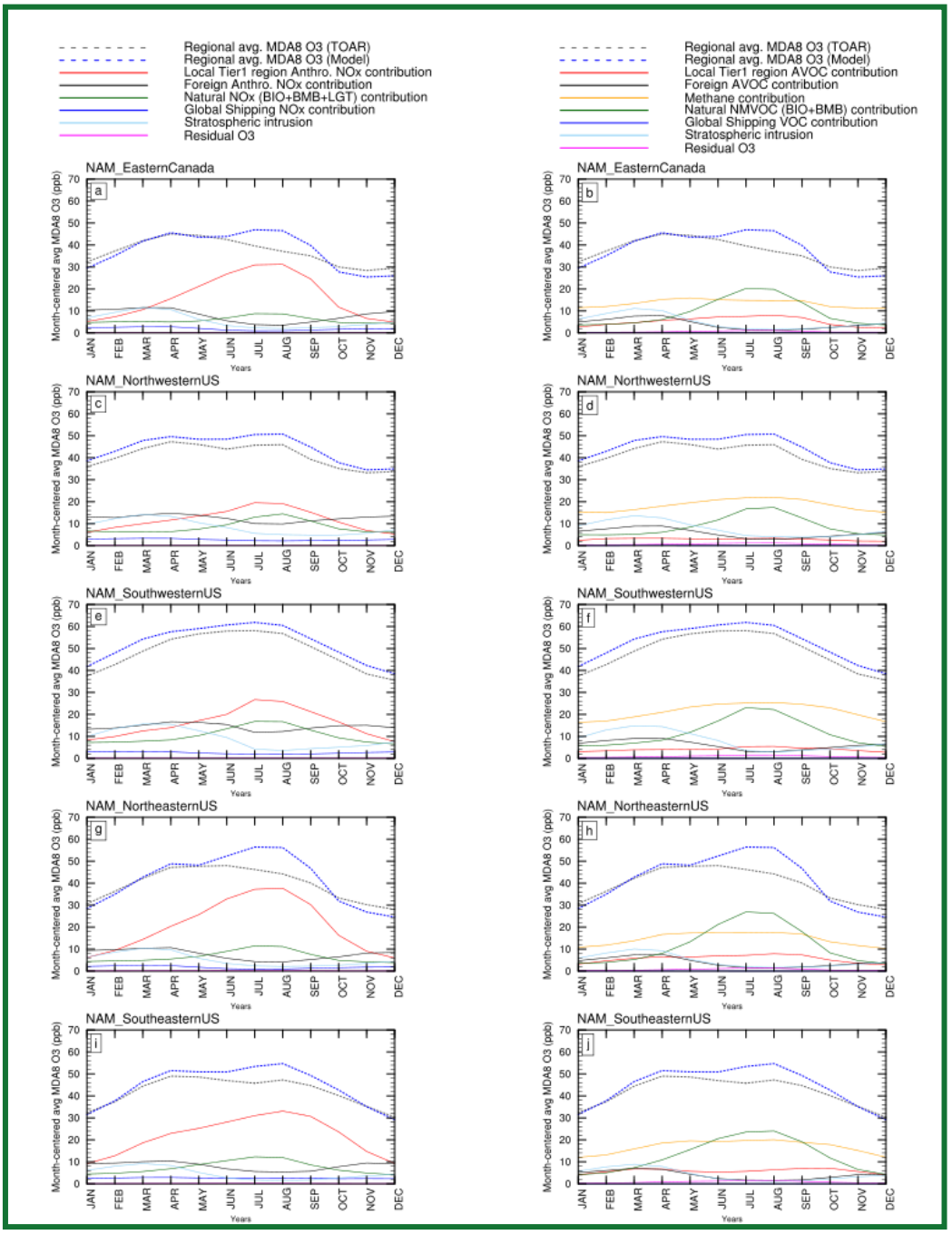
Regional avg. MDA8 O3 (TOAR)
Regional avg. MDA8 O3 (Model)
Local Tier1 region Anthro. NOx contribution
Foreign Anthro. NOx contribution
Natural NOx (BIO+BMB+LGT) contribution
Global Shipping NOx contribution
Stratospheric intrusion
Residual O3
Regional avg. MDA8 O3 (TOAR)
Regional avg. MDA8 O3 (Model)
Local Tier1 region AVOC contribution
Foreign AVOC contribution
Methane contribution
Natural NMVOC (BIO+BMB) contribution
Global Shipping VOC contribution
Stratospheric intrusion
Residual O3
NAM_EasternCanada
NAM_NorthwesternUS
NAM_SouthwesternUS
NAM_NortheasternUS
NAM_SoutheasternUS
Month-centered avg MDA8 O3 (ppb)
Years
JAN FEB MAR APR MAY JUN JUL AUG SEP OCT NOV DEC
a b c d e f g h i j

2171

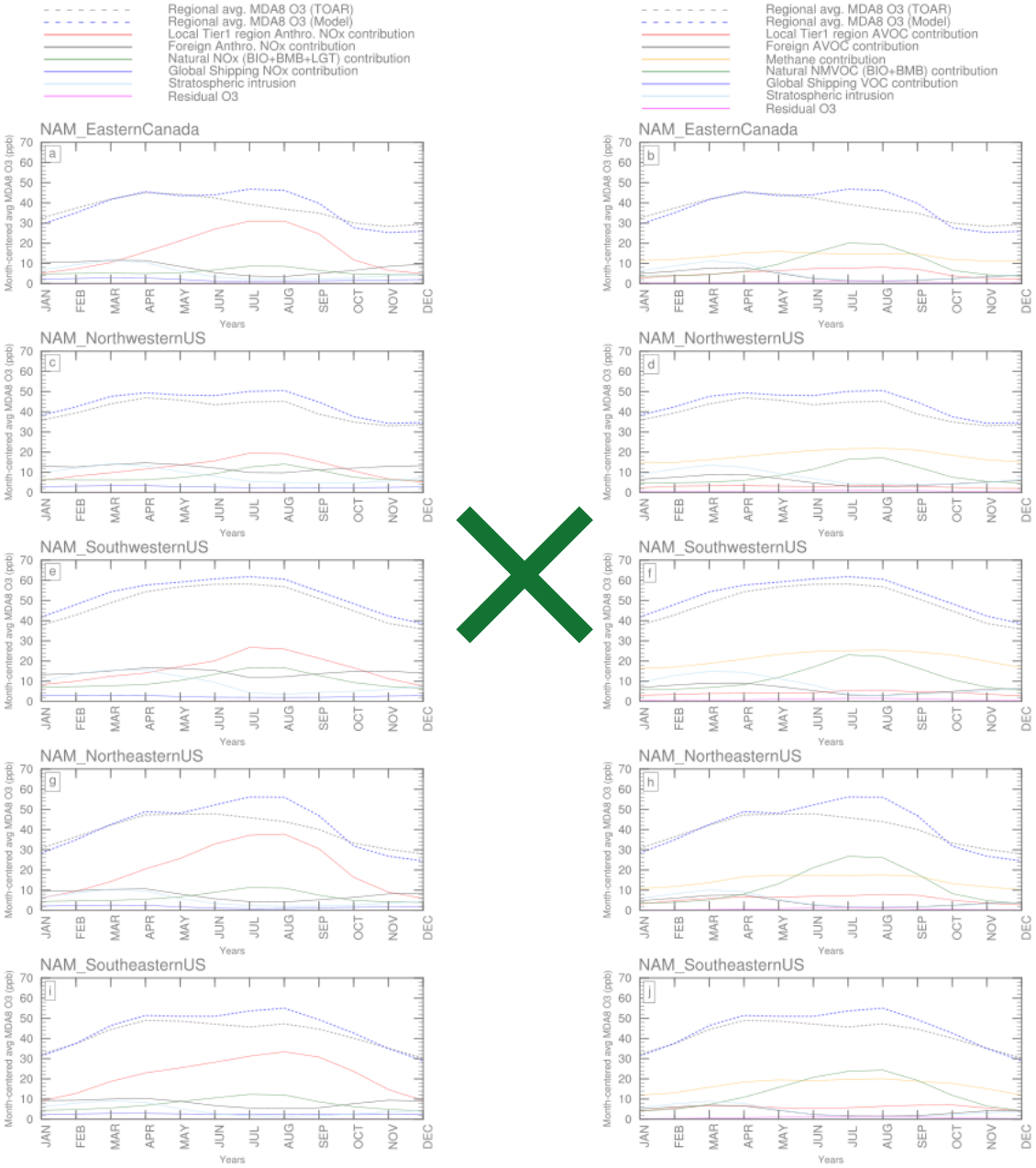

Figure 86: Month-centered average MDA8 O_3 over the 2000-2018 period for various receptor regions in North America and its source contributions in terms of NO_X sources (left panels) and VOC sources (right panels). Model output was sampled from TOAR-valid grid cells only.

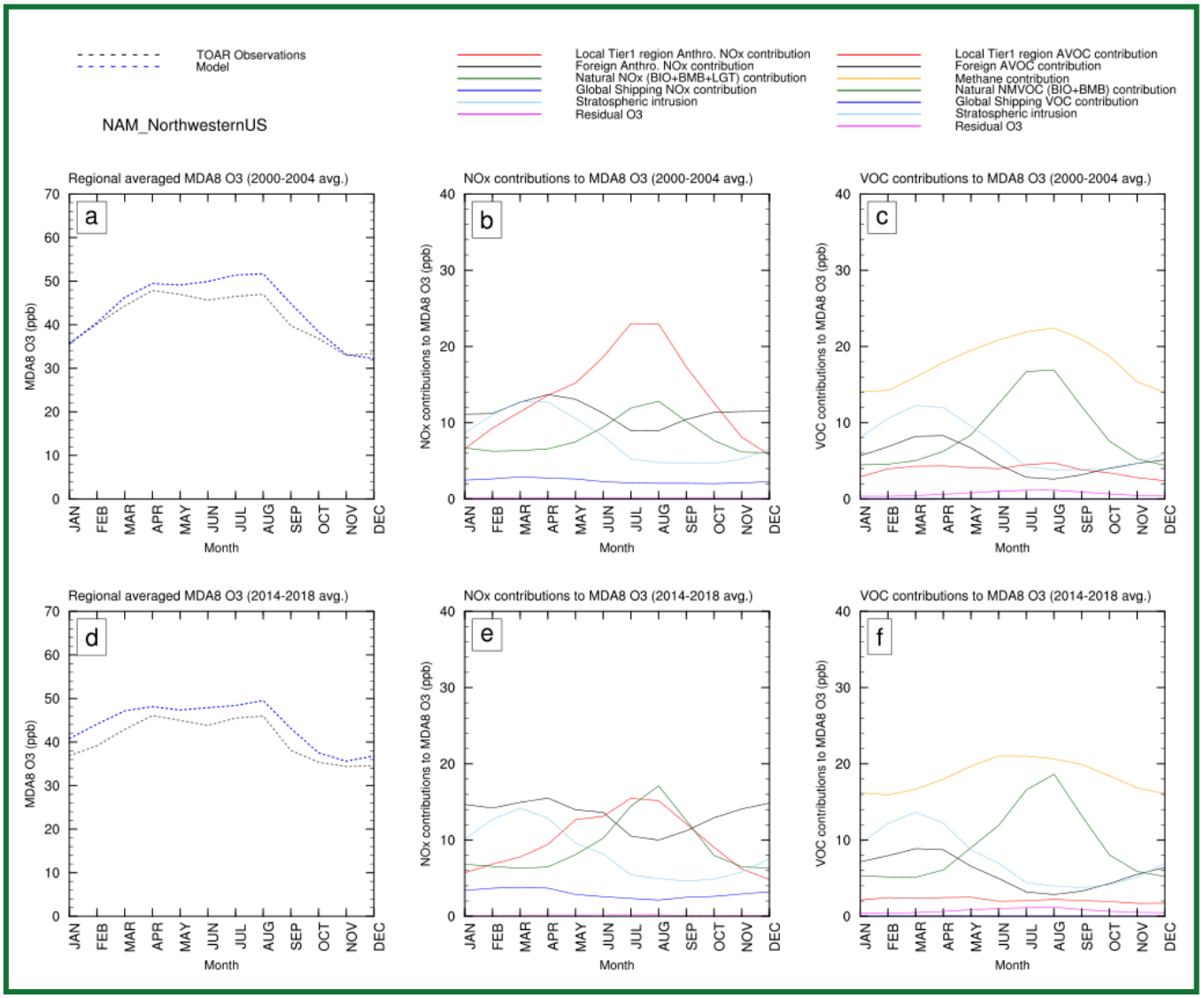
TOAR Observations
Model
NAM_NorthwesternUS
Local Tier1 region Anthro. NOx contribution
Foreign Anthro. NOx contribution
Natural NOx (BIO+BMB+LGT) contribution
Global Shipping NOx contribution
Stratospheric intrusion
Residual O3
Local Tier1 region AVOC contribution
Foreign AVOC contribution
Methane contribution
Natural NMVOC (BIO+BMB) contribution
Global Shipping VOC contribution
Stratospheric intrusion
Residual O3
Regional averaged MDA8 O3 (2000-2004 avg.)
NOx contributions to MDA8 O3 (2000-2004 avg.)
VOC contributions to MDA8 O3 (2000-2004 avg.)
Regional averaged MDA8 O3 (2014-2018 avg.)
NOx contributions to MDA8 O3 (2014-2018 avg.)
VOC contributions to MDA8 O3 (2014-2018 avg.)
a
b
c
d
e
f
MDA8 O3 (ppb)
NOx contributions to MDA8 O3 (ppb)
VOC contributions to MDA8 O3 (ppb)
Month
JAN FEB MAR APR MAY JUN JUL AUG SEP OCT NOV DEC

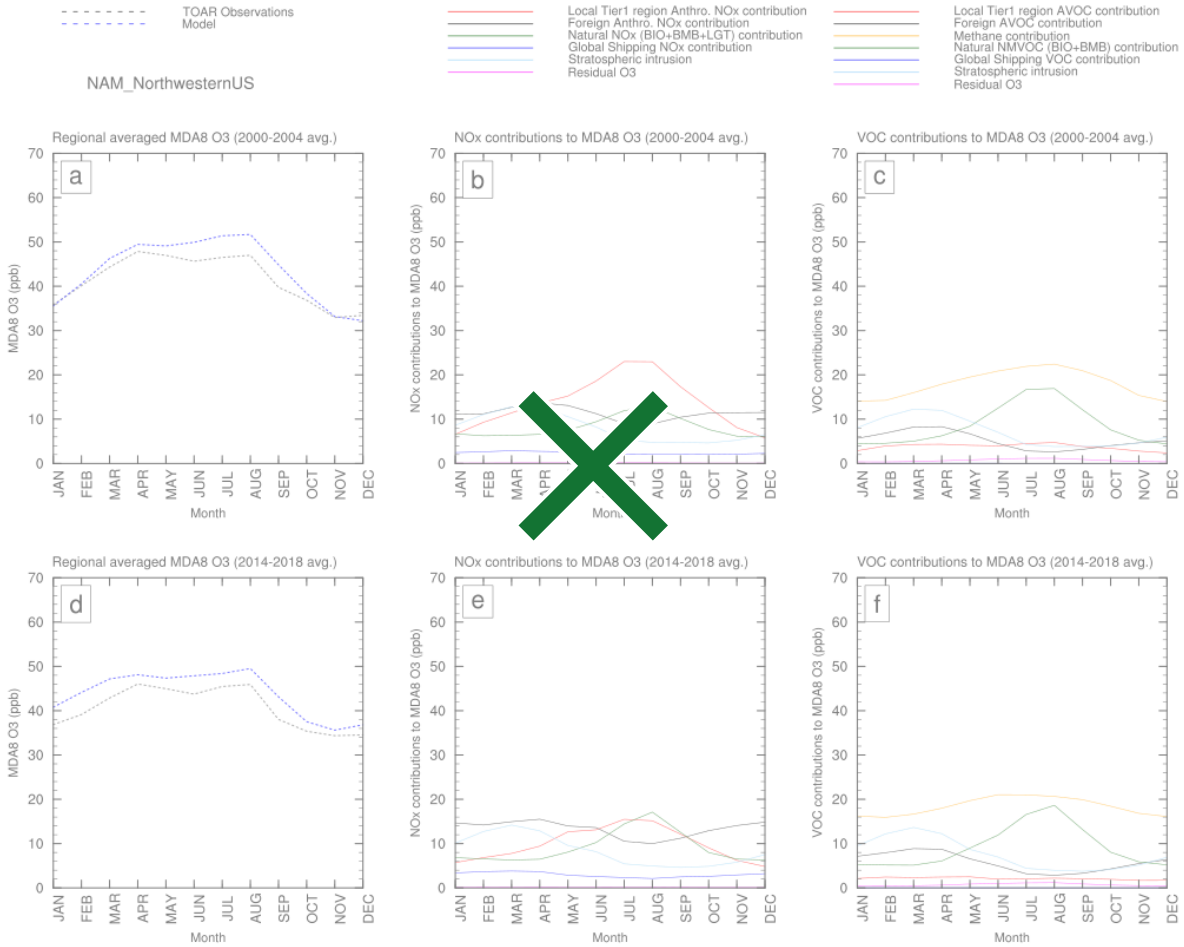

Figure 97: 5-year average MDA8 O_3 seasonal cycles for NW US~~Northwestern US~~ for 2000-2004 (a) and 2014-2018 (b) along with their NO_X (b,e) and VOC contributions (c,f).

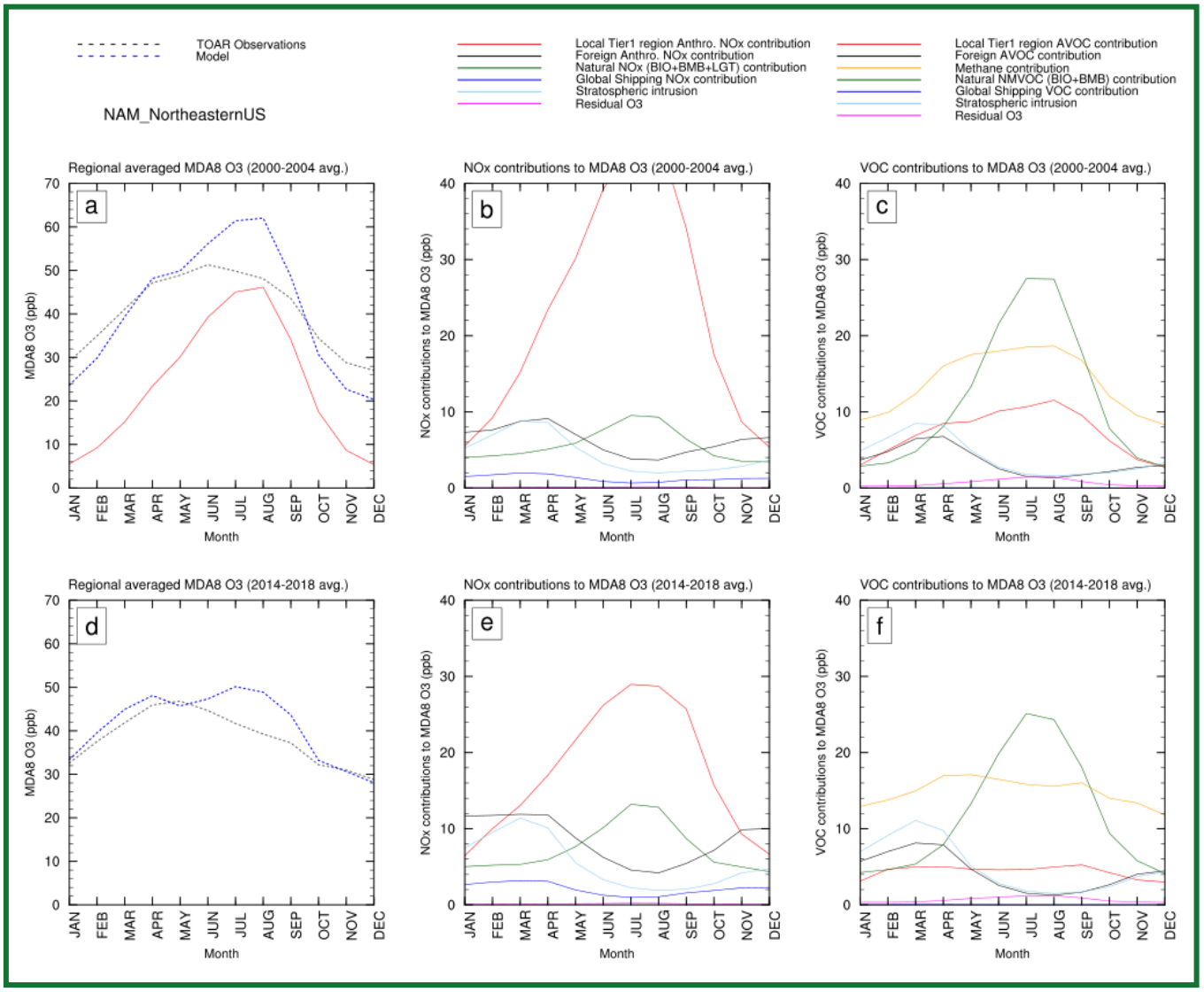
TOAR Observations
Model
NAM_NortheasternUS
Local Tier1 region Anthro. NOx contribution
Foreign Anthro. NOx contribution
Natural NOx (BIO+BMB+LGT) contribution
Global Shipping NOx contribution
Stratospheric intrusion
Residual O3
Local Tier1 region AVOC contribution
Foreign AVOC contribution
Methane contribution
Natural NMVOC (BIO+BMB) contribution
Global Shipping VOC contribution
Stratospheric intrusion
Residual O3
Regional averaged MDA8 O3 (2000-2004 avg.)
NOx contributions to MDA8 O3 (2000-2004 avg.)
VOC contributions to MDA8 O3 (2000-2004 avg.)
Regional averaged MDA8 O3 (2014-2018 avg.)
NOx contributions to MDA8 O3 (2014-2018 avg.)
VOC contributions to MDA8 O3 (2014-2018 avg.)
a
b
c
d
e
f
MDA8 O3 (ppb)
NOx contributions to MDA8 O3 (ppb)
VOC contributions to MDA8 O3 (ppb)
Month
JAN FEB MAR APR MAY JUN JUL AUG SEP OCT NOV DEC

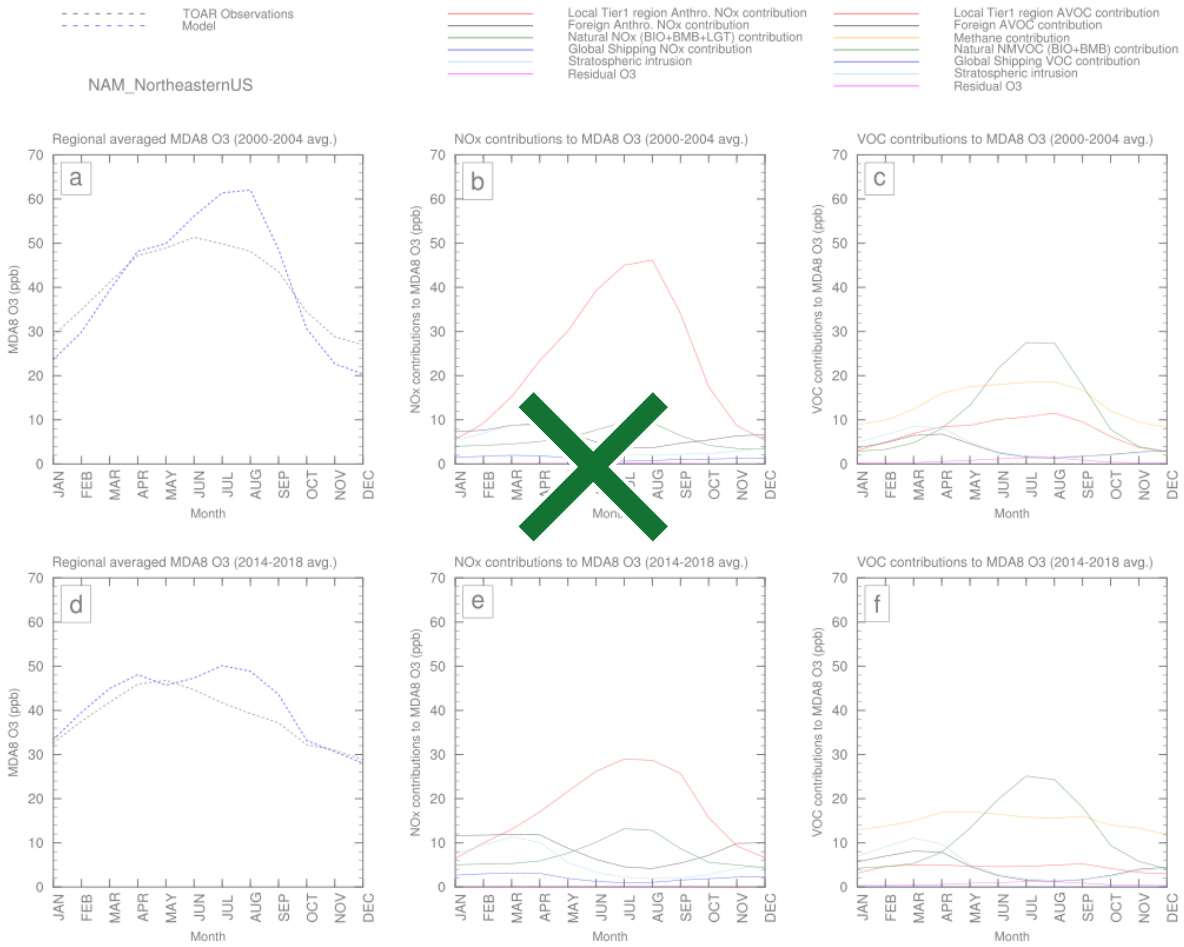

Figure 108: 5-year average MDA8 O_3 seasonal cycles for NE US~~Northeastern US~~ for 2000-2004 (a) and 2014-2018 (b) along with their NO_X (b,e) and VOC contributions (c,f).

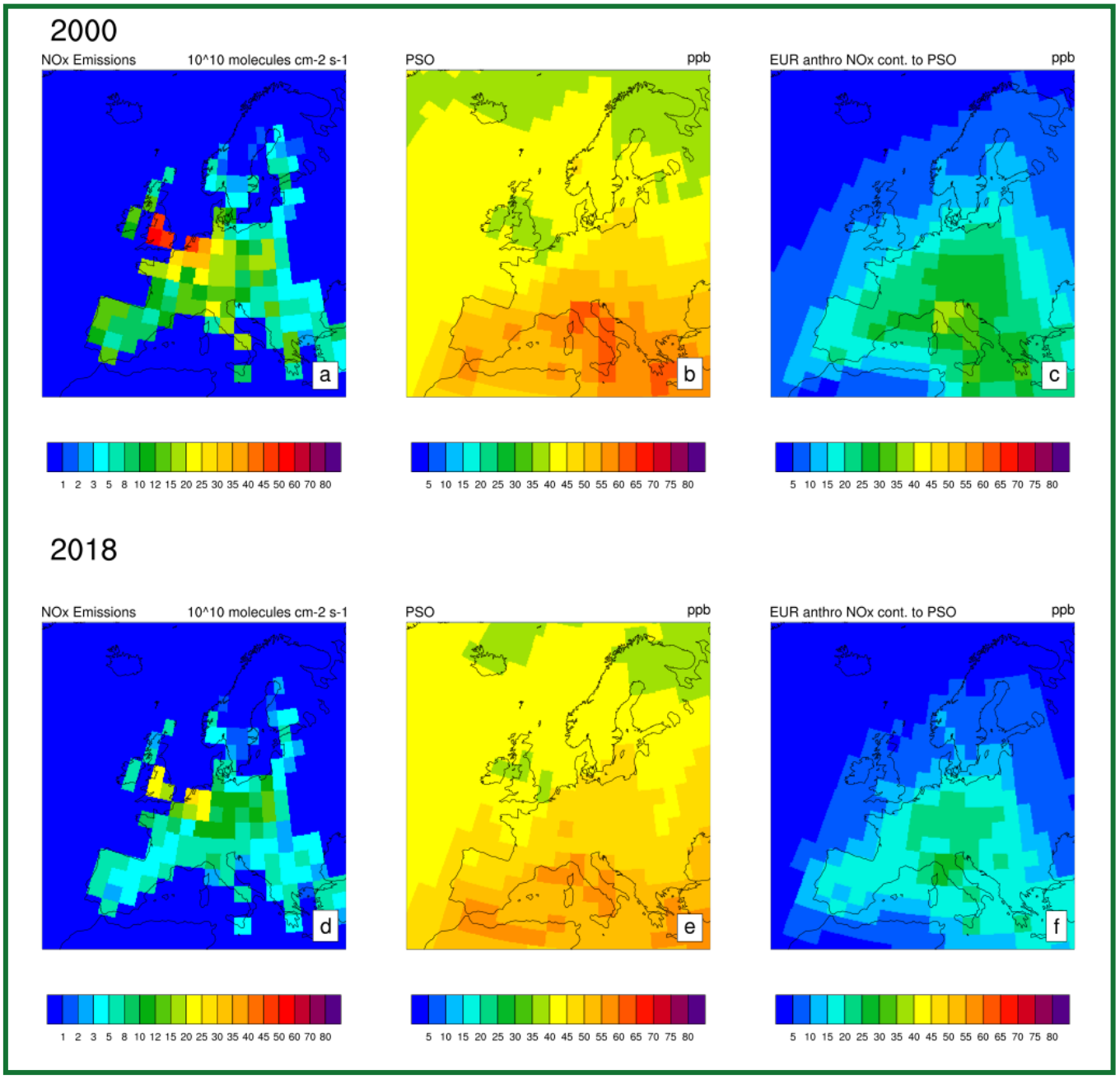
2000
NOx Emissions
10^10 molecules cm-2 s-1
PSO
ppb
EUR anthro NOx cont. to PSO
ppb
a
b
c
1 2 3 5 8 10 12 15 20 25 30 35 40 45 50 60 70 80
5 10 15 20 25 30 35 40 45 50 55 60 65 70 75 80
5 10 15 20 25 30 35 40 45 50 55 60 65 70 75 80
2018
NOx Emissions
10^10 molecules cm-2 s-1
PSO
ppb
EUR anthro NOx cont. to PSO
ppb
d
e
f
1 2 3 5 8 10 12 15 20 25 30 35 40 45 50 60 70 80
5 10 15 20 25 30 35 40 45 50 55 60 65 70 75 80
5 10 15 20 25 30 35 40 45 50 55 60 65 70 75 80

Figure 11: Spatial distribution of local anthropogenic NOx emissions during peak season (a, d), PSO (b, e), and local anthropogenic NOx contribution to PSO (c, f) for Europe during the initial (2000) and final year (2018). Here, emissions for each grid cell were calculated by averaging over a 6-month time window that matches the PSO window over the grid cell.

¶

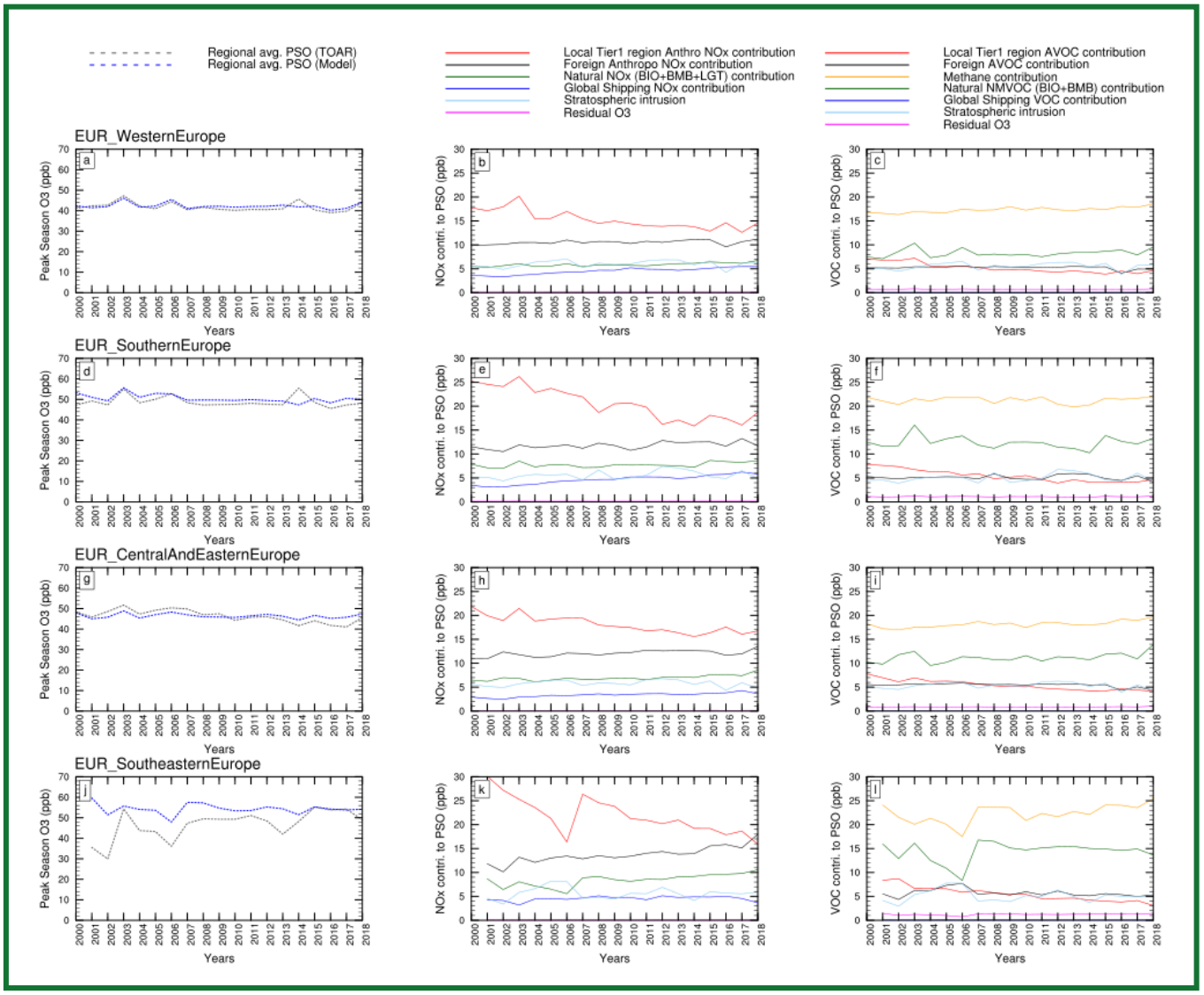
Regional avg. PSO (TOAR)
Regional avg. PSO (Model)
Local Tier1 region Anthro NOx contribution
Foreign Anthropo NOx contribution
Natural NOx (BIO+BMB+LGT) contribution
Global Shipping NOx contribution
Stratospheric intrusion
Residual O3
Local Tier1 region AVOC contribution
Foreign AVOC contribution
Methane contribution
Natural NMVOC (BIO+BMB) contribution
Global Shipping VOC contribution
Stratospheric intrusion
Residual O3
EUR_WesternEurope
EUR_SouthernEurope
EUR_CentralAndEasternEurope
EUR_SoutheasternEurope
Peak Season O3 (ppb)
NOx contri. to PSO (ppb)
VOC contri. to PSO (ppb)
Years

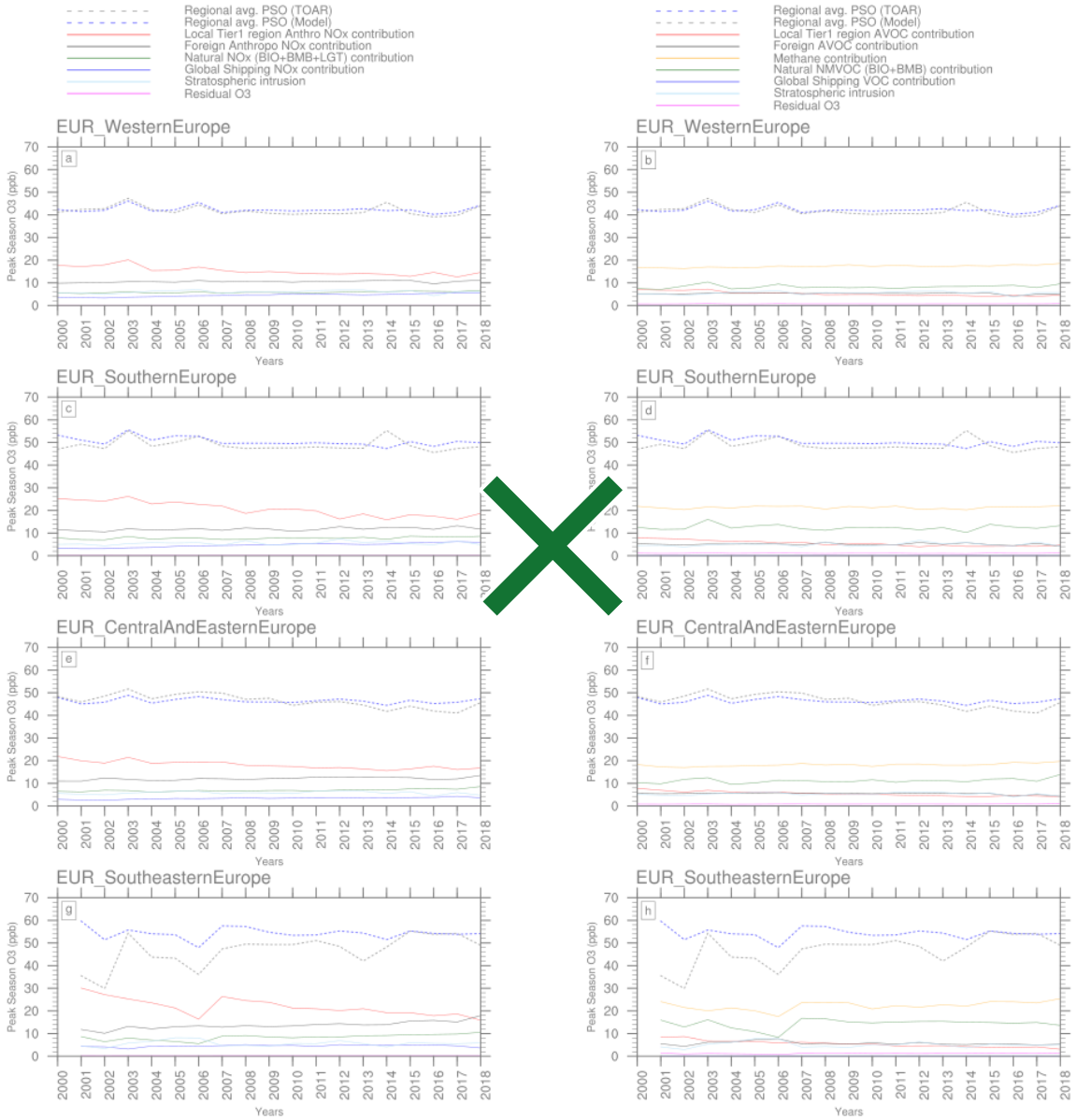

Figure 129: Time-series of observed and model-derived Peak Season Ozone for various receptor regions in Europe for 2000-2018 (left panels) and its source contributions in terms of NO_X sources (middle~~left~~ panels) and VOC sources (right panels). Model output was sampled from TOAR-valid grid cells only.

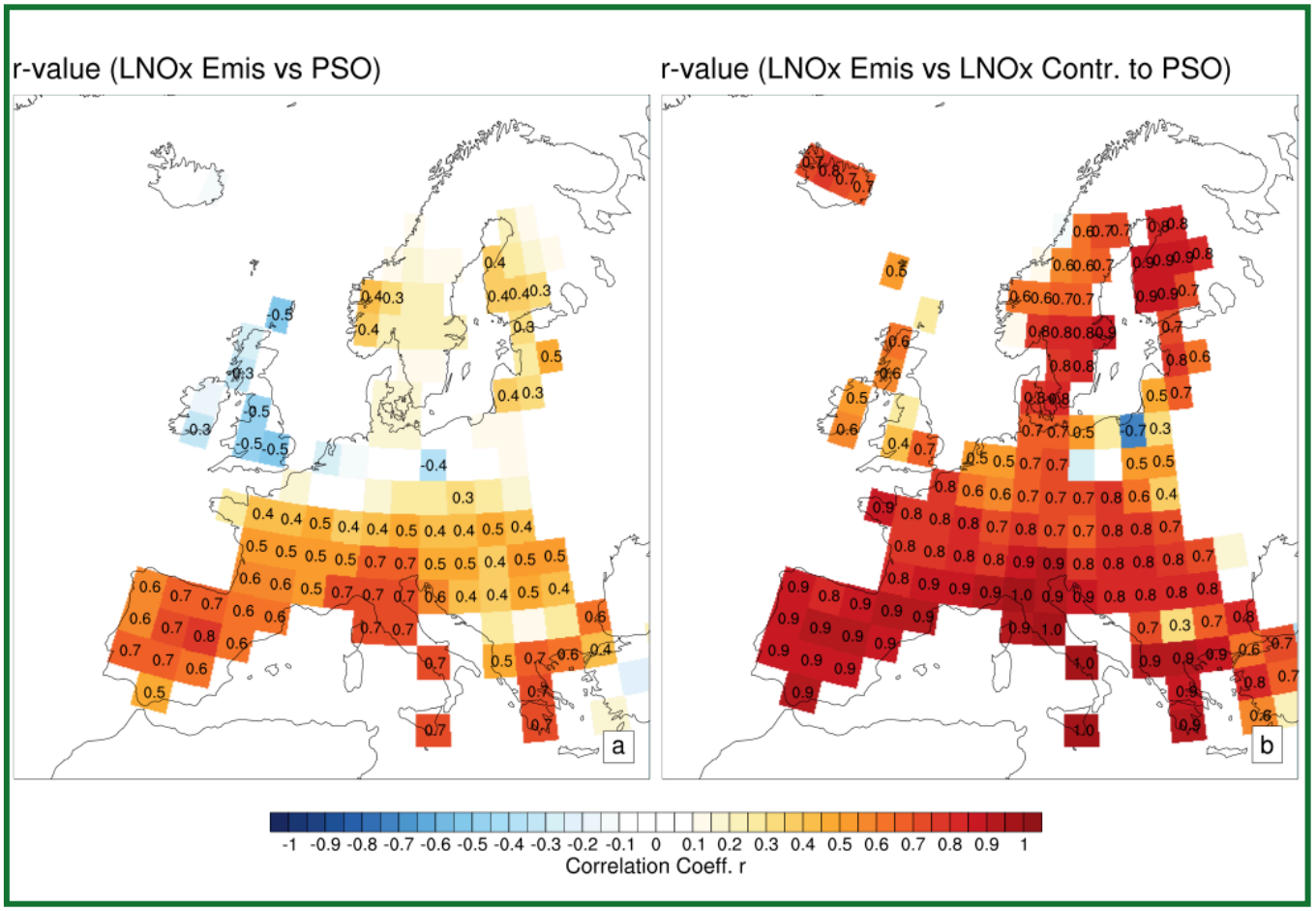

Figure 13: A spatial map showing correlation coefficient (r) between local anthropogenic NOx versus PSO (a) and local anthropogenic NOx versus local anthropogenic NOx contribution to PSO (b) over the 19 years for Europe. For each year, and each gridcell, only peak season NOx emissions were used per grid cell.

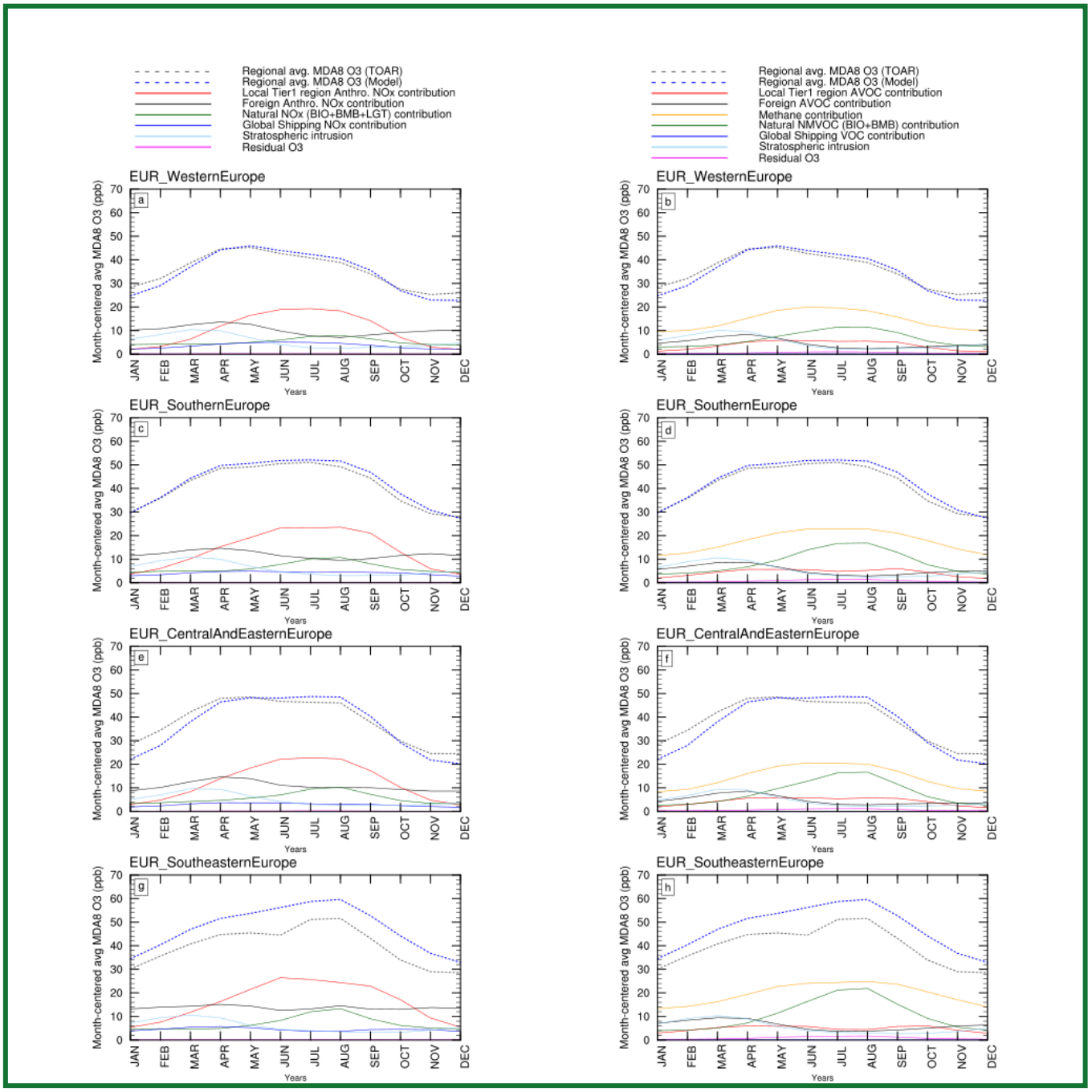
Regional avg. MDA8 O3 (TOAR)
Regional avg. MDA8 O3 (Model)
Local Tier1 region Anthro. NOx contribution
Foreign Anthro. NOx contribution
Natural NOx (BIO+BMB+LGT) contribution
Global Shipping NOx contribution
Stratospheric intrusion
Residual O3
Regional avg. MDA8 O3 (TOAR)
Regional avg. MDA8 O3 (Model)
Local Tier1 region AVOC contribution
Foreign AVOC contribution
Methane contribution
Natural NMVOC (BIO+BMB) contribution
Global Shipping VOC contribution
Stratospheric intrusion
Residual O3
EUR_WesternEurope
EUR_SouthernEurope
EUR_CentralAndEasternEurope
EUR_SoutheasternEurope
a
b
c
d
e
f
g
h
Month-centered avg MDA8 O3 (ppb)
0
10
20
30
40
50
60
70
JAN
FEB
MAR
APR
MAY
JUN
JUL
AUG
SEP
OCT
NOV
DEC
Years

2227

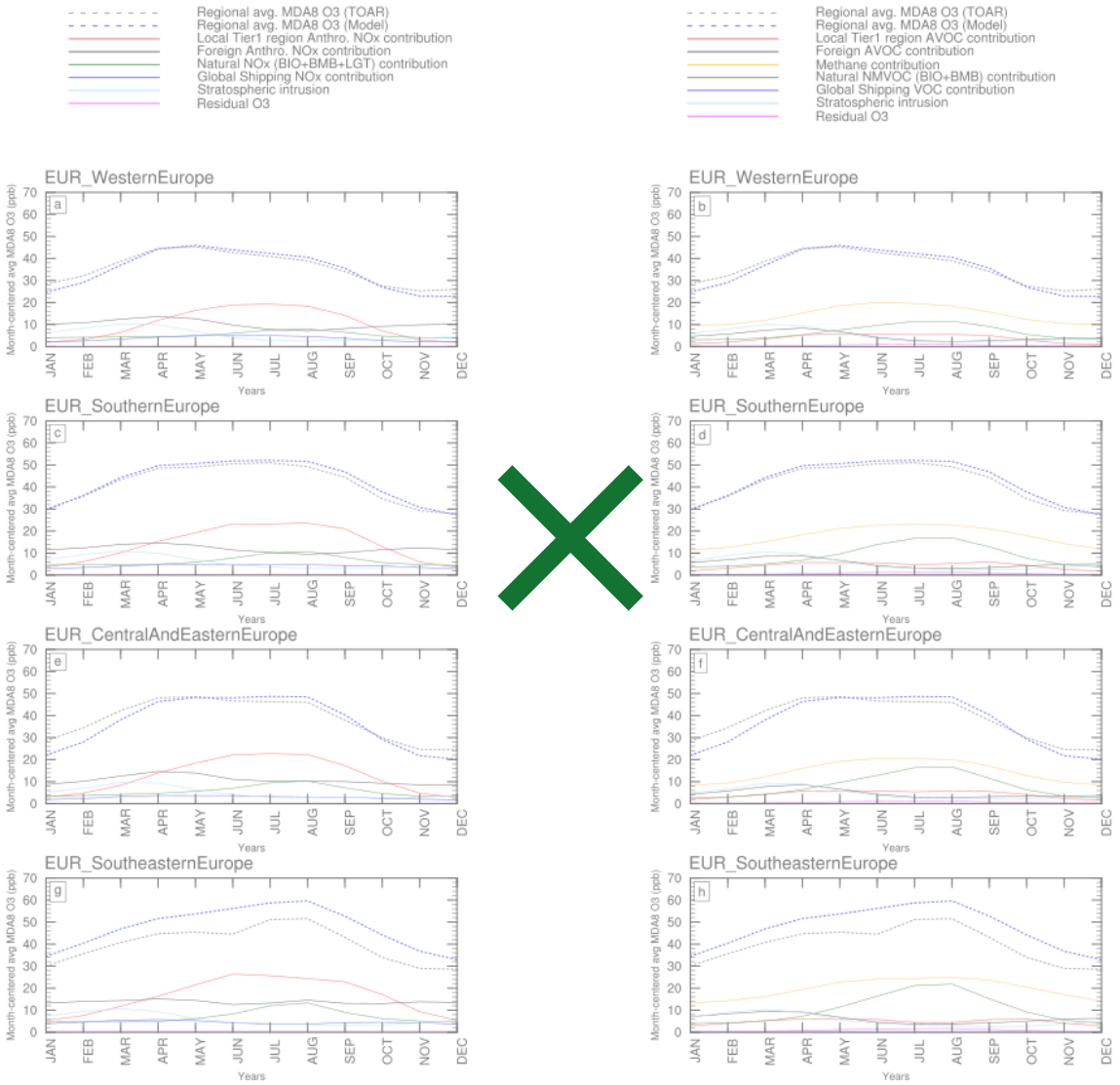

Figure 140: Month-centered average MDA8 O_3 over the 2000-2018 period for various receptor regions in Europe and its source contributions in terms of NO_X sources (left panels) and VOC sources (right panels). Model output was sampled from TOAR-valid grid cells only.

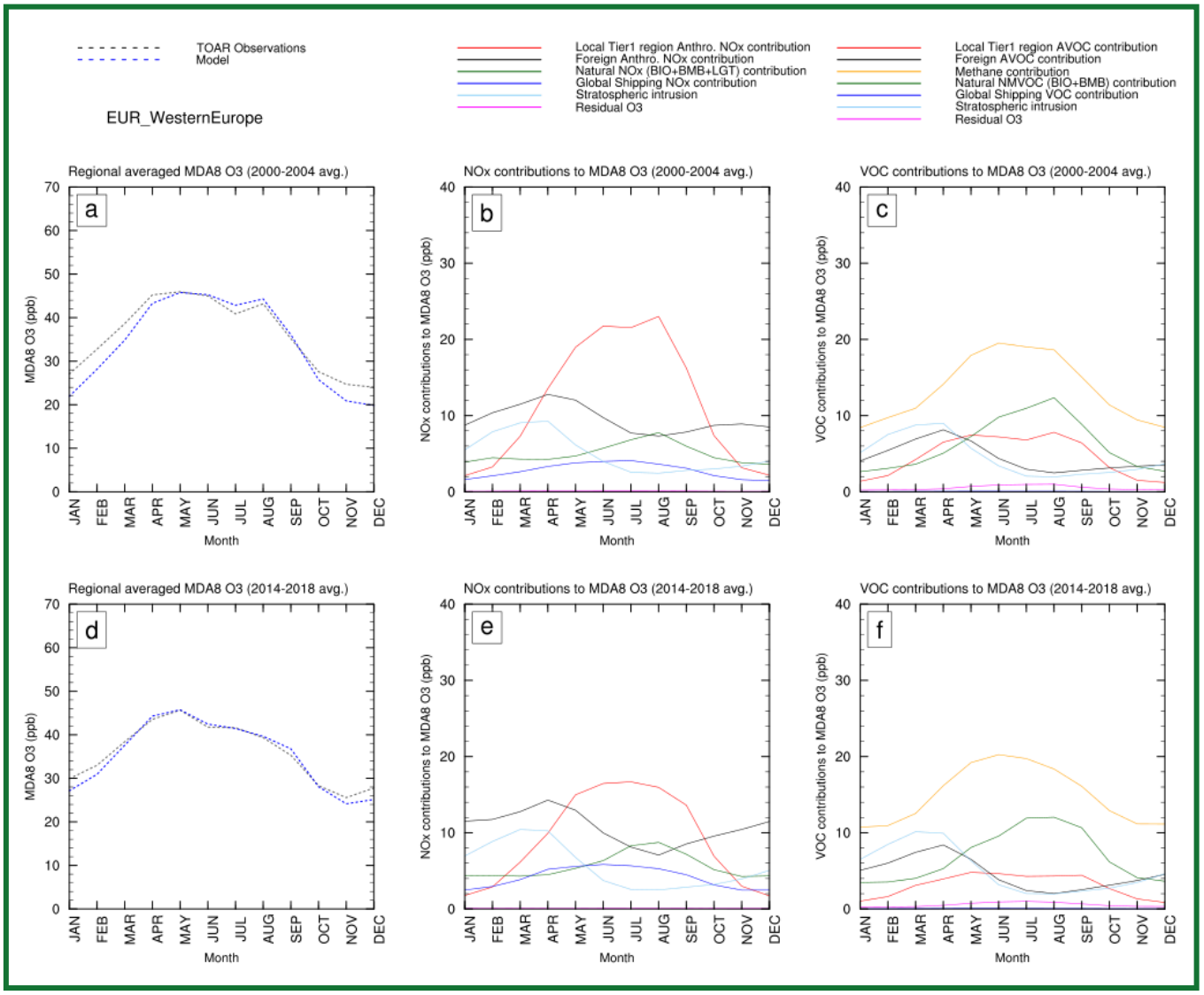
TOAR Observations
Model
EUR_WesternEurope
Local Tier1 region Anthro. NOx contribution
Foreign Anthro. NOx contribution
Natural NOx (BIO+BMB+LGT) contribution
Global Shipping NOx contribution
Stratospheric intrusion
Residual O3
Local Tier1 region AVOC contribution
Foreign AVOC contribution
Methane contribution
Natural NMVOC (BIO+BMB) contribution
Global Shipping VOC contribution
Stratospheric intrusion
Residual O3
Regional averaged MDA8 O3 (2000-2004 avg.)
NOx contributions to MDA8 O3 (2000-2004 avg.)
VOC contributions to MDA8 O3 (2000-2004 avg.)
Regional averaged MDA8 O3 (2014-2018 avg.)
NOx contributions to MDA8 O3 (2014-2018 avg.)
VOC contributions to MDA8 O3 (2014-2018 avg.)
a
b
c
d
e
f
MDA8 O3 (ppb)
NOx contributions to MDA8 O3 (ppb)
VOC contributions to MDA8 O3 (ppb)
Month
JAN FEB MAR APR MAY JUN JUL AUG SEP OCT NOV DEC

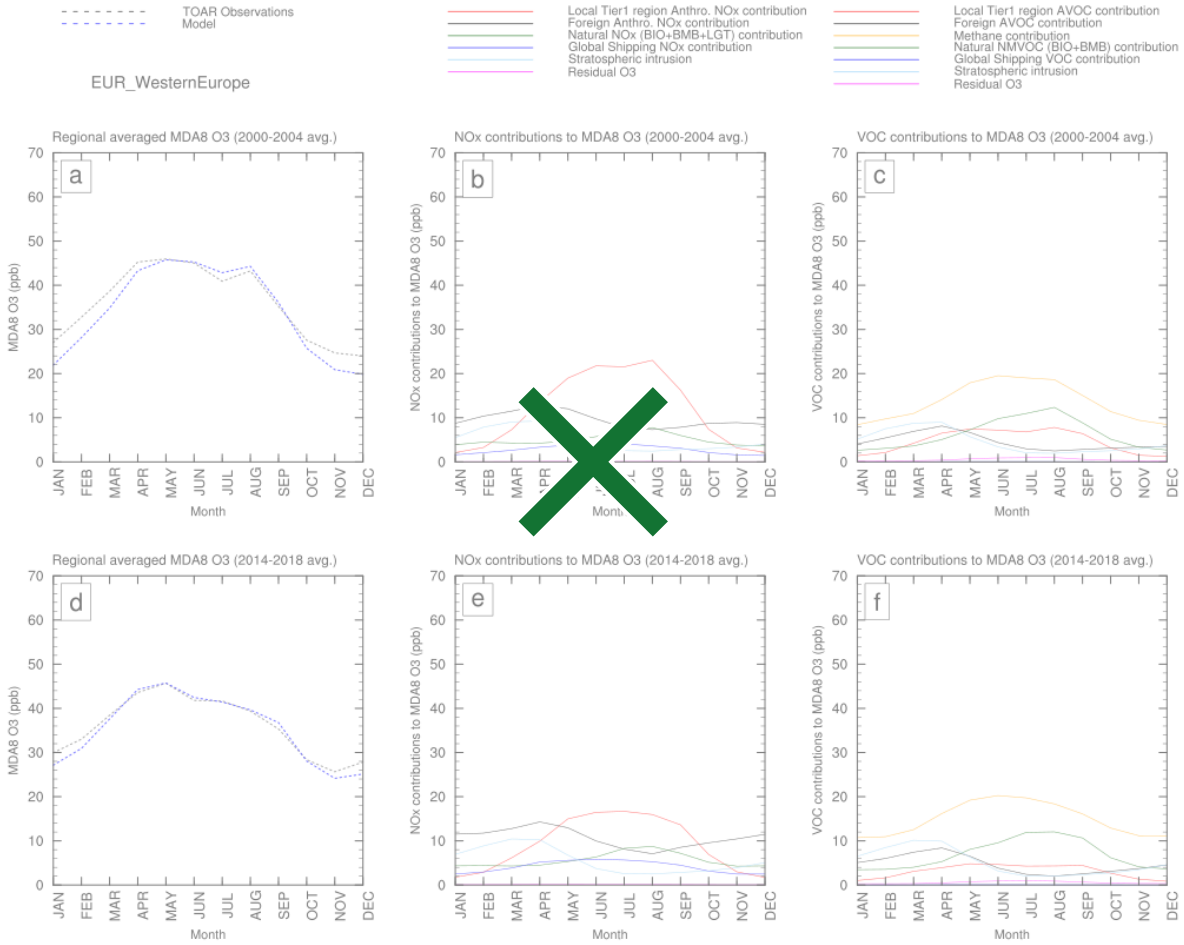

Figure 15: 5-year average MDA8 O_3 seasonal cycles for Western Europe for 2000-2004 (a) and 2014-2018 (b) along with their NO_X (b,e) and VOC contributions (c,f).

2248

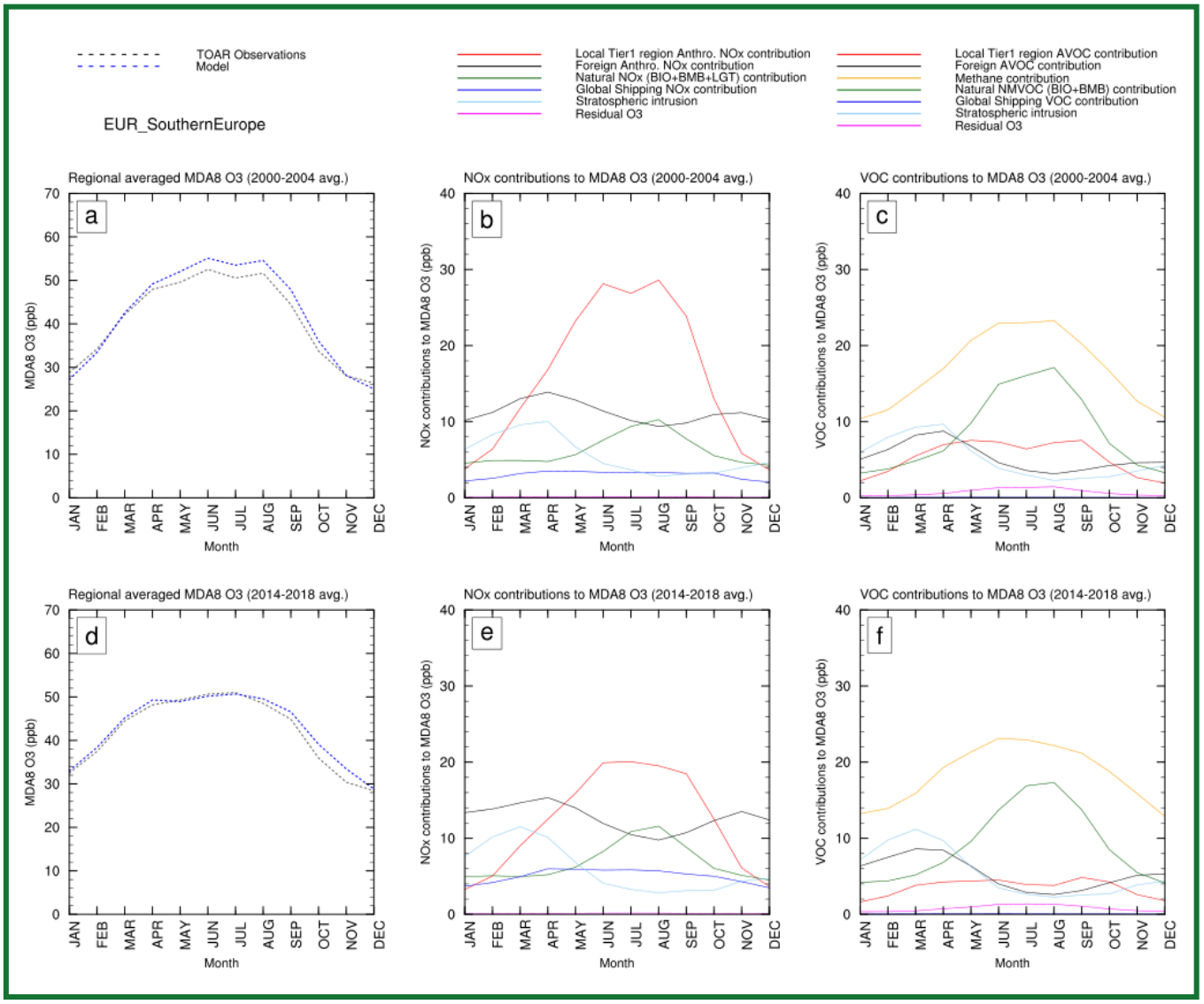
TOAR Observations
Model
EUR_SouthernEurope
Local Tier1 region Anthro. NOx contribution
Foreign Anthro. NOx contribution
Natural NOx (BIO+BMB+LGT) contribution
Global Shipping NOx contribution
Stratospheric intrusion
Residual O3
Local Tier1 region AVOC contribution
Foreign AVOC contribution
Methane contribution
Natural NMVOC (BIO+BMB) contribution
Global Shipping VOC contribution
Stratospheric intrusion
Residual O3
Regional averaged MDA8 O3 (2000-2004 avg.)
NOx contributions to MDA8 O3 (2000-2004 avg.)
VOC contributions to MDA8 O3 (2000-2004 avg.)
Regional averaged MDA8 O3 (2014-2018 avg.)
NOx contributions to MDA8 O3 (2014-2018 avg.)
VOC contributions to MDA8 O3 (2014-2018 avg.)
a
b
c
d
e
f
MDA8 O3 (ppb)
NOx contributions to MDA8 O3 (ppb)
VOC contributions to MDA8 O3 (ppb)
Month
JAN FEB MAR APR MAY JUN JUL AUG SEP OCT NOV DEC

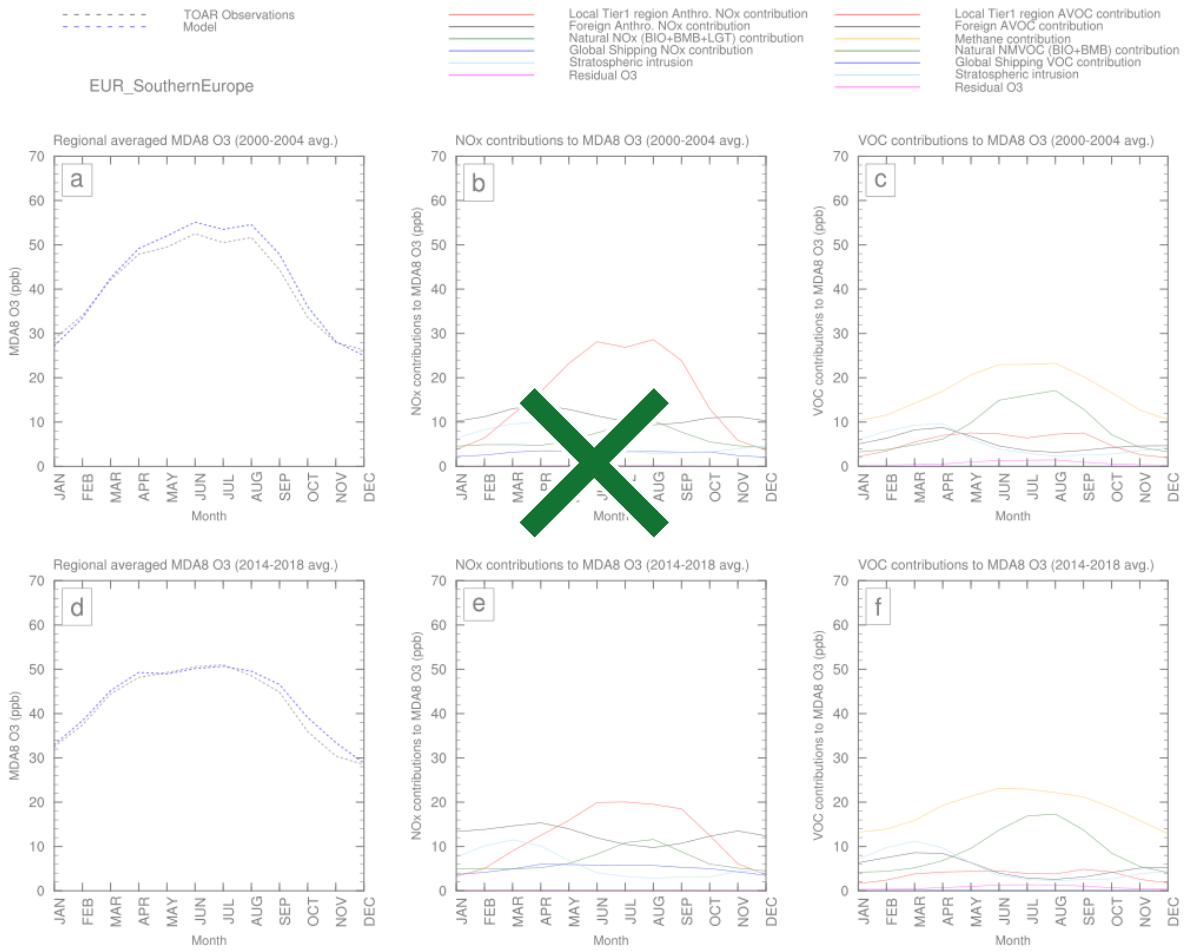

Figure 162: 5-year average MDA8 O_3 seasonal cycles for Southern Europe for 2000-2004 (a) and 2014-2018 (b) along with their NO_X (b,e) and VOC contributions (c,f).

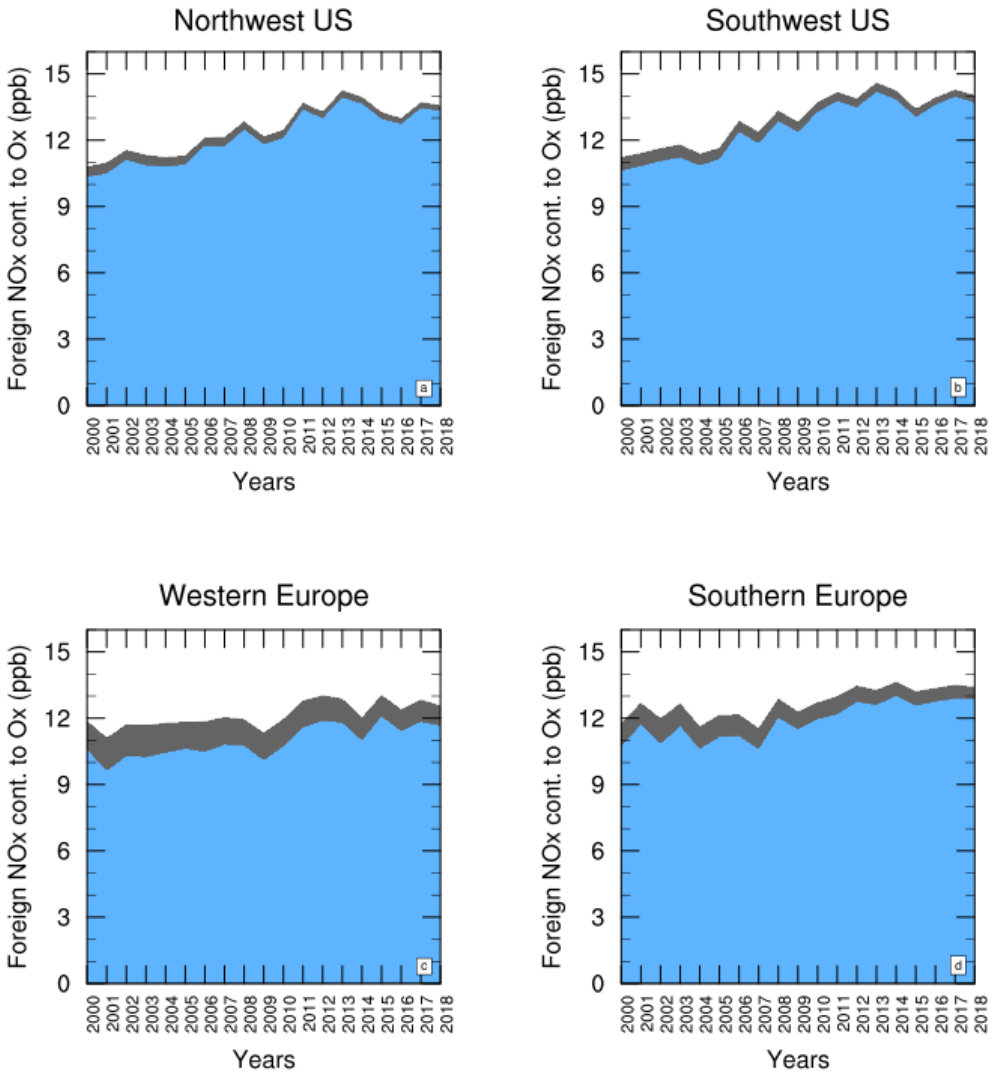

Figure 17: Time series of Foreign OX (O3+NO2) contributions to wintertime and springtime (Jan-Apr) mean ozone in North American and European receptor regions. The blue shaded area denotes O3 due to foreign anthropogenic NOx and the grey shaded area denotes NO2 originating from the titration of O3 that is attributed to foreign anthropogenic NOx.

Table 1: Various emission tags for NO_X- and VOC-tagged simulations. The geographic definition of the land-based tags corresponds to the HTAP tier 1 regions as shown in Figure 1. For NO_X-tagging, "Rest of the World" corresponds to the tier 1 regions of South America, Oceania, and Middle & Southern Africa combined. For VOC-tagging, the regions: Arctic, Central Asia, Mexico & Central America, North Africa, and Southeast Asia were also combined into the "Rest of the World". The regional oceanic tags are only applicable for NO_X-tagging and their geographic definitions are shown in Figure S12. For VOC-tagging we use a single oceanic tag representing NMVOCs from shipping and natural DMS emissions. Lightning tag is only applicable for NO_X-tagging.

Regional land-based Tags	**Regional oceanic tags**	**Global sector/process-based tags**
Central Asia	Arctic	Aircraft
East Asia	Eastern North Atlantic	Biogenic
Europe	North Atlantic (remaining)	Biomass Burning
Mexico & Central America	North American East-Coastal zone	Lightning
Middle East	North American West-Coastal zone	Stratosphere
North Africa	North Pacific	
North America	Baltic and North Seas	
Russia-Belarus-Ukraine	Hudson Bay	
South Asia	Indian Ocean	
Southeast Asia	Mediterranean, Black, and Caspian Seas	
Rest of the World	Southern Hemisphere Oceans	

Table 2: Generalized Least Squares (GLS) linear trends in ppb/year along with their p-values (shown in parentheses) and 95% confidence intervals (shown in square brackets) for observed and modelled Peak Season Ozone and its tagged source contributions for various receptor regions.

Region	TOAR	Model	Local Ant. NO_X	Foreign Ant. NO_X	Natural NO_X	Ship NO_X	Local AVOC	Foreign AVOC	Methane	Natural VOC	Stratosphere
E Canada	-0.19 (0.01) [-0.32, -0.06]	-0.28 (0.01) [-0.50, -0.07]	-0.78 (<0.01) [-1.08, -0.48]	0.22 (<0.01) [0.16, 0.28]	0.06 (0.01) [0.02, 0.11]	0.08 (<0.01) [0.06, 0.10]	-0.33 (<0.01) [-0.41, -0.26]	0.10 (<0.01) [0.05, 0.14]	0.00 (0.98) [-0.06, 0.06]	-0.17 (0.10) [-0.39, 0.04]	0.14 (<0.01) [0.06, 0.22]
NW US	-0.09 (0.11) [-0.20, 0.02]	-0.11 (0.03) [-0.21, -0.01]	-0.39 (<0.01) [-0.46, -0.31]	0.12 (<0.01) [0.09, 0.16]	0.09 (<0.01) [0.04, 0.14]	0.03 (<0.01) [0.02, 0.05]	-0.15 (<0.01) [-0.16, -0.13]	0.03 (0.07) [0.00, 0.07]	-0.03 (0.03) [-0.05, 0.00]	0.00 (0.95) [-0.09, 0.10]	0.03 (0.31) [-0.03, 0.10]
SW US	-0.33 (<0.01) [-0.45, -0.21]	-0.26 (<0.01) [-0.38, -0.15]	-0.72 (<0.01) [-0.83, -0.62]	0.19 (<0.01) [0.15, 0.24]	0.10 (0.02) [0.02, 0.18]	0.05 (<0.01) [0.04, 0.06]	-0.24 (<0.01) [-0.27, -0.22]	0.08 (<0.01) [0.04, 0.12]	-0.10 (<0.01) [-0.15, -0.06]	-0.10 (0.11) [-0.23, 0.03]	0.11 (0.01) [0.03, 0.19]
NE US	-0.34 (<0.01) [-0.50, -0.18]	-0.50 (<0.01) [-0.69, -0.31]	-0.97 (<0.01) [-1.19, -0.76]	0.17 (<0.01) [0.14, 0.20]	0.12 (<0.01) [0.08, 0.16]	0.06 (<0.01) [0.05, 0.07]	-0.36 (<0.01) [-0.41, -0.31]	0.08 (<0.01) [0.05, 0.12]	-0.09 (<0.01) [-0.15, -0.03]	-0.24 (0.01) [-0.42, -0.06]	0.12 (<0.01) [0.07, 0.18]
SE US	-0.46 (<0.01) [-0.63, -0.28]	-0.63 (<0.01) [-0.79, -0.47]	-1.09 (<0.01) [-1.25, -0.94]	0.17 (<0.01) [0.13, 0.22]	0.09 (<0.01) [0.04, 0.15]	0.08 (<0.01) [0.06, 0.09]	-0.33 (<0.01) [-0.37, -0.29]	0.08 (<0.01) [0.03, 0.13]	-0.15 (<0.01) [-0.20, -0.11]	-0.32 (<0.01) [-0.49, -0.15]	0.12 (<0.01) [0.06, 0.18]
W Europe	-0.10 (0.26) [-0.29, 0.08]	-0.05 (0.46) [-0.18, 0.08]	-0.28 (<0.01) [-0.38, -0.18]	0.04 (0.03) [0.00, 0.07]	0.05 (<0.01) [0.03, 0.07]	0.12 (<0.01) [0.10, 0.14]	-0.17 (<0.01) [-0.21, -0.12]	-0.02 (0.14) [-0.05, 0.01]	0.08 (<0.01) [0.05, 0.11]	0.03 (0.34) [-0.04, 0.11]	0.02 (0.48) [-0.04, 0.08]
S Europe	-0.09 (0.45) [-0.33, 0.15]	-0.20 (0.01) [-0.35, -0.06]	-0.54 (<0.01) [-0.67, -0.41]	0.07 (0.01) [0.02, 0.13]	0.05 (0.03) [0.00, 0.09]	0.16 (<0.01) [0.14, 0.19]	-0.21 (<0.01) [-0.25, -0.16]	-0.01 (0.71) [-0.05, 0.04]	0.00 (0.94) [-0.06, 0.06]	-0.03 (0.56) [-0.15, 0.08]	0.05 (0.20) [-0.03, 0.12]
C&E Europe	-0.40 (<0.01), [-0.58, -0.22]	-0.05 (0.32), [-0.15, 0.05]	-0.28 (<0.01), [-0.36, -0.20]	0.08 (<0.01), [0.04, 0.13]	0.08 (<0.01), [0.05, 0.11]	0.07 (<0.01), [0.05, 0.09]	-0.18 (<0.01) [-0.21, -0.15]	-0.04 (0.01) [-0.07, -0.01]	0.09 (<0.01) [0.04, 0.13]	0.09 (0.04) [0.01, 0.17]	-0.01 (0.84) [-0.07, 0.05]
SE Europe	0.84 (0.01) [0.29, 1.38]	-0.06 (0.60) [-0.32, 0.19]	-0.56 (<0.01) [-0.80, -0.32]	0.28 (<0.01) [0.20, 0.36]	0.18 (<0.01) [0.09, 0.27]	0.03 (0.19) [-0.02, 0.08]	-0.28 (<0.01) [-0.32, -0.23]	-0.05 (0.20) [-0.12, 0.03]	0.18 (0.04) [0.01, 0.35]	0.08 (0.45) [-0.13, 0.28]	-0.01 (0.89) [-0.14, 0.12]

Table 3: Changes in the foreign anthropogenic NOx contributions and stratospheric contributions to springtime (March-May) mean MDA8 O3 in different receptor regions between the initial period (2000-2004) and recent period (2014-2018).

Region	Foreign anthropogenic NOx contribution		Stratospheric contribution	
	Initial Period	Recent Period	Initial Period	Recent Period
Eastern Canada	8.91	11.72	8.20	12.97
NW US	13.16	14.81	12.02	12.55
SW US	14.01	17.37	13.24	14.25
NE US	8.30	10.83	7.58	1.00
SE US	8.47	10.59	6.70	9.27
Western Europe	12.10	13.34	8.15	9.14
Southern Europe	13.25	14.66	8.77	9.48
C&E Europe	13.07	13.94	7.87	8.38
SE Europe	13.98	15.64	8.44	9.06